

**Interplay between Charge, Spin and Orbital
Ordering in $\text{La}_{1-x}\text{Sr}_x\text{MnO}_3$ Manganites**

Von der Fakultät für Mathematik, Informatik und
Naturwissenschaften
der Rheinisch- Westfälischen Technischen Hochschule Aachen
zur Erlangung des akademischen Grades eines Doktors
der Naturwissenschaften genehmigte Dissertation

vorgelegt von

Diplom-Physiker
Konstantin Istomin
aus Novosibirsk, Russische Föderation

Berichter: Universitätsprofessor Dr. Thomas Brückel,
Universitätsprofessor Dr. Bernd Büchner.
Tag der mündlichen Prüfung: 14.03.2003

Diese Dissertation ist auf den Internetseiten der
Hochschulbibliothek online verfügbar.

Contents

1	Introduction	3
1.1	Introduction	3
1.2	Structure	4
1.3	The Influence of Cubic Field	4
1.4	Jahn-Teller Effect	5
1.5	Influence of Super and Double Exchange	7
1.5.1	Super Exchange	7
1.5.2	Double exchange	8
1.5.3	Calculation of the total Hamiltonian	8
1.6	Properties	10
1.7	Charge and Orbital Ordering in Manganites	13
2	Review of Experimental Works	17
2.1	Introduction	17
2.2	Neutron diffraction	18
2.3	High Energy X-ray Scattering	21
2.4	Theory of Resonant X-Ray Scattering	23
2.5	Review of RXS Experiments	26
2.6	Conclusions from the Experimental Review	29
3	Preparation and Characterization	31
3.1	Ceramics	31
3.2	Characterization	33
3.2.1	X-Ray Powder Diffraction	33
3.2.2	Atom Emission Spectroscopy with Inductively Coupled Argon Plasma	34
3.3	Crystal Growing	34
3.3.1	Introduction	34
3.3.2	Experimental Procedures	35
3.3.3	Results	37

3.4	Characterization	39
3.4.1	Microprobe Analysis	39
3.4.2	Magnetization	40
3.4.3	Resistivity	41
4	Experiments with X-Ray Scattering	45
4.1	Resonant X-Ray Scattering	45
4.2	High-Energy X-Ray Scattering	49
4.3	Non-resonant X-Ray Scattering	54
4.4	Interpretation Of The Experimental Results and Discussion	63
4.4.1	Resonant X-Ray Scattering	63
4.4.2	Charge Ordering	65
4.4.3	Interplay Between Orbital Ordering and Lattice Distortions	65
4.4.4	Interplay between Charge and Orbital Ordering	66
5	Experiments with Neutron Scattering	69
5.1	Introduction	69
5.1.1	Elastic Nuclear and Magnetic Scattering	70
5.1.2	Inelastic Neutron Scattering	70
5.1.3	Magnetic Critical Neutron Scattering	71
5.1.4	Paramagnetic Scattering	71
5.2	Rules For Separation	71
5.3	Diffuse Neutron Scattering Experiments	72
5.4	Polarized Neutrons Experiments	78
5.5	Results	79
6	Summary of Results	83
A	RXS Mesh-Scans	85
B	Neutron Scattering Data	89
B.1	List of Abbreviations	103
B.2	Acknowledgement	104
B.3	Curriculum Vitae	105

Chapter 1

Introduction

1.1 Introduction

Strongly correlated electron systems, in which the Coulomb interactions between electrons strongly inhibit their motion, are of great interest due to their possible applications in technology. These materials are characterized by a wide variety of ground states, ranging from antiferromagnetic to ferromagnetic and from insulating to superconducting. In many cases transitions between these ground states can be driven by relatively small changes in the chemical doping or temperature. The origin of such unusual sensitivity is believed to be in the fact that not a single degree of freedom dominates the behavior, but rather a number of correlated degrees of freedom. These can include the spin, charge, orbital and lattice degrees of freedom. The ground state is then determined by the interplay between the competing degrees of freedom. However, despite this qualitative understanding, the complete description of the electronic behavior still does not exist. Investigation of this problem remains one of the central tasks in condensed matter research today.

In this work interplay between charge, orbital and spin ordering in lightly doped $La_{1-x}A_xMnO_3$ with $x \approx 1/8$ has been studied using both resonant and non-resonant X-ray scattering as well as neutron scattering.

The outline of this work is as follows:

- Chapter 1 is an introduction with a basic theory of manganites and their most important properties.

- Chapter 2 contains overview of experimental works devoted to studying of charge, spin and orbital ordering in this system.
- In Chapter 3 sample preparation and characterization procedures are described.
- Experiments with X-ray scattering are presented and discussed in Chapter 4.
- Chapter 5 is devoted to experiments with neutron scattering.
- The results are summarized in Chapter 6
- Appendix contains some additional information such as resonant X-ray scattering mesh-scans, neutron scattering patterns and credits.

1.2 Structure

The mixed-valence compounds of the type $La_{1-x}A_xMnO_3$, where A is a bivalent atom (for example Sr, Ca, Ba, etc.,) are the most investigated among manganites. They have a typical Pbnm orthorhombic perovskite structure with space group Pbnm with a $a\sqrt{2} \times b\sqrt{2} \times 2c$ supercell. In the ideal perovskite structure the centre of the cell is randomly occupied by a large lanthanide cation or an alkali cation. At the corners there are smaller Mn ions, the oxygen ions are situated at the centres of the cubic edges. (See. Figure 1.1).

These compounds can be regarded as solid state solutions, for example of $LaMnO_3$ and $SrMnO_3$ with $La^{3+}Mn^{3+}O_3^{2-}$ and $Sr^{2+}Mn^{4+}O_3^{2-}$ ion valence states, respectively. The intermediate compositions have a valence structure $(La_{1-x}^{3+}Sr_x^{2+})(Mn_{1-x}^{3+}Mn_x^{4+}O_3^{2-})$ containing trivalent ($3d^4$) and tetravalent ($3d^3$) manganese ions. Thus, doping the parent compound $LaMnO_3$ with a bivalent element at concentration x produces an equal amount of holes in the 3d band of the material (for $x < 0.5$). For $x > 0.5$, the compound can be regarded as the parent compound $SrMnO_3$ doped with electrons of concentration $1 - x$.

1.3 The Influence of Cubic Field

The ground states of the Mn-ions consist of five-fold degenerate 3d-orbits. If one such ion is situated in octahedral oxygen neighborhood, it splits due to the influence of the

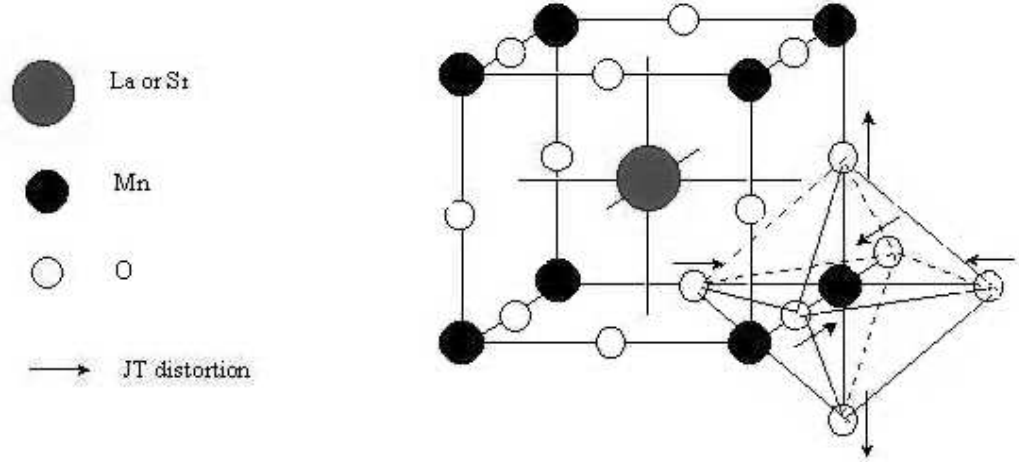


Figure 1.1: The idealized perovskite unit-cell of manganese and Jahn-Teller distortions.

cubic crystal field (CF) into two energy states, t_{2g} and e_g , with two and three orbitals respectively. These two states have an energy gap of $\Delta_{CF} = 10Dq \approx 1eV$ where the energy of the e_g states are $6Dq$ higher than the ground state energy and the energy of t_{2g} are $4Dq$ lower than the ground state energy (See Fig. 1.2). D is the crystal parameter and $q \sim \langle r^4 \rangle$ where r is the average atom distance.

In Mn^{4+} there are three electrons at the 3d-shell, therefore all three $4t_{2g}$ are filled with one electron each. The total is spin is $S = 1.5$. On the other hand, Mn^{3+} ions obtain one additional electron at the e_g shell which spin is parallel to the spins of t_{2g} -electrons due to the strong Hund's coupling.

1.4 Jahn-Teller Effect

Besides the splitting of the 3d-orbitals under the influence of the cubic crystal field, another splitting of the e_g -shell is possible which is realized through distortions of the lattice. Slightly distorted orthorhombic structure leads to further separation of the both e_g -states. This distortion exists due to the different ion sizes, or in the case of Mn^{3+} ions, due to the Jahn-Teller (JT) effect. For the Mn^{3+} ions, according to the JT theorem [1]

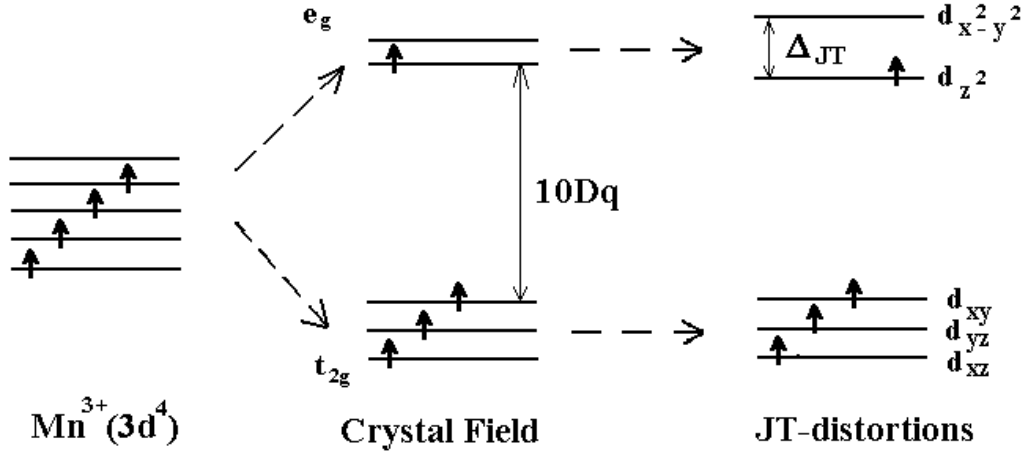


Figure 1.2: Splitting of the $3d$ -orbitals under the influence of Crystal Field and Jahn-Teller distortions.

¹, splitting of degenerated e_g -states through the lattice distortion lead to an energy gain and is an order of magnitude lower ($\Delta_{JT} \approx 0.1$ eV) than the energy difference between e_g and t_{2g} levels.

When the lattice has predominantly Mn^{3+} ions then one can observe a cooperative static JT-effect with a permanent distortion of the lattice structure.

In the case of Mn^{4+} there are no static JT-distortions because the e_g -shells are not occupied. When a Mn^{4+} ions is replaced locally by a Mn^{3+} then there is one additional electron at the e_g -orbit of one lattice site. At this site a local JT-distortion takes place because the neighboring sites stay undistorted. However the e_g electron has a possibility to hop from one site to another neighboring one (in other words Mn^{3+} and Mn^{4+} are changing their places). It takes the distortion with itself. Such combination of electron and distortion is called polaron. The JT-effect is statistically dispersed over the whole lattice and changing in time. This effect is called dynamic JT-effect.

Another case of dynamic JT-effect takes place if the temperature of a system with static JT-effect becomes higher than the JT-temperature ($T > T_{JT}$). The JT-active ions can in fact stay at their lattice sites, however the lattice distortion is dynamic due to the

¹”any non-linear molecular system in a degenerate electronic state will be unstable and will undergo distortion to form a system of lower symmetry and lower energy thereby removing the degeneracy”

higher energy. The e_g -electron hops between two possible orbitals way and back and it leads to oscillation of the O_6 -octahedra between both possible distorted states.

1.5 Influence of Super and Double Exchange

In the highly correlated transition materials, among them also in the system studied in present work, there are two basic competing mechanisms which affect the magnetic properties: super exchange (SE) and double exchange (DE) between the Mn-ions. SE is in favour of antiferromagnetic order and DE is in ferromagnetic order.

1.5.1 Super Exchange

SE is a indirect Spin-Spin exchange process in systems where the distance between magnetic ions is too large for a direct exchange. Dipole-Dipole exchange processes are weaker than the SE exchange process, therefore the latter is the primary mechanism for the magnetism. The spin coupling in this case takes place between two Mn-ions over an ion lying in between (in case of $La_{1-x}Sr_xMnO_3$ over O^{2-}) without charge transfer (See Fig. 1.3).

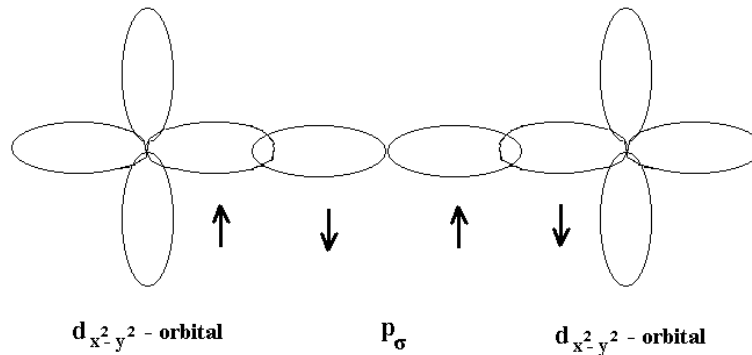


Figure 1.3: Super exchange of two 4d-ions over an O^{2-} -ion.

The orbitals would not overlap by a pure ionic connection. In reality there is a weak covalent binding between the Mn- and the O-atoms. Since this binding is small, the disturbance of the electron movement is weak, and the electrons stay localized. This results in a possible spin structure which features in an antiferromagnetic order of 3d-spins.

This coupling, however, can be of ferromagnetic nature. For realization of this kind of coupling the Goodenough-Kanamori rules [3] must be implemented:

- An antiferromagnetic exchange occurs when two occupied orbitals at neighboring places overlap.
- The exchange is ferromagnetic when one empty and one occupied orbital overlap. This exchange is much weaker than in the antiferromagnetic case.

1.5.2 Double exchange

Chemical doping brings transferable charge carriers into the system which leads to ferromagnetic coupling of the Mn-spins. This exchange mechanism was first introduced by Zener [2] and later called DE. The explanation is following:

- The Hund's coupling within one atom is strong, therefore only possible configuration of the system is when the spins of the charge carriers are parallel to the local ion spin.
- The charge carriers do not change their spins when moving from one neighboring site to another. In cooperation with the Hund's rule it forbids a hopping process when neighboring atoms obtain anti-parallel spins.

According to this, the DE mechanism leads to a ferromagnetic order and is principally different from the usual (direct or indirect) exchange mechanisms. Figure 1.4 shows the principle of the DE which occurs between two unequal (Mn^{3+}/Mn^{4+}) ions.

1.5.3 Calculation of the total Hamiltonian

Let us consider now a Bravais lattice of magnetic ions, which spin ordering has an antiferromagnetic coupling in the ferromagnetically layered system, where every ion spin S is ferromagnetically coupled to z' neighboring spins of the same layer but antiferromagnetically coupled to z spins of the adjacent layers. The exchange integrals will be denoted as $J' > 0$ and $J < 0$. The Zener charge carriers are allowed to hop within one layer as well as between the neighboring layers (with transfer integrals b' and b). N is the number of

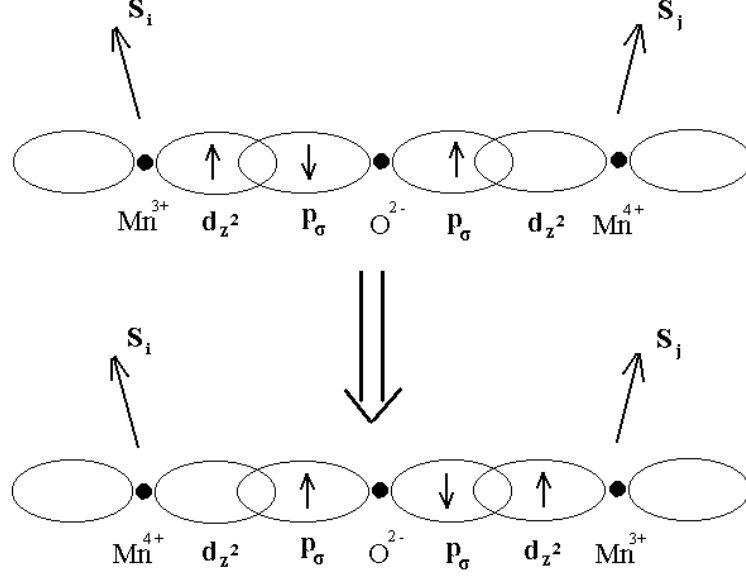


Figure 1.4: Double Exchange Mechanism.

the magnetic ions per unit cell, and Nx is number of charge carriers. In configurations, where spins are ordered parallel within one layer but every two neighboring layers are canted with an angle Θ , there is a canting angle Θ_0 which can be calculated from the minimization of the energy of super and double exchange.

For the SE energy:

$$E_{SE} = -Nz'J'S^2 + Nz|J|S^2 \cos \Theta_0. \quad (1.1)$$

For calculation of the DE-energy one should calculate first the energy $E_{DE,k}$ of a Zener charge carrier with wave vector \vec{k} . The amplitude of the corresponding wave function Ψ_i is $\alpha_i = e^{i\vec{k}\cdot\vec{R}_i}$. Together with $\Psi = \sum \alpha_i \varphi_i$ and $t_{ij} = b_{ij} \cos \frac{\Theta_{ij}}{2}$ we have: ²

$$E_{DE,k} = \sum_{i,j} t_{ij} e^{i\vec{k}\cdot(\vec{R}_j - \vec{R}_i)} = -b'\gamma'_k - b\gamma_k \cos \frac{\Theta_0}{2}. \quad (1.2)$$

Where $\gamma'_k = \sum_{j'} e^{i\vec{k}\cdot(\vec{R}_{j'} - \vec{R}_i)}$ and $\gamma_k = \sum_j e^{i\vec{k}\cdot(\vec{R}_j - \vec{R}_i)}$ are sums over the next neighbors

² φ_i is the complete set of orthogonal functions from which the wave function Ψ is linearly combined, t_{ij} is the transfer integral between ion i and j .

at place i . Accepting that b and b' are positive, the energy $E_{DE,k}$ is limited from below with

$$E_{\min} = -\gamma'_0 b' - \gamma_0 b \cos \frac{\Theta_0}{2} \quad (1.3)$$

The Nx Zener charge carriers have energy about E_{\min} , then the total DE-energy is

$$E_{DE} = Nx E_{\min} \quad (1.4)$$

From the minimization of the sums of 1.1 and 1.4 one can obtain:

$$\cos \frac{\Theta_0}{2} = \frac{bx}{4|J|S^2} \quad (1.5)$$

and

$$H_{\text{total}} = E_{SE} + E_{DE} = -N(z'J'S^2 + xz'b' + z|J|S^2 + \frac{zb^2x^2}{8|J|S^2}). \quad (1.6)$$

It is not possible to calculate the energy without knowing the value of the exchange integral. Many theoretical works are devoted to this problem (See [4], [5], [6]) but the exact values of the exchange integral have never been measured experimentally.

1.6 Properties

In the case of $La_{1-x}Sr_xMnO_3$, the doping level can be varied over the whole range from 0 to 1 which affects the properties of the manganites dramatically, causing a series of phase transitions and producing various types of ordering in the system, such as charge, orbital and magnetic ordering. (See Fig. 1.5)

Among the unique properties in the manganites, the colossal magnetoresistance (CMR) is particularly important.

This effect is seen within the x range of $x \approx 0.15$ to $x \approx 0.5$ where the metallic ferromagnetic phase exists and means that the resistivity ρ of the material decreases when a magnetic field is applied. The magnetic field aligns the core spins of the Mn ions and therefore electrons can easily hop from one Mn site to another due to the DE mechanism. The size of the effect, $\delta\rho/\rho$, may be as high as tens of percent in fields of order 1 T and has a maximum around the Curie temperature T_C (Fig. 1.6 [7]). As the

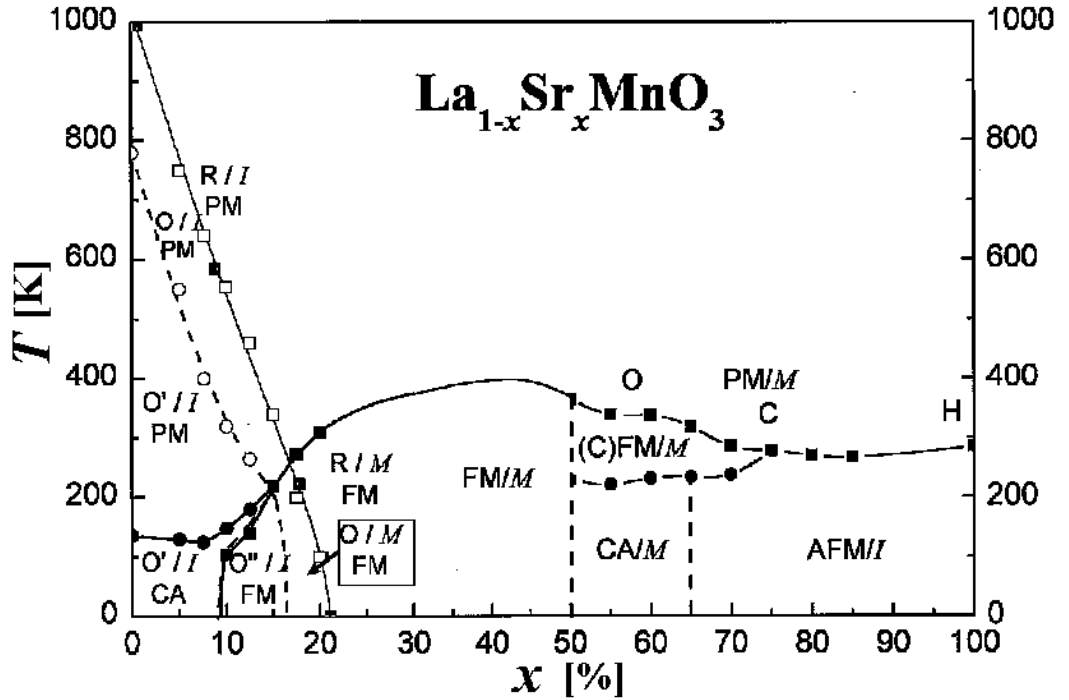


Figure 1.5: Complete phase diagram of $\text{La}_{1-x}\text{Sr}_x\text{MnO}_3$. From [8]. Abbreviations used in this figure: O, O', O'' - Different Orthorhombic phases, R - Rhombohedral, C - Cubic, H - Hexagonal, I - Insulator, M - Metal, PM - Paramagnetic, FM - Ferromagnetic, AFM - Antiferromagnetic, CA - Canted

temperature increases, the ferromagnetic phase is replaced by the paramagnetic phase with much less conductivity.

The temperature behavior of the electrical resistivity depends strongly on the doping level (Fig. 1.7). A characteristic feature of these curves is the point T_0 , for $0.1 < x < 0.3$, where CMR has a maximum (point T_0 lies in the neighborhood of T_C). As the temperature decreases from T_0 , $d\rho/dT < 0$ is observed, corresponding to the metallic phase; on the other hand above T_0 we have $d\rho/dT > 0$.

This phenomena has attracted a lot of attention of investigators in the early 1990s because of its potential for engineering and technological applications. On the other hand, the physical properties exhibited by the manganites are so rich and diverse that it is attracting intense experimental and theoretical interest.

A very fundamental question which remains to be answered is how adequately the DE

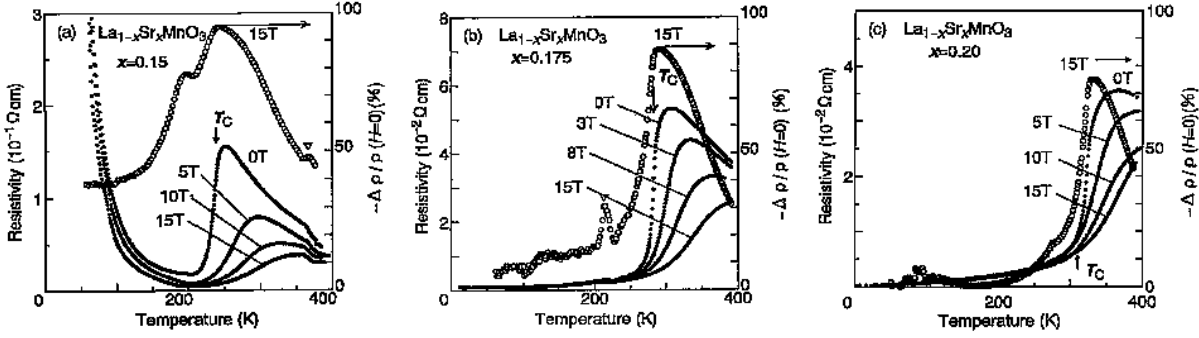


Figure 1.6: Temperature dependence of resistivity for $La_{1-x}Sr_xMnO_3$ under various magnetic fields. (a) $x=0.15$, (b) $x=0.175$, (c) $x=0.2$. Open circles represent the magnitude of negative Magnetoresistance $-\left[\rho[H] - \rho[0]\right]/\rho[0]$ with a magnetic field of 15 T. Open triangles represent structural transitions. From [7].

model describes the physics of the manganites. Several dynamical mean field calculations [9], [10] show good qualitative agreement with the experimental data. This is true, in particular, for the general structure of the temperature - electron concentration phase diagram containing a homogeneous ferromagnetic phase and various metallic or insulating antiferromagnetic phases. Also magnetization and various transport properties are well described by the DE model, including the temperature, electron concentration and field variation of electrical resistivity and optical conductivity.

However, recently Millis et al. [11] argued against the DE model as the basic theory for the manganites. He had shown in particular, that the predictions for T_C are too high and for the resistivity are an order of magnitude too low.

To explain the real physical properties of the manganites, corrections for the interaction of electrons with lattice degrees of freedom must be introduced into the theory. This gives a much better agreement with experiment for the Curie temperature and $\rho(T)$ dependence.

Moreover, one should take into account the possibility that the cubic lattice may be distorted locally due to the JT effect on manganese ions. The inclusion of JT distortions, easy to observe experimentally, makes it possible to understand the nature of the paramagnetic insulating phase in the electron concentration range where ferromagnetic ordering exists.

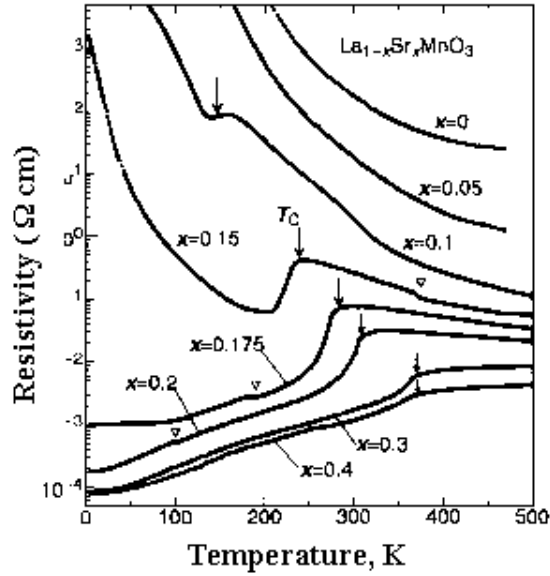


Figure 1.7: Temperature dependence of the resistivity in zero field for $La_{1-x}Sr_xMnO_3$. Arrows indicate the critical temperature for the ferromagnetic transition. Open triangles represent structural transitions. From [7]

1.7 Charge and Orbital Ordering in Manganites

The idea of charge ordering (CO) in manganites dates back to Goodenough [12]. The phenomenon of CO is interesting because there is a necessity for taking into account all aspects of manganites' physics (localization of charges, structural distortions, orbital ordering, and magnetic interactions). It was prompted by the discovery in neutron diffraction data [13] of superstructural peaks which have no relation to magnetism.

The first reliable experimental observation of this phenomena was done in 1997 [14] on $La_{0.5}Ca_{0.5}MnO_3$. This compound (see Fig. 1.8) is located on the phase boundary between ferromagnetic metal and antiferromagnetic insulator and its resistivity exhibits semiconductor temperature behavior. Observed spin ordering was the C-type of AFM structure. Replacing of a Ca^{2+} ion by a La^{3+} leads to creation of a JT Mn^{3+} ion which deforms the ideal octahedron by splitting of filled e_g -shells. In the range of low doping level $1 - x \ll 1$ the JT ions are randomly distributed and the local JT distortion is low. Decreasing of x leads to interaction of the Mn^{3+} ions in such way that the lattice tensions

are relaxed and the global JT distortion is optimized. Above $x = 0.5$ the compound is insulating because it contains no transferable charge carriers, it means that the distortions are localized and not averaged.

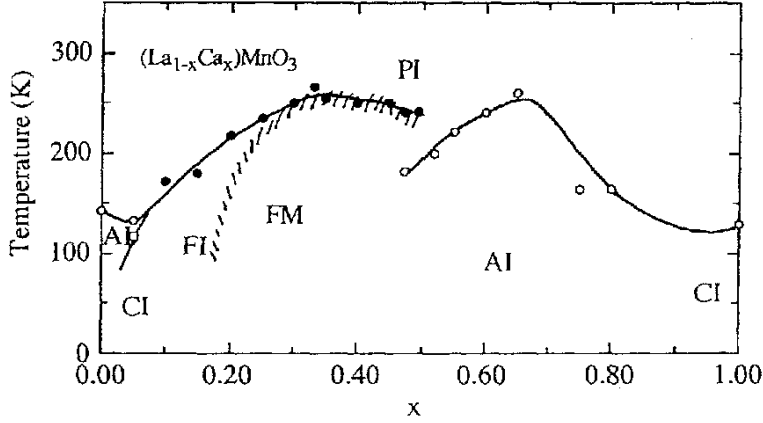


Figure 1.8: Magnetic phases in $La_{1-x}Ca_xMnO_3$ [15]. The shaded lines represent the insulator-metal transitions. The regions are indicated with the same abbreviations like in Fig.1.5, only A stands here for antiferromagnetic.

Interactions between Mn^{3+} ions have two components: Coulomb interactions and JT-distortions. The first one is isotropic and responsible for CO. The second one is anisotropic, fields from different JT Mn^{3+} ions overlap and determine type of z^2 -orbital ordering.

Fig. 1.9 shows the CO observed model for half-doping level leading to the lattice period doubling of the crystal. The CO has a simple AFM type. Spins $S = 2$ (Mn^{3+}) and $S = 3/2$ (Mn^{3+}) also have the AFM structure despite the fact that the magnetic correlation lengths of each sub-lattice are different [14]. Along the c -axis FM spin chains are observed. Physically, orbital ordering (OO) is more interesting. OO is arrangement of long axis of octahedra with Mn^{3+} ions (or arrangement of doped holes surrounded by local JT distortions) in the ab -plane. Sometimes OO is also called polaron ordering [16].

Later, stripe structures of CO were observed by electron microscopy for compounds with $x > 0.5$: $La_{0.33}Ca_{0.67}MnO_3$ ($x = 2/3$) and $La_{0.25}Ca_{0.75}MnO_3$ ($x = 3/4$) [17]. The stripes are observed in the insulating phase when distribution of ions of different valence becomes anisotropic. Like in the case of $La_{0.5}Ca_{0.5}MnO_3$, corresponding CO along the

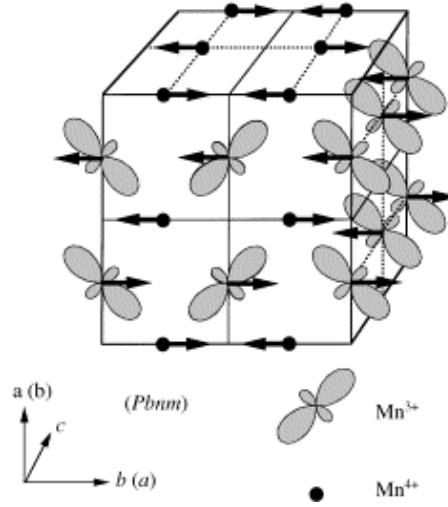


Figure 1.9: Spin, Charge and Orbital Ordering model of the CE type observed for most of $x \approx 1/2$ manganites. The e_g -orbitals ordering on Mn^{3+} sites are also shown. The Mn^{4+} sites are indicated by closed circles. From [18].

(110) axis in the compounds of $La_{1-x}Ca_xMnO_3$ with commensurate carrier concentrations ($x = 1/2, 2/3, 3/4$ and $4/5$) has a chain type. OO also remains of the same type but chains with different orientation are not continuous any longer. The experiments [17] show that in the samples with incommensurate x (for example $5/8$) there is a separation to domains with commensurate x (in the case of $5/8$ to $x = 2/3$ (75 % of the volume) and $x=1/2$ (25 %) because $0.75 \cdot 2/3 + 0.25 \cdot 1/2 = 5/8$).

Many works are devoted to the explanation of the orbital and magnetic structures of manganites. The establishing mechanism of an orbital structure in JT manganites was often discussed. There are three basic mechanisms which can lead orbital structures [19]: (a) the quadrupole interaction; (b) the orbital depending exchange interaction; (c) the cooperative JT effect, i.e. JT phonons freeze due to interaction with orbitally degenerated ground state. No experimental work devoted to the case (a) has been found. The case (b) is represented by the Kugel-Khomskii model [19] and related ones [20], [21]. The (c) approach is represented mainly by the Kanamori model [22], which was developed and applied to the manganites in works [23], [24], [25], [26], [27].

The authors of several papers have failed to reach the common opinion about the reasons of interactions forming the magnetic structure in undoped manganites.

In the present work the interplay between spin, orbital, magnetic and lattice degrees of freedom in lightly doped $La_{1-x}Sr_xMnO_3$ compounds has been studied using complimentary resonant and non-resonant X-ray scattering, diffuse neutron scattering and macroscopic analysis.

Chapter 2

Review of Experimental Works

The charge and spin ordering can be investigated by the traditional neutron and electron diffraction techniques. ¹

2.1 Introduction

Lightly doped $La_{1-x}Sr_xMnO_3$ with $x \approx 1/8$, which is located between the antiferromagnetic insulating region and the ferromagnetic metallic region (Figure 2.1 [28]), shows many anomalous behaviors ([7], [16], [29], [30]. $La_{0.875}Sr_{0.125}MnO_3$ is a paramagnetic insulator above $T_C \approx 180$ K and has a ferromagnetic state below it. Recently, it has been found that $La_{0.875}Sr_{0.125}MnO_3$ becomes a ferromagnetic insulator below 140 K. ([31]). One important question is why the hole-doped system can exist as an insulator. The superstructure, first observed by Yamada et al ([16] and attributed to the CO phenomena, indicates that CO may be responsible for the insulating behavior.

Another interesting question is what is the origin of the ferromagnetism. Since the system is insulating, the simple DE mechanism cannot be applied. A model Hartree-Fock calculation for $LaMnO_3$ has predicted that, if the JT distortions are suppressed, a ferromagnetic insulating state with orbital ordering would be realized [32]. It means that the superexchange interaction between the Mn^{3+} ions can be ferromagnetic because of orbital ordering ([19]. Endoh et al. [30] have claimed to have observed orbital ordering

¹Neutrons are a bulk probe, electrons see only surface near phenomena. Neutrons do not strongly interact with charges, however they can measure local lattice distortions due to charge ordering.

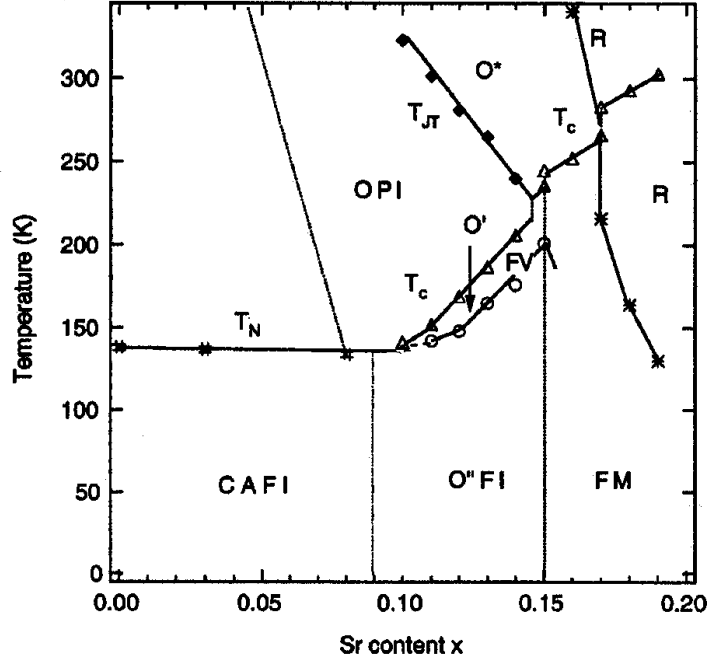


Figure 2.1: Phase diagram for $La_{1-x}Sr_xMnO_3$, $0 \leq x \leq 0.20$. [28] The regions are indicated with the same abbreviations like Fig.1.5

below 145 K using X-ray resonant scattering and argued that the orbital ordering is essential for the ferromagnetic and insulating state. However, the orbital ordered state without charge ordering is expected to be metallic and may not be consistent with the fact that $La_{0.875}Sr_{0.125}MnO_3$ is insulating.

In order to understand the electronic structure of the ferromagnetic and insulating state in the lightly doped manganites, it is necessary to consider the complicated interplay between charge, spin and orbital orderings, as well as lattice distortions.

2.2 Neutron diffraction

In $La_{1-x}Sr_xMnO_3$ system charge and orbital ordering was first investigated by Yamada et al in 1996 [16] by single crystal neutron diffractions for stoichiometries corresponding to $x=0.1$ and $x=0.15$.

Fine mesh scans at $T = 10$ K over a wide region in the $(h, k, 0)_C$ reciprocal space

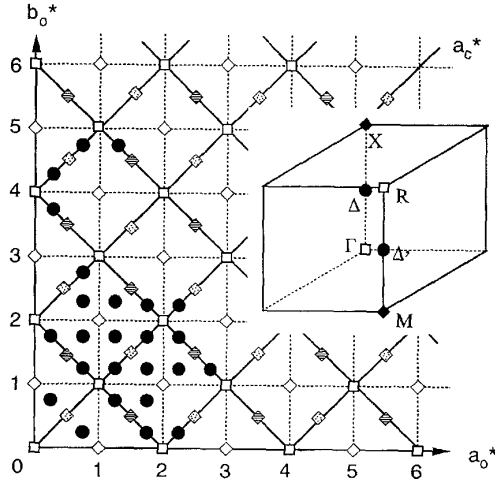


Figure 2.2: Schematic representation of the observed diffraction pattern. The solid lines represent the pseudocubic $(h, k, 0)_c$ reciprocal space. The dashed line give the orthorhombic $(h, k, 0)_o$ lattice. The small solid circles give the the positions of the superstructure satellites. The inset shows the corresponding positions of the Bragg reflections in the first Brillouin zone of pseudocubic reciprocal space. Notice Δ and Δ' points are equivalent when referred to the exact orthorhombic symmetry. The equivalent superlattice reflections originating from the different domains are distinguished by the following symbols: open diamond M points of domain I; stripped diamond X points of domain II; dotted diamond X points of domain III. [16]

were carried out. For both samples with $x=0.1$ and $x=0.15$ a series of satellite reflections indexed as $(h \pm 1/4, k \pm 1/4, 0)_O$ were found (See Fig. 2.2). However, since the samples are multidomain crystals composed of microtwins, there is another possible indexing referring to the true orthorhombic lattice: $(h, k, l \pm 1/2)_O$.

Temperature dependencies of the satellite intensities as well as the main Bragg reflection (Γ points) and the superlattice reflections (X or M points) were investigated. The results are summarized in Fig. 2.3.

Important characteristics of the experimental results:

Figure 2.3 (a), ($x=0.15$). The satellite reflection $(2,2,-0.5)$ sets in at $T_p=190$ K. Temperature variation of the satellite reflection at $T < T_p$ is rather gradual indicating that the transition at T_p is of second order type.

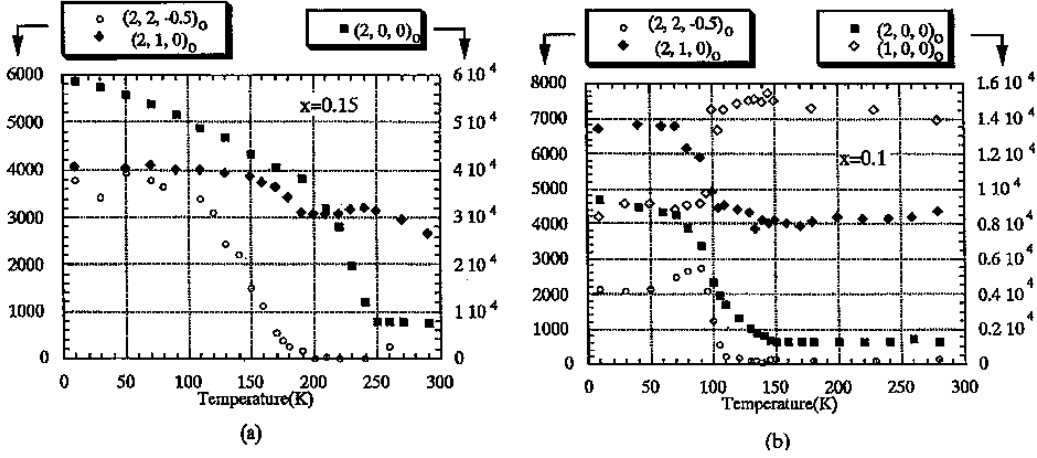


Figure 2.3: Temperature dependencies of the intensities of various types of reflection: (a) $x = 0.15$, (b) $x = 0.10$. [16]

Figure 2.3 (b), ($x=0.10$). The satellite reflection $(2,2,-0.5)$ sets in at $T_p \approx 100$ K. Temperature variation of the satellite reflection shows clear cutoff indicating that the transition at T_p is of first order type.

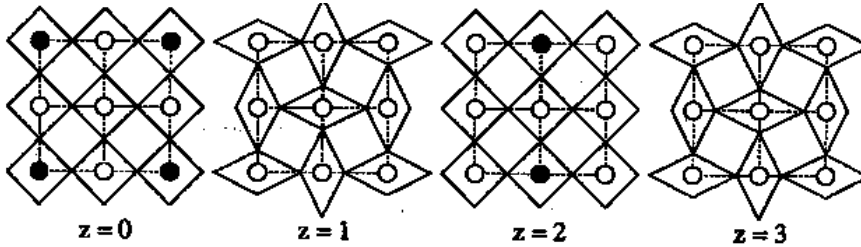


Figure 2.4: According to the Yamada CO model there are periodical two layers with charge carriers (full circles, Mn^{4+}) and two JT-distorted layers without charge carriers. This ordering exists for optimal $x=0.125$ doping level.

Authors clearly says that the transition at T_p is due to polaron ordering and explains the quartering of the unit cell with the model shown in figures 2.4 and 2.5. Layers, in which the ordering of holes in a - and b -directions exhibits in doubling of the pseudocubic unit cell, changes with layers without free charge carriers which show cooperative JT-distortions. The quartering of the unit cell exists because of the hole ordering in the ($z=2$)-layer in

relation to the ($z=0$)-layer. The hole positions in these layers are different due to the orthorhombic lattice distortions, therefore only reflections with indexing $(0, 0, n_l \pm 1/4)$ are allowed (n_l even). This model is based on the assumption of exact $x=0.125$ doping level.

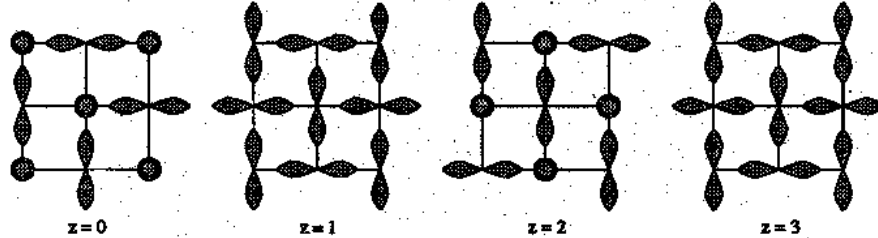


Figure 2.5: One possible ordering of $d_{(x,y,z)^2}$ -orbitals according to the Yamada model for exact $x=0.125$ doping. Holes are not shown since they are not ordered as opposed to the orbitals. The circle symbols are d -orbitals perpendicular to the figure plane.

It is still unclear why sample with $x=0.15$ exhibits a second order type transition to the orbital ordered phase and sample with $x=0.10$ has a first order transition.

In 2000 Yamada et al re-investigated the $La_{1-x}Sr_xMnO_3$ ($x = 0.10$) system and calculated another model which is the most stable (See Fig. 2.6.) [33].

2.3 High Energy X-ray Scattering

Superstructure reflections attributed to CO have been observed in $La_{1-x}Sr_xMnO_3$ ($x=0.06, 0.125$ and 0.15) single crystals using high energy (100-120 keV) X-ray diffraction by Niemöller et al in 1999 [34].

At low temperatures 16 superstructure reflections were detected at positions $(h \pm 0.25, k, 0)$ and $(h, k \pm 0.25, 0)$ (See Fig. 2.7 a), h and k being integer or half-integer (filled circles, authors call them charge peaks). Temperature dependences of charge peak intensities are shown in Fig. 2.7 b.

Sample with $x=0.125$ exhibit a first order type transition to CO state at $T=150$ K. Sample with $x=0.15$ has a second order transition with an unclear transition temperature of about 180 K. Authors suggest that the $x=0.15$ crystal should be regarded as a charge ordered $x=0.125$ compound doped by a small amount of additional holes.

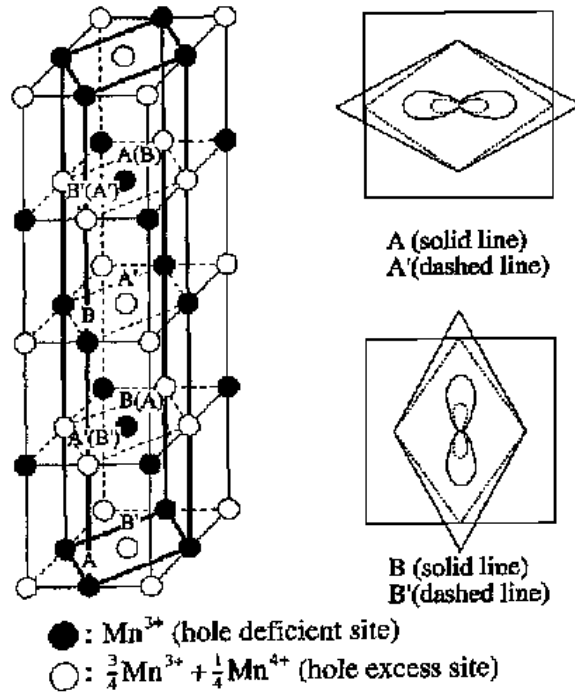


Figure 2.6: (a) Proposed hole configuration corresponding to the most stable state. The unit cell of the hole lattice is $(\sqrt{2} \times \sqrt{2} \times 2)_{\text{cubic}}$. (b) Schematic representation of the elongated orbitals and the deformation of the oxygen octahedron at various types of small polarons. A, B (solid lines): orbital and deformation around the Mn^{3+} site, A', B' (dashed lines): orbital and deformation around the $Mn^{3.25+}$ site. [33]

In addition to the charge peaks, superstructure reflections were found in all studied samples at $(h \pm 0.5, k \pm 0.5, l \pm 0.5)$ positions, h, k, l being integer or half-integer. These reflections are observed in the entire temperature range. Authors suggest that these reflections originate from imperfect destructive interference of adjacent layers in the perovskite structure due to the Sr-doping which introduces distortions in the tilt pattern of the oxygen octahedra.

Generally, Niemöller et al support the Yamada model and add that a cooperative JT effect must lead to structural distortions which do not support CO.

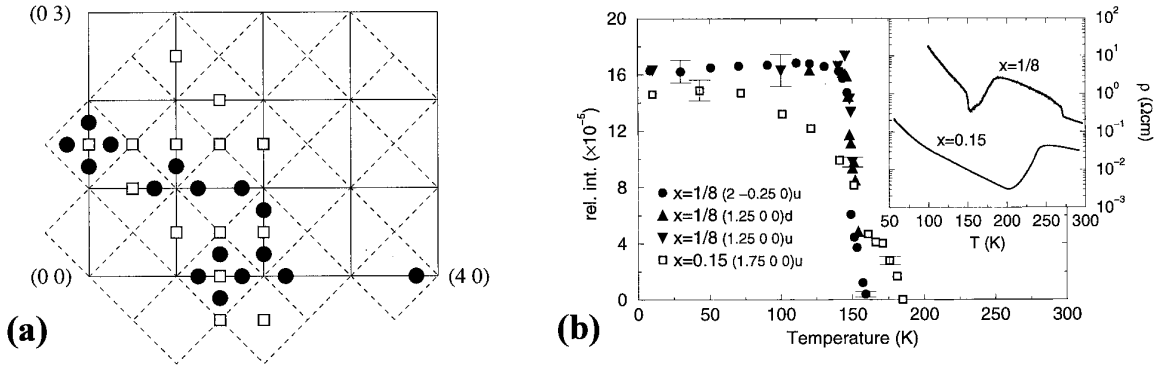


Figure 2.7: (a) The surveyed area in the reciprocal space. The solid lines belong to the cubic reciprocal lattice, whereas the dashed lines show the h, k plane of an orthorhombic setting. The corners represent the fundamental reflections. Charge peaks and superstructure reflections due to Sr-doping have been observed at the indicated positions. (b) Comparison of the charge peak intensities in the $x=0.125$ and the $x=0.15$ sample. The intensities are normalized relative to the adjacent Bragg-reflections. The inset shows resistivity measurement from the same samples on a logarithmic scale. [34]

2.4 Theory of Resonant X-Ray Scattering

The direct experimental observation of the orbital ordering, predicted by various theoretical considerations, has proved quite difficult. A theory for the resonant scattering (RXS) mechanism has been developed by Murakami et al [35] in 1998.

The incoming photon is virtually absorbed to promote a core electron to an empty intermediate excited state, which subsequently decays to the same core hole emitting a second photon with the same energy than the incoming one (Figure 2.8). Since the excited electron is sensitive to any anisotropy of the environment (it can either be of structural origin or due to the anisotropic charge distribution in the ground state of the system) it gives rise to a tensor component in the atomic scattering factor with sharp photon energy dependence in the anomalous dispersion region. This anisotropy of the x-ray susceptibility tensor leads to a number of well known phenomena, like for example, existence of "structurally forbidden" reflections and orientational dependence of x-ray absorption near edge structure.

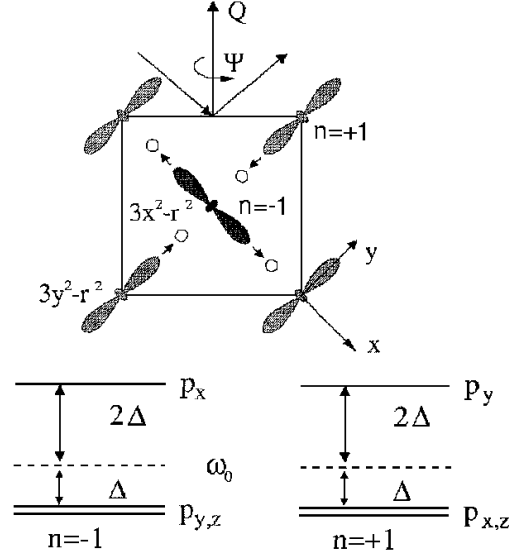


Figure 2.8: Upper panel: Schematic view of the orbital and spin ordering in the $a-b$ plane of the perovskite manganite, $LaMnO_3$. Lower panel: Schematic energy level diagram of Mn $4p_{x,y,z}$ in the orbitally ordered state. From [35]

The excitation of the Mn $1s$ electron to empty $4p$ states (which are initially unoccupied but split in their y and x, z components by an energy Δ due to some interaction with the surrounding) gives rise to a nonzero resonant scattered intensity proportional to Δ^2 at the Bragg reflections sensitive to the difference between the two orbitally ordered sublattices. In cubic systems such as $LaMnO_3$ these reflections are $(h00)$ and $(0k0)$, with h, k odd, that are nominally extinct (as a consequence of the Bragg equation when all Mn^{3+} ions are equivalent).

For the difference reflection, the resonant scattered intensity may be written [35]

$$I^{\text{res}} = \left| \sum_{m=x,y,z;n=\pm 1} n \frac{\langle s | P^\alpha | p_m \rangle \langle p_m | P^\beta | s \rangle}{\omega - \omega_0 - \delta\omega_m^n + i\Gamma/2} \epsilon'^\alpha \epsilon^\beta \right|^2, \quad (2.1)$$

where the coordinate system has been chosen so that x and y are along the direction of extension of the ordered e_g orbitals and z is perpendicular to the $x-y$ plane. $|s\rangle$ and $|p\rangle$ are the wave functions of the Mn $1s$ and $4p$ orbitals, respectively. P^α is the α component of the dipole operator ($\alpha = x, y, z$), ω is the incident photon energy, and ω_0 is the energy of the unperturbed p_m levels. The incident (final) polarization of the photons is $\epsilon(\epsilon')$ and

± 1 labels the orbital sublattice. Γ is the lifetime of the excited state. $p_m P^\alpha s = A \delta_{m\alpha}$, where A is a constant. As illustrated in the figure, $\delta\omega_m^n = -\Delta$ for $n = +1, m = x, z$ and $\Delta\omega_m^n = 2\Delta$ for $n = +1, m = y$ and so on.

The origin of the splitting Δ is not specified in the model proposed in [35], but the authors clearly state that one possible source is the Coulomb interaction between the $4p$ conduction band states and the ordered $3d$ orbitals, which raises (lowers) the $4p_m$ levels lying parallel (perpendicular) to the direction of the orbital by $2\Delta(\Delta)$. Authors suggest Δ to be of order several tenths to 1 eV and $\Gamma \sim 5$ eV.

An alternative mechanism, they suggest, comes from the coherent JT distortions of the oxygen octahedra surrounding the Mn atoms that accompanies the orbital ordering, with the long axis always along the occupied $3d - e_g$ orbital.

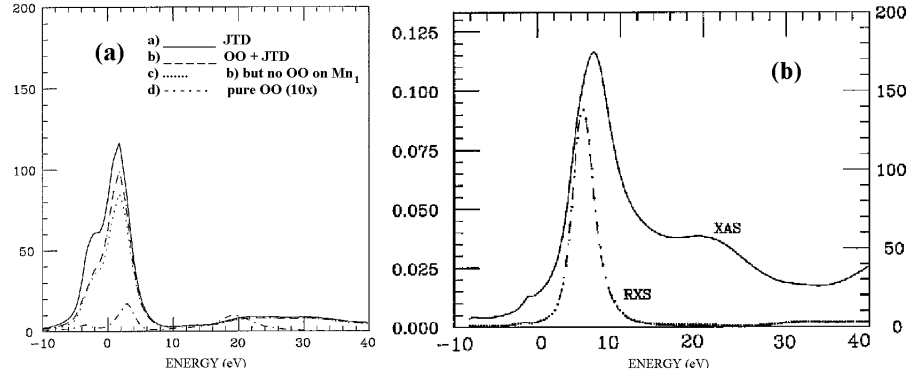


Figure 2.9: (a) Anomalous resonant diffraction intensity (adimensional units) at the $(3,0,0)$ reflections by full potential calculations. (a) Full line: Pure JTD; (b) long-dashed line: JTD plus OO on all Mn atoms; (c) dotted line: same as (b) with no OO on central Mn_1 atom; (d) dot-dashed line: pure OO without JTD ($\times 10$). (b) Mn K-edge unpolarized absorption cross section (Mbarn, left scale) in $LaMnO_3$ and anomalous resonant diffraction signal due solely to JTD, calculated in muffin-tin approximation (adimensional units, right scale). [37].

Working in a linear polarization basis, with $\sigma(\pi)$ polarization perpendicular (parallel) to the scattering plane, one can show that for σ incident polarization, the orbital ordering shown in Fig. 2.8 does not give rise to a σ' polarized scattered beam. For any azimuthal angle Ψ , intensity $I_{\sigma\sigma'}(\Psi) = 0$. In the rotated π' channel,

we have:

$$I_{\sigma\pi'}^{\text{res}}(\Psi) \sim \frac{A^4 \sin^2 \Psi \Delta^2}{[\Gamma^2 + 4(2\Delta - x)^2][\Gamma^2 + 4(\Delta + x)^2]}, \quad (2.2)$$

where $x = (\omega - \omega_0)$. Thus, the model predicts that the scattering is all of the $\sigma \rightarrow \pi'$ type and it has a two-fold azimuthal symmetry, with zeros coming when the incident beam is parallel to z (c axis). The question is whether the observed signal is directly correlated to the orbital ordering or to the JT-distortions of the same symmetry.

Recently, Elfimov [36] and Benfatto [37] et al shown that hybridization between Mn 4p and neighboring Mn 3d with O 2p orbitals is very sensitive to JT-distortions (JTD) and according to their calculations must be the main reason for RXS on Mn K-edge (Fig. 2.9).

2.5 Review of RXS Experiments

First claims of direct observation of OO in the manganites were reported in 1998 by Murakami et al [35]. They studied an undoped sample of $LaSrMnO_3$ and observed a resonant signal at $E=6555$ eV on structurally forbidden (3,0,0) reflection which they attributed to the OO phenomena.

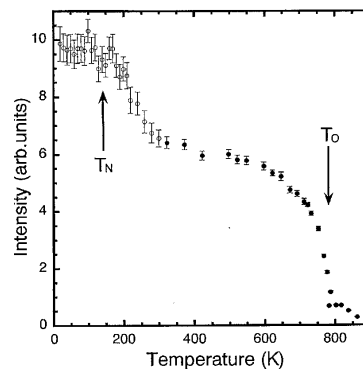


Figure 2.10: Temperature dependence of the normalized intensity of the orbital ordering reflection (3,0,0) at $E=6555$ eV. Open symbols correspond to results obtained at an azimuthal angle $\psi = 127^\circ$ and cooling with a displax cryostat; closed symbols were obtained for $\psi = 90^\circ$ and heating with an oven. [35]

Authors suggested that the the orbital ordered structure is kept after the disappearance of magnetic order. It disappears only after a high-temperature transition to the non-JT distorted phase (See Fig. 2.10) [39], [35]. One year later Endoh et al [30] conducted a similar experiment on a single crystal of $La_{0.88}Sr_{0.12}MnO_3$. They observed resonant enhancement of the (0,3,0) reflection at $E=6552$ eV (See Fig. 2.11 (a)). However, the data quality in not very good due to poor energy resolution and low intensity.

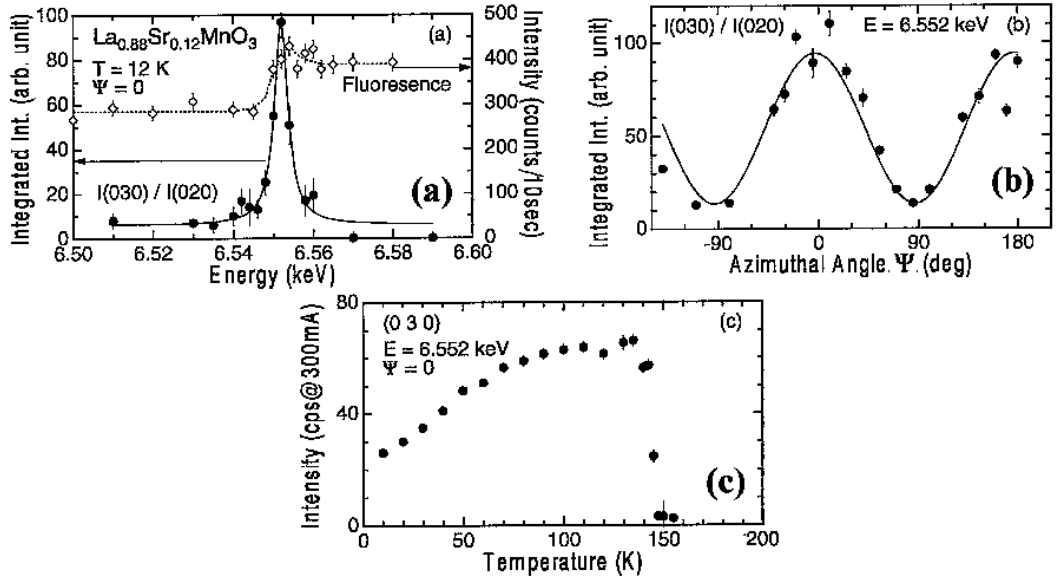


Figure 2.11: (a) Energy dependence of intensity of the orbital ordering reflection (0,3,0) at $T = 12$ K. The dashed curve represents fluorescence showing the resonant energy (6552 eV) corresponding to the MnK -edge. (b) The azimuthal angle dependence of (0,3,0). The solid line is the twofold squared sine curve of angular dependence. (c) Temperature dependence of (0,3,0) peak intensity [30].

Figure 2.11 (b) shows the azimuthal scan, clearly revealing a square of sinusoidal angle dependence of twofold symmetry. Although OO in $La_{0.88}Sr_{0.12}MnO_3$ seems similar to that of $LaMnO_3$, authors observed a marked difference. According to Endoh et al, as shown in Fig. 2.11 (c), OO appears only below $T_{OO} = 145$ K. They suggest that spin and orbital degrees of freedom are coupled because the magnetization is also enhanced below T_{OO} .

Authors conclude that below T_{OO} there appears a long-range structural modulation along the c axis though neither a conventional charge ordering nor a long-range cooperative JT distortion exist.

Recently, Wochner et al [38] studied RXS on the $La_{7/8}Sr_{1/8}MnO_3$ on (003) reflection which is not completely forbidden in the Pbnm crystallographic group. However, they observed a weak resonance (by factor of 6 only) at $E=6554$ eV (See Fig. 2.12 d) in the entire temperature range 50-300 K.

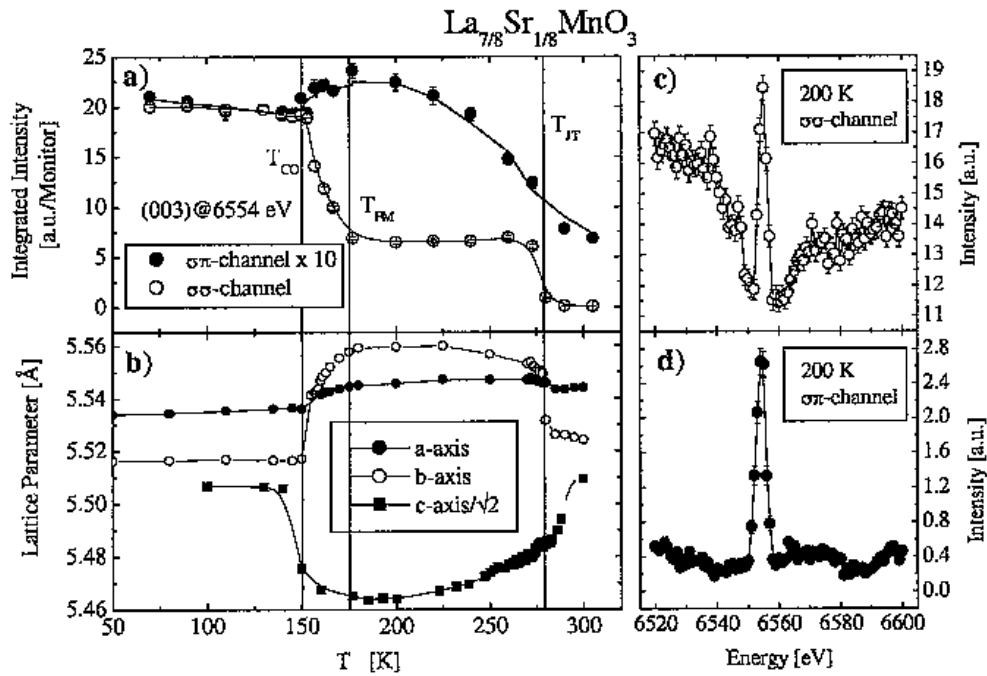


Figure 2.12: Comparison of temperature dependencies for $\sigma\sigma$ – and $\pi\pi$ -component of (003) reflection shown in a) and the lattice parameters (Pbnm-setting) in b). The energy dependence for $\sigma\sigma$ – and $\pi\pi$ -component at 200K is plotted in c) and d), respectively.

2.6 Conclusions from the Experimental Review

Despite the fact that the $La_{1-x}Sr_xMnO_3$ system was extensively studied in the past years, many questions are still not completely understood. Many groups have conducted experiments on the lightly doped system with $x=1/8$ employing one single technique (either neutron scattering or RXS or high-energy scattering).

Simultaneous existence of both OO and CO has never been confirmed. The so-called direct observation of OO by Endoh's group is doubtful since theoretically predicted [37] signal due to JT distortion must be much stronger than the one, related purely to OO. The quality of the data of different groups is not very good. Nowadays it is possible to improve its quality using synchrotron sources of the new generation, like for example Advance Photon Source (APS).

Therefore it was decided to study systematically the $La_{1-x}Sr_xMnO_3$ system ($x \approx 1/8$) by means of careful macroscopic measurements, both resonant and non-resonant X-Ray scattering, as well as neutron scattering. The aim is to obtain a complete picture of interplay between charge, orbital and spin ordering in this system.

Chapter 3

Preparation and Characterization

3.1 Ceramics

Polycrystalline ceramics have been prepared by the standard ceramic route, although some methodological improvements and additional investigations were needed to achieve compositions with specific stoichiometries.

The starting materials are La_2O_3 , $SrCO_3$ and MnO_2 with 99.99 % purity.¹ La_2O_3 is fired in air at 900 C to eliminate the adsorbed water and carbon dioxide. After this procedure the weight of the powder is about 5% less than the weight of the same powder before dehydration. The raw materials are weighted to desired stoichiometric ratio with accuracy better than 0.1 %. The lanthanum oxide is taken directly from the oven at 200 °C after dehydration to avoid water absorption during the weighting-in procedure.

The powders are mixed in a planetary mix installation with addition of 2-propanol (1 ml per 5 g of powder) and zirconium balls (1 ball per 2 g of powder). It is very important to have the powder well mixed before the reaction, otherwise the materials will not react properly during calcination; on the other hand a long-time exposure to zirconium can lead to contamination. Ultrasonic probe analysis shows that the best samples can be obtained after 2 hours of milling at a rotation rate of 200 rpm. After that the average size of the particles in the powder mix was about is 3 μm . There are no particles observed with the size larger than 12 μm . (See Fig. 3.1)

¹Produced by Aldrich GmbH

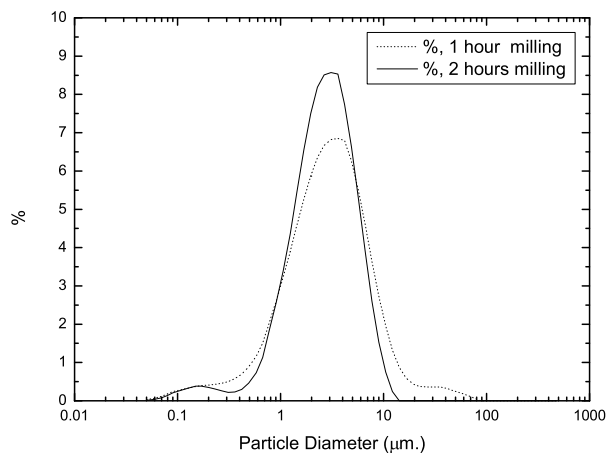


Figure 3.1: Distribution of the particle size after milling as determined by the ultrasonic probe analysis.

After mixing the powder-liquid suspension is dried up at 70 °C. Dry powder is separated from the zirconium balls using a sieve, placed in a zirconium crucible and fired in air at 1100 °C for 12 hours. Afterwards the material is ground manually and mixed again in the planetary mix for 2 hours with zirconium balls and 2-propanol. Then the material is dried up again and fired at 1200 °C for 12 hours.

After the regular grinding, milling and drying procedure, the material is mixed with a binder solution ² to form the feed rods for crystal growing. The powder is put into a stainless steel form and pressed in an uniaxial press by applying an isostatic pressure of 20 KN into rods of a shape of about $4.4 \times 4.4 \times 44 \text{ textmm}^3$. The best rods are obtained using 1 gm of binder per 4 gm of powder.

The rods are placed in a platinum crucible into a furnace first at 500 °C for 6 hours to evaporate the binder and then sintered at 1300 °C for 12 hours. After sintering the furnace cooled down at the rate of 120 °C per hour. Cooling rates faster than 120 °C lead to bending of the rods.

²consisting of 7g PAF 35 and 2g PEG 400 glue per 100 ml H_2O

3.2 Characterization

3.2.1 X-Ray Powder Diffraction

The quality of the sintered rods was investigated by several means. First, phase composition was studied on Phillips X'Pert MRD machine using X-Ray powder diffraction (XPD). Small amounts of samples were thoroughly ground and then the thin layers of the materials were glued on a glass plate. A typical diffraction pattern is shown in Figure 3.2. The XPD scan parameters are shown in the inset of Fig. 3.2 The data are consistent with those measured on the same compounds by other groups [40]. No additional peaks corresponding to non-stoichiometries and impurities were found. The accuracy of the XPD analysis is about 1-2%.

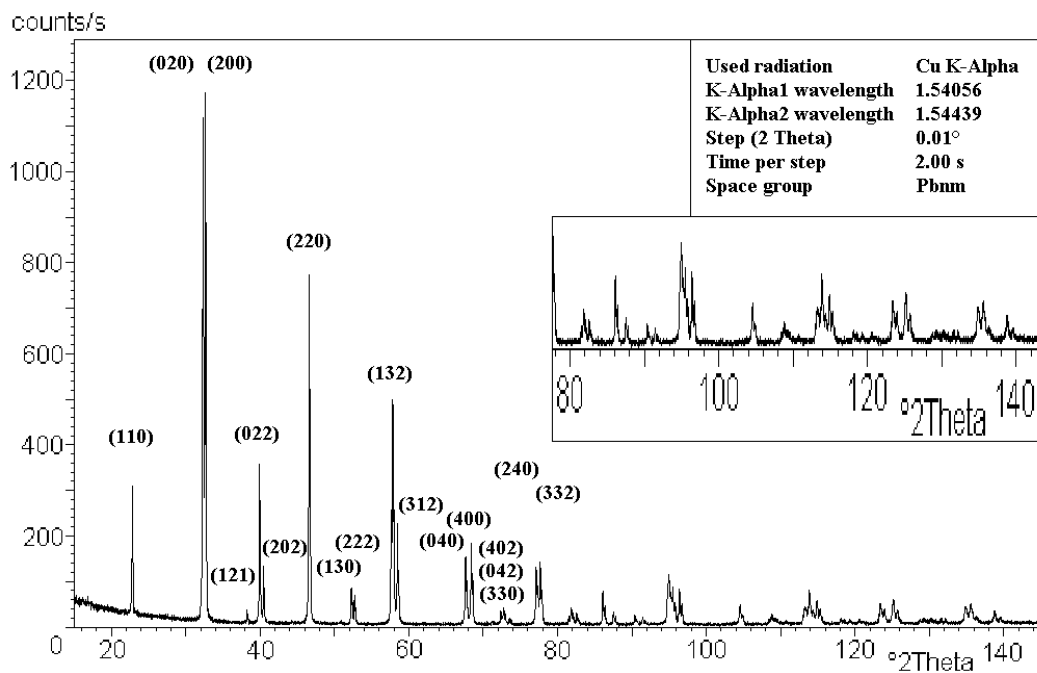


Figure 3.2: Typical XPD pattern for $La_{0.875}Sr_{0.125}MnO_3$ sample.

3.2.2 Atom Emission Spectroscopy with Inductively Coupled Argon Plasma

Analysis of the chemical compositions was done by Central Chemical Department of the Institute of Solid State Research using atom emission spectroscopy with inductively coupled argon plasma (ICAP) [41], [42] at Thermo IRIS machine. 10 mg of ground powder were solved in 3 ml HNO_3 (65%) with addition of H_2O_2 (35%) and filled in a volume of 100 ml. The measured percentage of the chemical elements (La, Sr, Mn) in the volume were as expected from the preparation. The relative accuracy of this method was about 1-2 % in relatively terms for main elements (La, Mn) and 10 % for Sr.

The theoretical and measured quantities for the $La_{0.875}Sr_{0.125}MnO_3$ powder sample are shown in Table 3.1 for nominal composition $La_{0.875}Sr_{0.125}MnO_3$.

Element	Theoretical, %	Measured, %	Accuracy, %
La	51.46	51.2	± 1.02
Sr	4.66	4.65	± 0.47
Mn	23.41	23.0	± 0.46

Table 3.1: Amounts expected from preparation and results from ICAP measurement

3.3 Crystal Growing

3.3.1 Introduction

Single crystals of the manganites may be grown in several ways. One of them is a flux method, which involves cooling a charge of the oxides with a flux closed in a platinum crucible at the rate of 1 mm through the liquidus. The flux growth method allows growth in lower than melting point temperature (about 1500 °C) but is hardly suitable for growing pure mixed crystals with a defined composition. The other method is the floating-zone method (FZM) with radiation heating.

Figure 3.3 is a compilation of Curie temperature data for the $La_{1-x}A_xMnO_3$ systems. The variations presumably reflect differences in the composition, stoichiometry and defect

structure. Agreement is achieved between the results from different laboratories when the preparation conditions are well controlled, as in the growth of single crystals by the FZM.

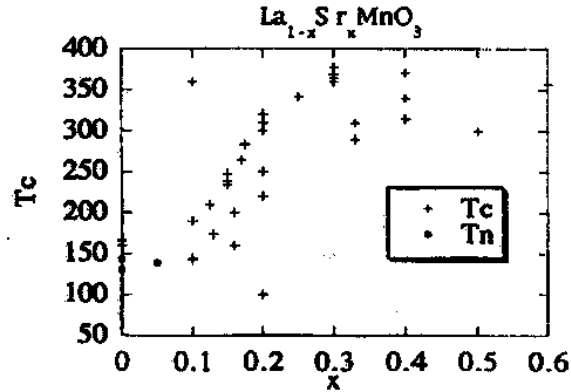


Figure 3.3: Compilation of measured Curie temperatures in nominal $La_{1-x}Sr_xMnO_3$ compounds from [15].

Due to the fact that this method ensures a high purity of the growing crystals, it is widely used for the growth of manganite single crystals by several groups [43], [44], [7], [45], [46], [47]. However some problems for this method still remain, namely:

- The electrical and magnetic properties reported are different for the same nominal composition of the crystals, which makes it difficult to conclude definitely on the properties of the compound itself;
- Little is known about the factors controlling cation ratio, homogeneity of elements distribution and defect structure in the crystals grown by the FZM.

Therefore it was decided to grow a series of $La_{1-x}Sr_xMnO_3$ ($x \approx 1/8$) crystals with slightly different nominal compositions.

3.3.2 Experimental Procedures

The manganite single crystals were grown using Crystal Systems Inc. FZT 4000H Optical Floating Zone Furnace (Figure 3.4) in the Institute for Crystallography, RWTH, Aachen.

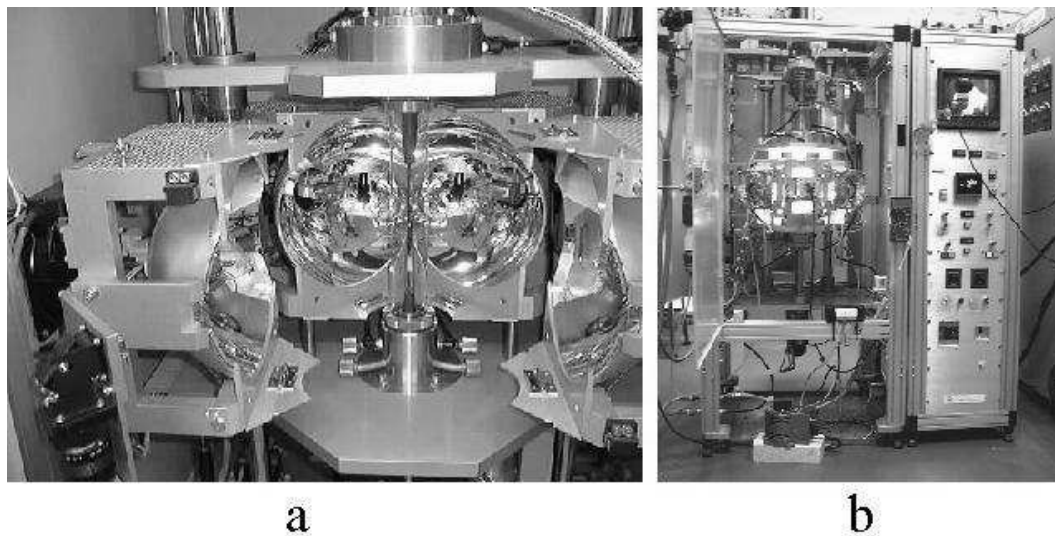


Figure 3.4: CSI machine with four ellipsoidal mirrors (a). Common view (b).

The experimental arrangement is presented in Figure 3.5. The small zones of sintered manganite rods with desired composition were symmetrically heated by the light beam from four halogen lamps (1500 KW each).

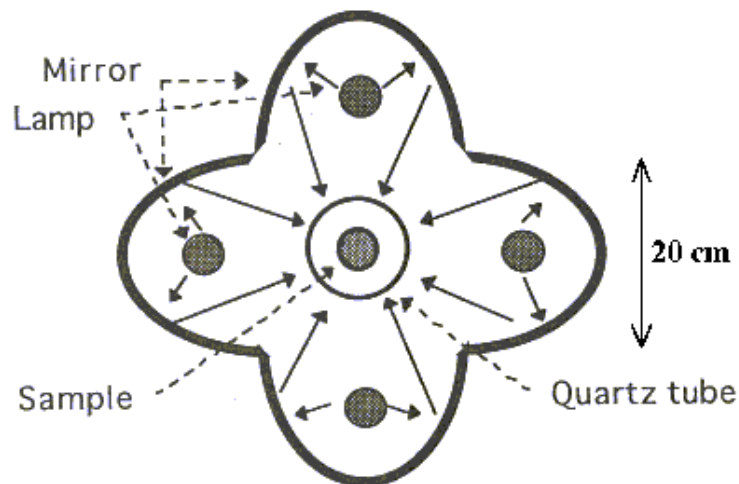


Figure 3.5: Schematic illustration of the four mirror image furnace. Upper view.

The rods were connected to the shafts using platinum wires. Both the upper and lower shaft were rotated in opposite direction at a rate of 20-30 rpm. (Figure 3.6 a) The

independent rotation of the rods produces a homogeneous heating environment and allows modification of convection inside the molten zone. At the initial stage of the heating, both the feed (upper) and seed (lower) rod are set apart by a distance of a few mm. As the heating progresses, both ends of the rod begin to melt (Figure 3.6 b). At this stage, the upper feed rod is moved downwards and the seed rod is moved upwards until they touch each other. Finally, the length of the molten zone is adjusted so that its diameter is almost the same as that of the rods (Figure 3.6 c). After this, the mirror system is moved upwards at a rate of 5-8 mm/hour and the upper shaft with the feed rod is pushed downwards at a rate of 3-5 mm/hour. The single growth always took place in normal air pressure. The temperature of the melt was not measured during the growing process because the melt reflected the light of the arc lamps making pyrometric temperature measurements impossible. After finishing the growing process the power of the lamps was decreased at a rate of 0.5% per minute.

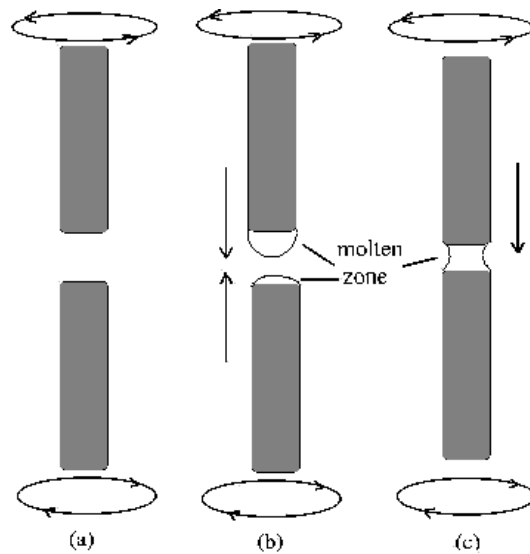


Figure 3.6: Schematic illustration of 3 stages of growing process. Front view.

3.3.3 Results

Well-crystallized specimens were obtained for the $La_{1-x}Sr_xMnO_3$ system with $x=0.105$, 0.115, 0.125 and 0.135. A few experiments were performed also at $La_{1-x}Sr_xMn_{0.95}Fe_{0.05}O_3$

and $La_{0.5-x}Nd_{0.5-x}Sr_xMnO_3$ since ceramic materials of this materials show some very interesting features ([48], [49]). Unfortunately it seems that it is difficult to grow single crystals with additional Fe and Nd doping. The samples obtained of these systems had numerous cracks and defects. More investigations in this field are planned for the future.

An example of the grown specimen is shown in Figure 3.7. The ingots have a glossy black colour and normally consist of a few single crystals with a size of about $4 \times 4 \times 4 \text{mm}^3$.

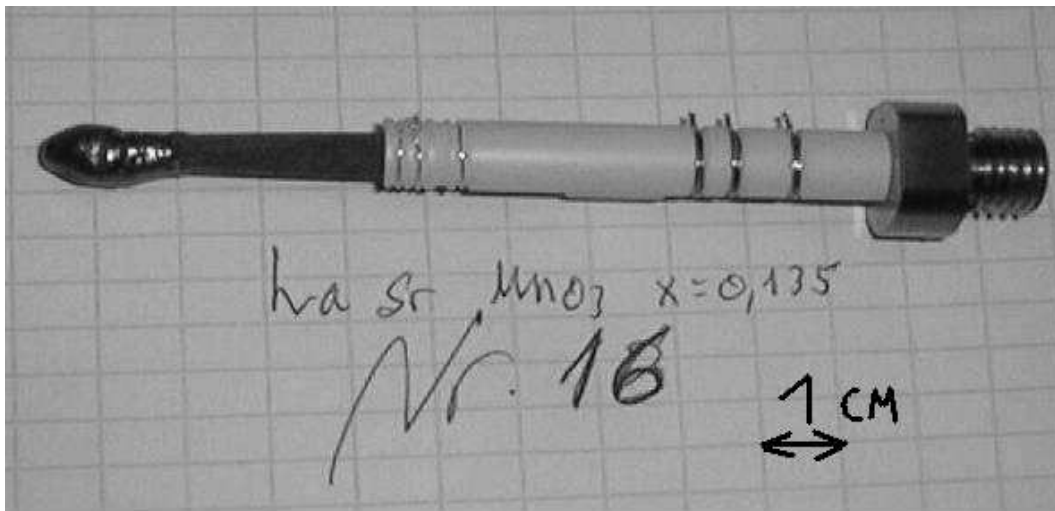


Figure 3.7: Grown crystal on top of seed rod.

The single crystals parts were first found in the grown ingots using an optical microscope. Then there were cut by diamond wire and polished by diamond paste. The quality was evaluated first by careful observation of the surface using an optical microscope. When it was found that the crystals did not have any cracks or other defects, the quality and orientation of the crystals were examined by means of Laue pictures taken at different points on the polished surfaces. A typical Laue pattern is shown at Figure 3.8. Afterwards the samples were characterized by several means.

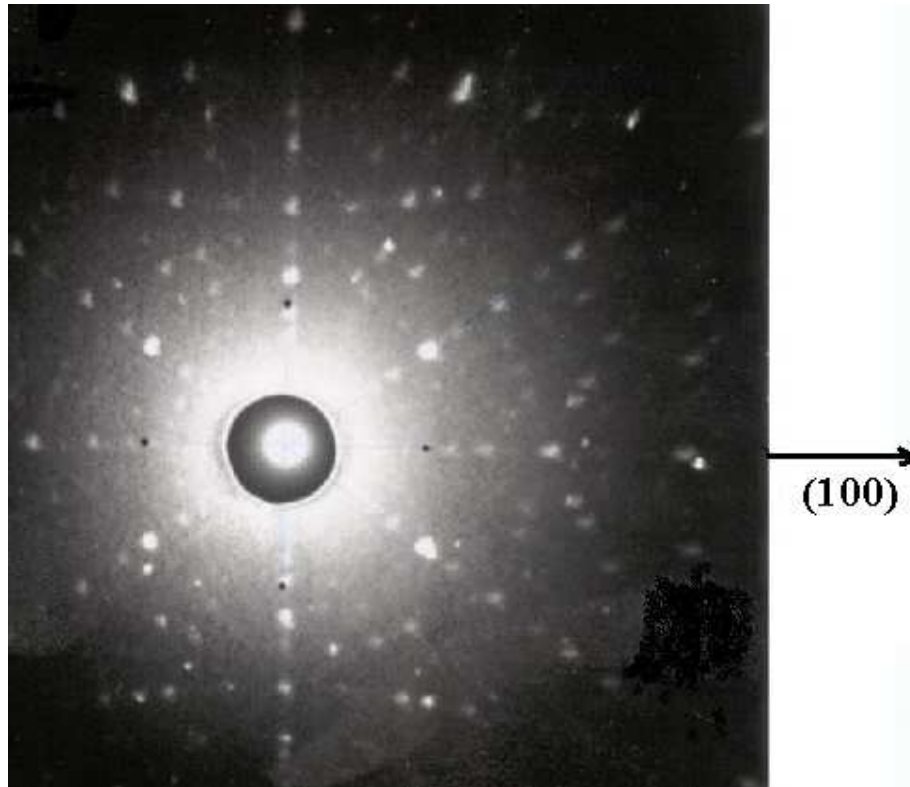


Figure 3.8: Laue picture taken from $La_{0.875}Sr_{0.125}MnO_3$ crystal. The polished surface is (1 0 0) plane of the crystal, the distance between the X-Ray source and the sample is 3 cm.

3.4 Characterization

3.4.1 Microprobe Analysis

Distribution of the elements in different areas (See Fig. 3.9) on the crystal surface was measured by the electron ion spectroscopy (EIS) with the beam size of about $10 \mu\text{m}$. The results of the measurements on $La_{0.875}Sr_{0.125}MnO_3$ crystal are shown in Table 3.2.

Accuracy of La and Mn concentration measurements was 0.5% in relatively terms. Accuracy for Sr measurements was lower - about 2% because of its lower concentration. This method allows to measure only relative amounts of elements excluding oxygen ions and provides only qualitative information about the distribution of the elements on the sample. No standard probe was available for calibration measurement.

As it can be seen from Table 3.2, the La, Mn and Sr concentrations are quite homogeneous. Impurity phases such as La_2O_3 or MnO_2 could not be detected.

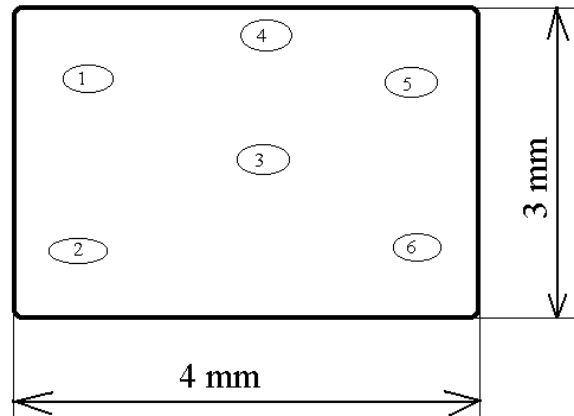


Figure 3.9: Areas on the crystal surface investigated by electron ion spectroscopy. $La_{0.875}Sr_{0.125}MnO_3$ sample

Spot Number	Concentration, %		
	La	Mn	Sr
1	47.99	46.57	5.44
2	47.83	47.27	4.90
3	49.15	46.71	4.14
4	47.99	46.41	5.60
5	47.39	46.34	6.27
6	48.17	46.38	5.45

Table 3.2: Concentration of the elements on the surface of the $La_{0.875}Sr_{0.125}MnO_3$ single crystal measured by electron ion spectroscopy, see approximate coordinates in Fig.3.9

3.4.2 Magnetization

The magnetization measurements of four single crystals with different stoichiometry were performed at Quantum Design Magnetic Property Measurement System using a small

field of 100G for samples with $x=0.105$, $x=0.125$ and $x=0.135$; and 500G for the sample with $x=0.115$. The magnetization normalized on the sample mass is plotted as a function of temperature in Fig. 3.10 (a,b,c and d for $x=0.105$, 0.115, 0.125 and 0.135 respectively). All magnetization measurements were performed during warming, no hysteresis effect with warming or cooling was found.

The observed transition from paramagnetic to ferromagnetic state are of second order type, therefore the transition temperatures can be determined on the reciprocal scale of magnetization (See. Fig. 3.11). For our samples measured Curie temperatures are as follows: $x=0.105$ sample - 170 K, $x=0.115$ sample - 185 K, $x=0.125$ sample - 190 K and $x=0.135$ sample - 215 K. The transition temperatures are systematically increasing with x contents which is consistent with literature [7].

Magnetization of all four crystals is slightly decreasing at lower temperature which is a well-known phenomena attributed to anizathropy of the samples. In our case we may suspect presence of smaller domains with different orientation in the balk of the crystals which leads to a preferable orientation of magnetic spins.

3.4.3 Resistivity

The resistivity of the crystals was measured using a standard four-wire method. The samples were mounted on the top of a cold finger of a closed-cycle cryostat. Temperatures between 6 K and 300 K could be reached. The resistivity for samples $x=0.105$, $x=0.125$, $x=0.125$ and $x=0.135$ is plotted versus temperature in Figure 3.12 (a,b,c and d respectively).

The anomalies in vicinity in Fig. 1.7 seem much stronger it may have following explanation: since the size our samples is relatively small ~ 0.4 cm, effects of the electrical current path may be crucial. Thus, the current doesn't flow through all parts of the crystal but probably through domains with lesser resistivity or on the crystal surface. For better quality of resistivity measurement one should obtain larger crystals and cut a narrow long sample exclusively for these purposes.

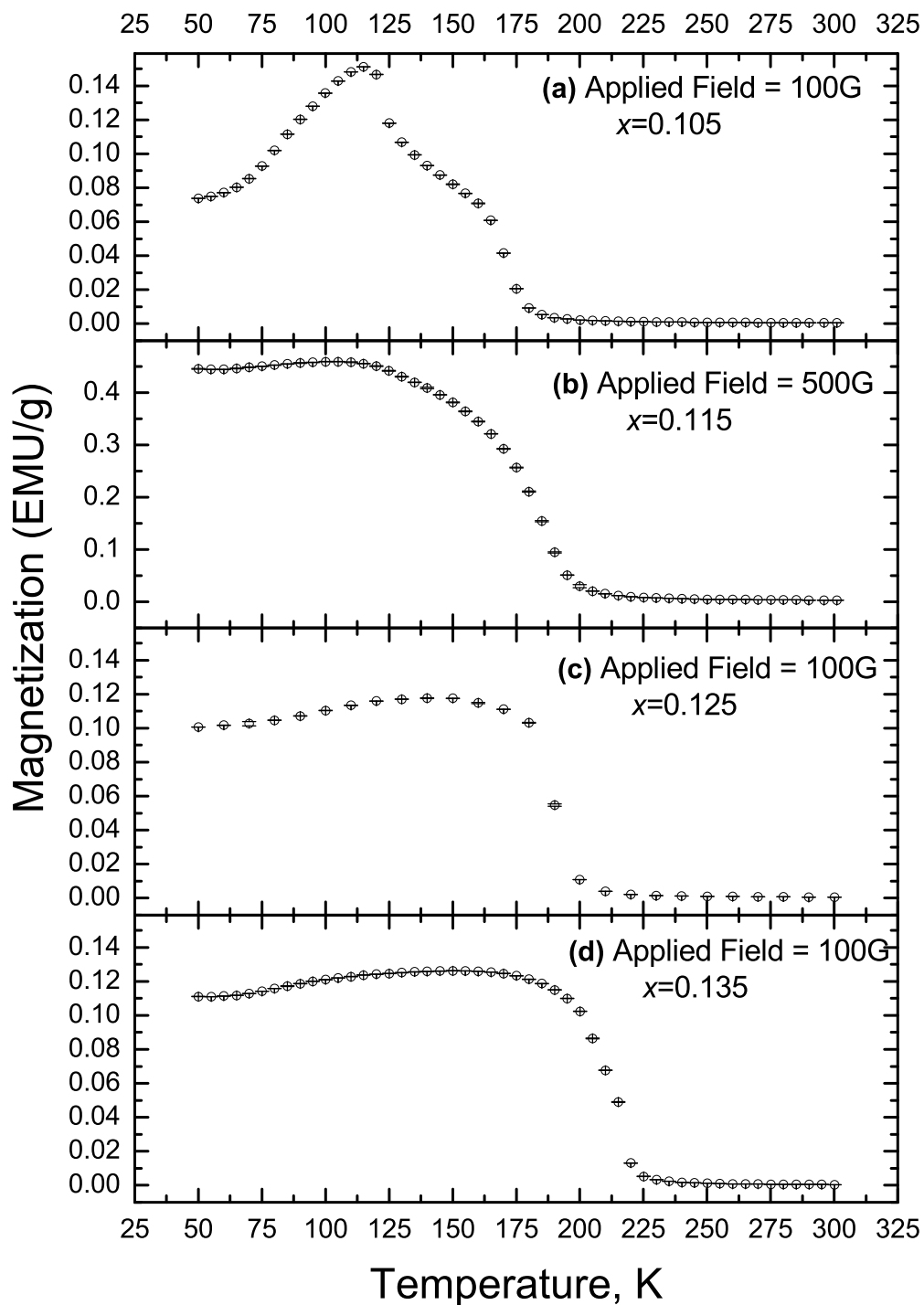


Figure 3.10: Magnetization of the four $La_{1-x}Sr_xMnO_3$ single crystals.

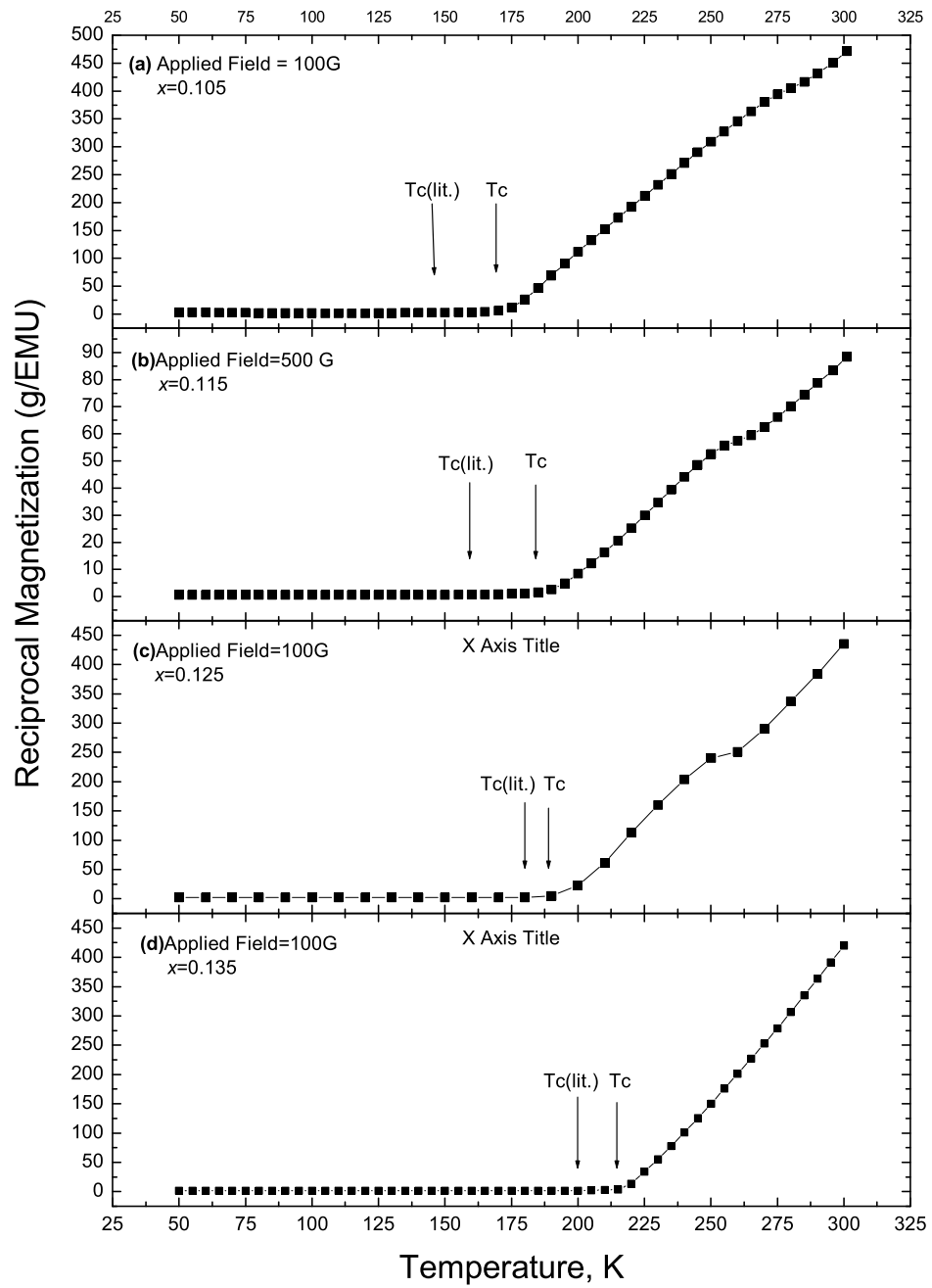


Figure 3.11: Reciprocal magnetization of the four $La_{1-x}Sr_xMnO_3$ single crystals. Transition temperatures are indicated with T_c symbols, transition temperatures as are taken from Fig. 2.1 are indicated with $T_c(\text{lit.})$.

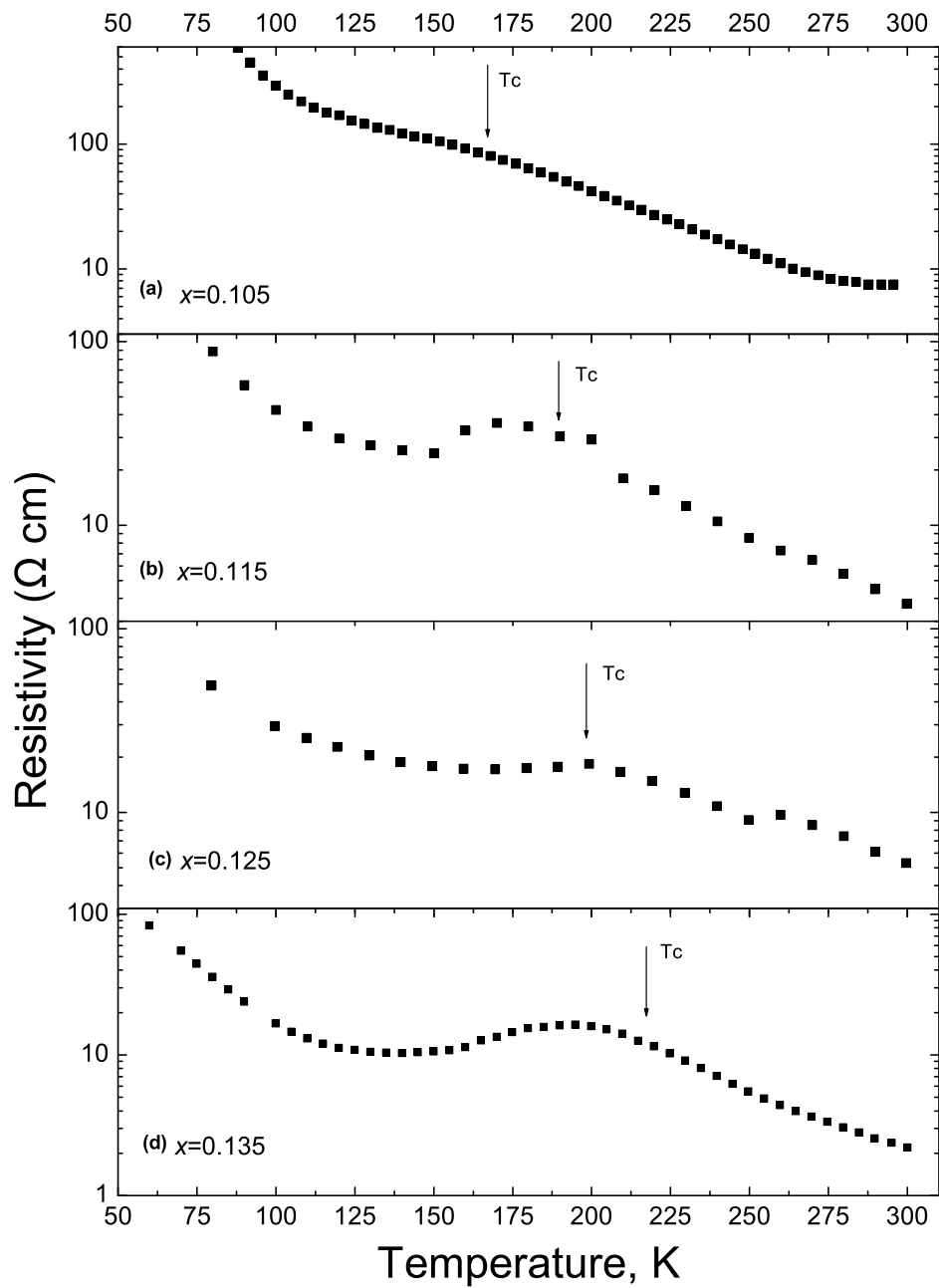


Figure 3.12: Resistance of four $\text{La}_{1-x}\text{Sr}_x\text{MnO}_3$ single crystals with different x contents in zero field. Transition temperatures are shown as from magnetization measurements Fig. 3.11.

Chapter 4

Experiments with X-Ray Scattering

4.1 Resonant X-Ray Scattering

The RXS measurements of the $x=0.125$ and $x=0.135$ samples were undertaken at the 6ID-D (Mu-Cat sector) beamline located at the APS (Argonne National Laboratory, USA). The RXS measurement of the $x=0.115$ sample was done at W1 beamline at HASYLAB, DESY. The (100) planes of the samples were aligned within the scattering plane using a standard four-circle vertical scattering geometry. (Figure 4.1). The incident beam was focused by a bent cylindrical mirror and monochromatized by a pair of Si(111) crystals, giving an energy resolution of about 0.5 eV at 6ID-D and about 5 eV at W1. A closed-cycle cryostat was used to cool down the samples. To discriminate the different polarization states of the scattered beam, a polarization analyzer setup was also employed using a Cu(220) analyzer crystal, which gives a scattering angle of 95.6 degree when the incident photon energy is set at the Mn K -edge. This corresponds to the $\sigma - \pi$ scattering geometry.

At room temperature, all Bragg reflections of the $x=0.125$ sample are single-peak both along longitudinal and transverse directions. A rocking-curve scan on the (200) reflection of the $x = 0.125$ sample is shown in Fig. 4.2. Moving the sample surface around the incident beam indicates no peak splitting or multiple component. The other two samples ($x=0.115$ and $x=0.135$) have smaller grains at the periphery of the crystals.

Fluorescence near the Mn K-edge was measured on the background far off in the reciprocal space from any Bragg reflections by tuning the incident X-ray energy in the

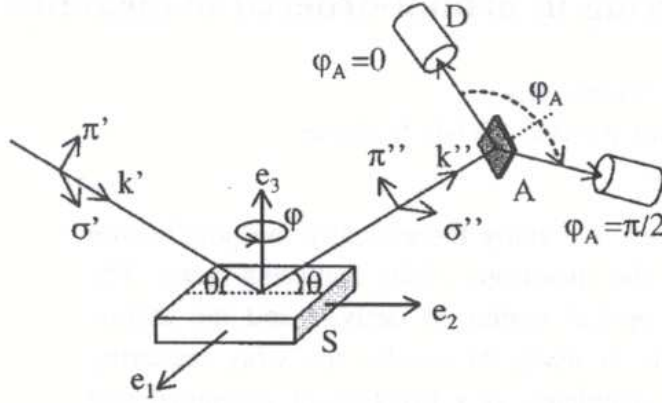


Figure 4.1: The schematic view of the experimental arrangement (refs. [50], [51]) which consists of a sample crystal (S), analyzer crystal (A) and photon detector (D). φ is the azimuthal angle and φ_A is the analyzer angle. \vec{k}' (\vec{k}'') is the photon momentum and $\vec{\pi}'$ ($\vec{\pi}''$) and $\vec{\sigma}'$ ($\vec{\sigma}''$) are the polarization of the incident (scattered) photon.

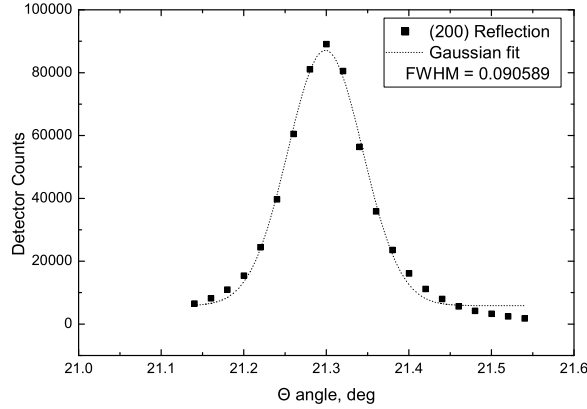


Figure 4.2: Rocking curve on the (200) reflection of the $x = 0.125$ sample at room temperature. Gaussian fit is also shown.

range of 6500-6600 eV and integrating the emitted fluorescence by rocking a graphite (004) analyzer. (See Fig. 4.3). Besides the maximum of fluorescence intensity at the white-line ($E = 6555.5$ eV), small anomalies attributed to $1s \rightarrow$ local $3d$ ($E = 6539.5$ eV) and $1s \rightarrow$ neighboring $3d$ (6548.5 eV) [52] transitions can be seen.

A huge resonant enhancement (by the factor 200) of the intensity of the forbidden reflection (1,0,0) was observed between the inflection point ($E = 6552.5$) and the "white-

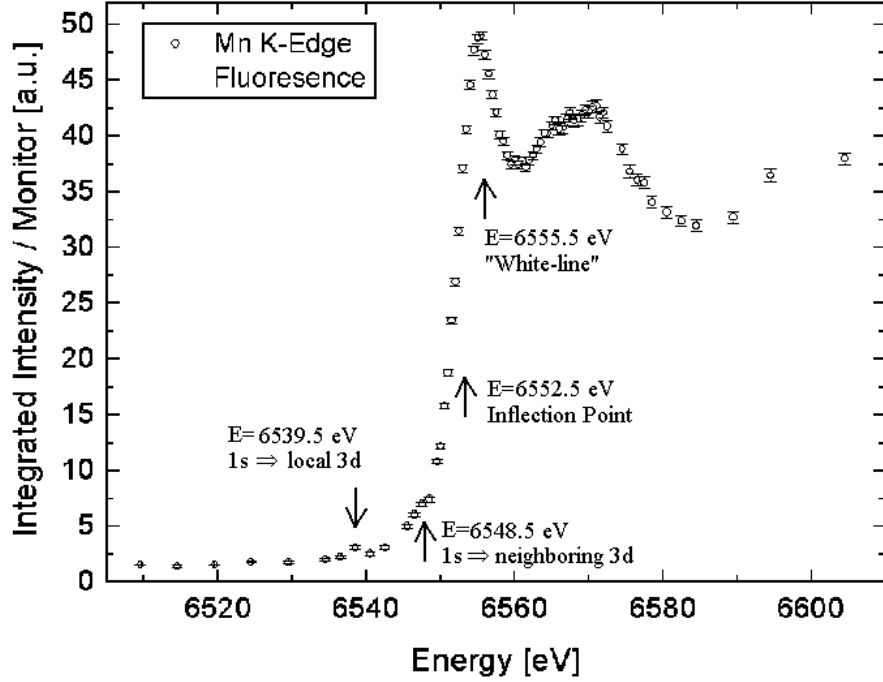


Figure 4.3: Fluorescence at the Mn K -edge. $T=300$ K, $x=0.125$ sample. Tabulated energy for Mn K -Edge (single ion) is 6539 eV (inflection point).

line" ($E = 6555.5$) of the absorption spectrum. The energy dependence of the (1,0,0) reflection of the $x=0.125$ sample at different temperatures is shown in Figure 4.4. All samples have identical energy dependences in the whole temperature range from 10 K to 300 K. The largest enhancement occurs at $E = 6554$ eV. Second resonance peak having less enhancement was observed at $E = 6566$ eV, sometimes followed by even more fine feature - a very narrow (1.0 eV width) peak which can be attributed to multiple charge scattering due to the *Umweganregung* [53] effect. This peak disappears completely with rotating the azimuthal angle.

The data shown in Fig. 4.4 is not corrected by the calculation of absorption coefficient, it will be done in Section 4.4.

Using polarization setup, it was confirmed that the scattered beam of (1, 0, 0) is predominantly $\sigma \rightarrow \pi$ scattered (see Fig. 4.5), which is an indication of a dipolar transition ($1s \rightarrow 4p$).

Complete measurements of the temperature dependences of resonant (1,0,0) ((3,0,0)

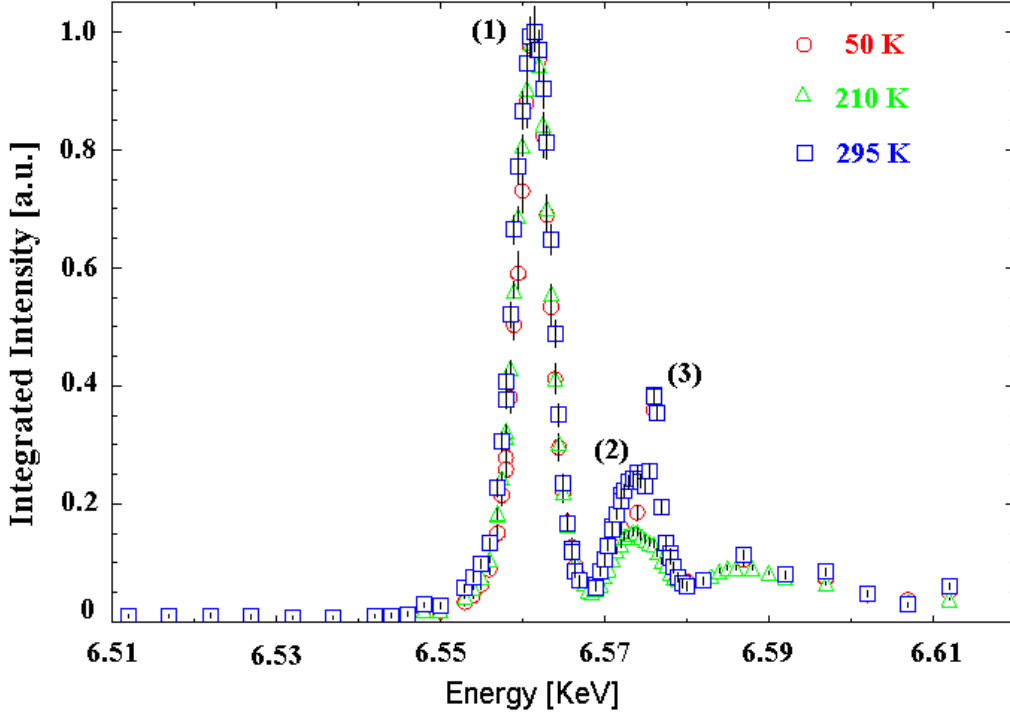


Figure 4.4: Resonant enhancement of the forbidden $(1,0,0)$ at the Mn K -edge. ($x=0.125$ sample) at different temperatures normalized at the maximum. (1) Main peak, (2) Second peak and (3) Multiple scattering peak.

for $x=0.115$ sample) scattering are shown in Figures 4.6 (c) ($x=0.115$), 4.7 (c) ($x=0.125$) and 4.8 (c) ($x=0.135$). In the same figures magnetization and resistivity measurements are also shown. Curie temperatures are indicating with vertical lines as defined in Figure 3.10 and literature. [7].

Peak splittings along the longitudinal direction of the Bragg $(2,0,0)$ reflections were identified between 160-270K ($x=0.115$), 150-260K ($x=0.125$) and 120-230K ($x=0.135$), where the $(1,0,0)$ and $(3,0,0)$ peaks are split along the transverse direction. This effect can be attributed to the JT distortions. Q-area scans for the $x=0.125$ sample around $(1,0,0)$ reflections are shown in supplement A. At low temperatures ($T=50$ K) is a single peak, then it splits up into two peaks in the intermediate temperature range, and it is again single peak at room temperature.

Figure 4.9 shows the azimuthal scan obtained by rotating the crystal ($x=0.135$) by

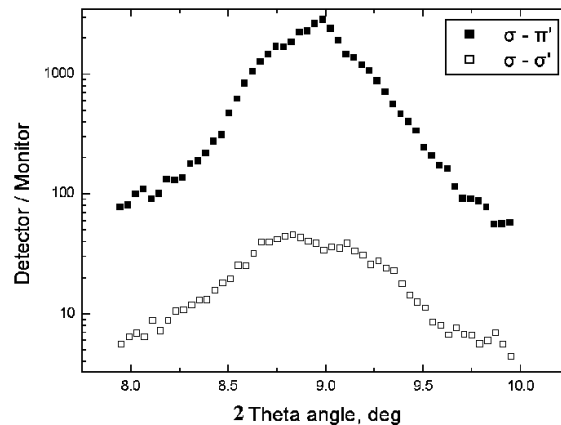


Figure 4.5: Rocking curve scan of the resonant (100) reflection in $\sigma - \pi'$ and $\sigma - \sigma'$ polarization geometries. Note the logarithmic scale of the intensities.

angle Ψ around the scattering vector kept at (3 0 0). The intensity of the (3,0,0) reflection was normalized by the intensity of the fundamental (2,0,0) reflection for the same Ψ value.

The resonant intensity exhibits almost a sinusoidal-square angle dependence with periodicity of about 150 deg. Theoretically, minimum of scattering intensity is expected at the angle $\Psi=0$ when the crystal c axis is normal to the scattering plane, and maximum at $\Psi=\pm 90$ deg when the c axis is in the scattering plane.

4.2 High-Energy X-Ray Scattering

Experiments with high-energy scattering on the same crystals were performed at the 6ID-D beamline at the APS. The standard four-circle vertical scattering geometry was used, a large-area detector was placed behind the samples (See Fig. 4.10).

Figure 4.11 shows a typical pattern obtained from scattering of high-energy photons (88 keV) on the $x=0.125$ sample. It was obtained by rocking the sample $\pm 5^\circ$ in φ angle. It shows a good quality of the crystal. Almost all Bragg reflections can be indexed except a few very weak ones which come from grains of different orientation in the bulk of the crystal. Other three samples ($x = 0.105, 0.115, 0.135$) have similar patterns but with a larger amount of unidentified reflections from foreign grains. These grains do not affect the RXS measurements where the scattering occurs in the upper 3-micron layer of the

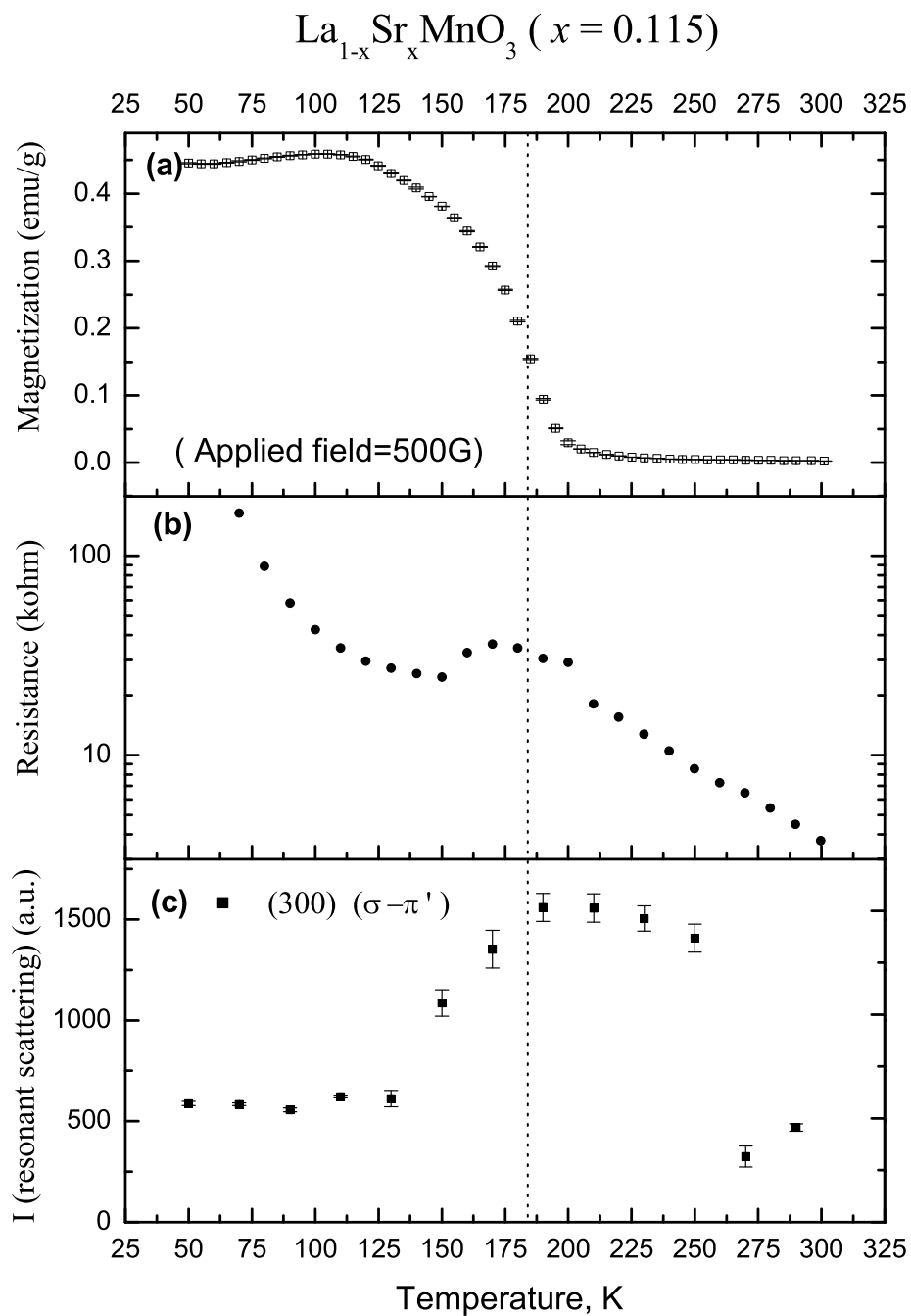


Figure 4.6: Temperature behavior of magnetization (a), resistivity (b), intensity of (1,0,0) reflection (c). $x=0.115$ sample, $\Psi = -90^\circ$. Curie temperature is indicated with vertical line as defined in Figure 3.10 and literature [7].

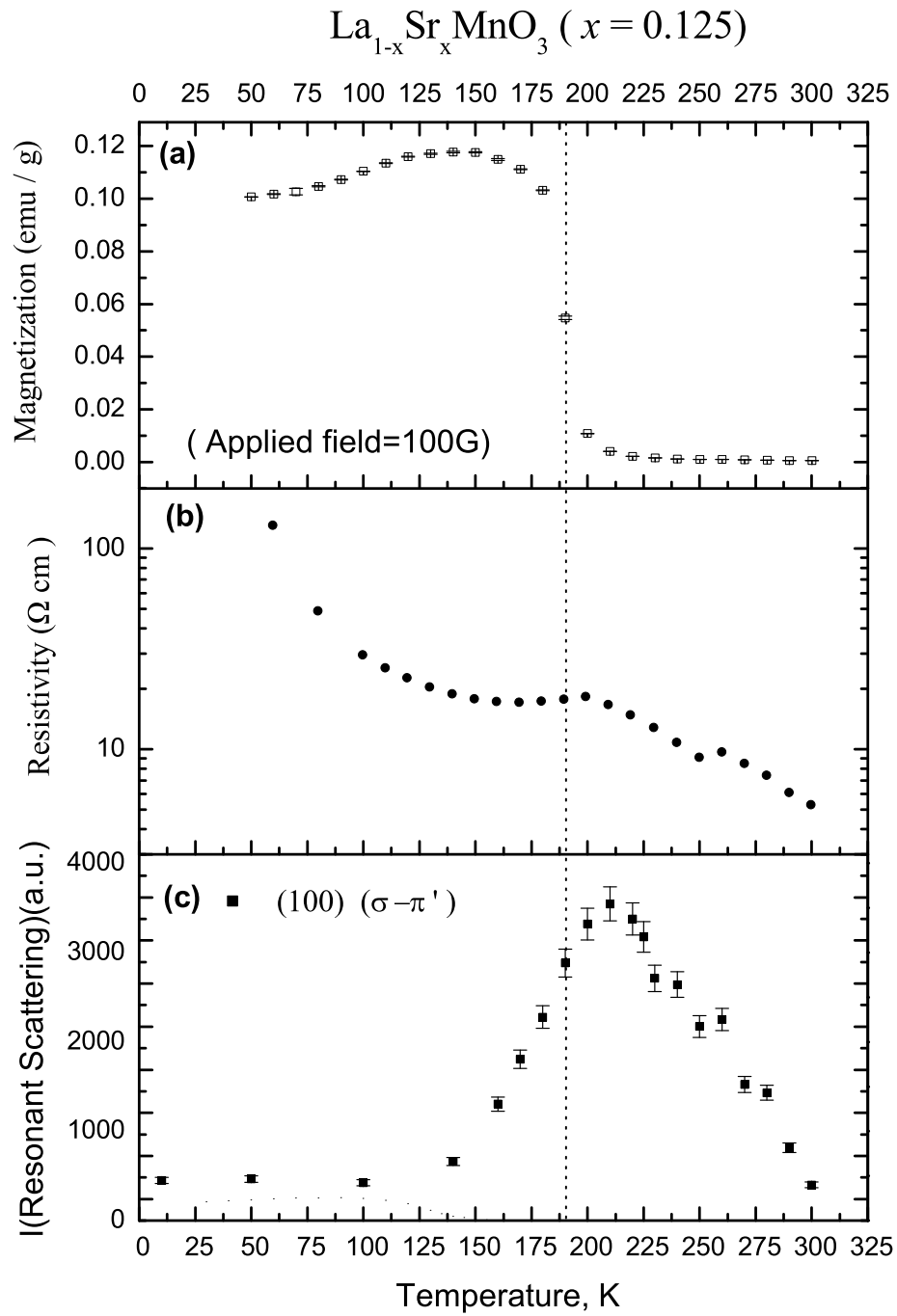


Figure 4.7: Temperature behavior of magnetization (a), resistivity (b), intensity of (1,0,0) reflection (c). $x=0.125$ sample $\Psi = -90^\circ$. Curie temperature is indicated with vertical line as defined in Figure 3.10 and literature. [7].

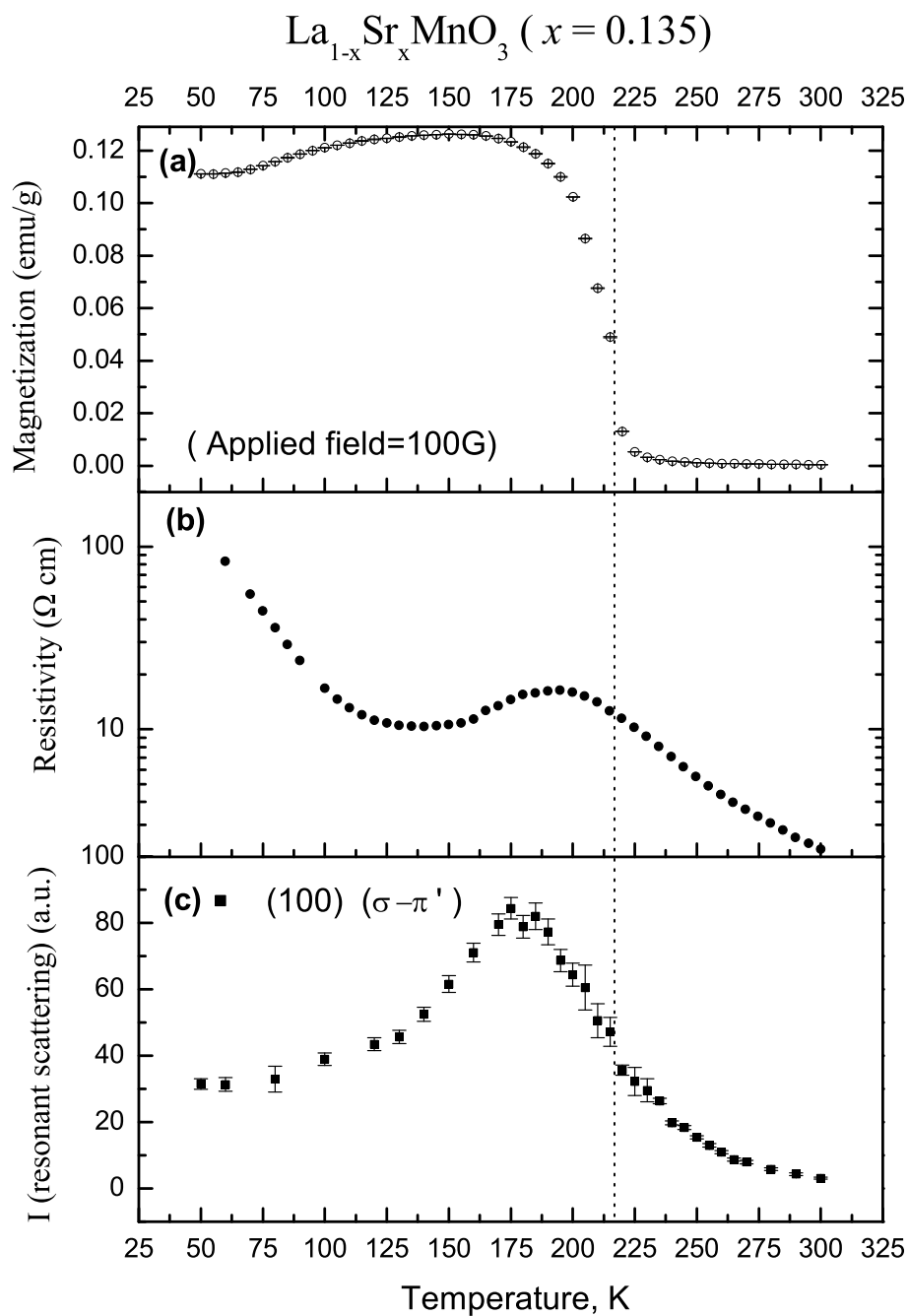


Figure 4.8: Temperature behavior of magnetization (a), resistivity (b), intensity of (1,0,0) reflection (c). $x=0.135$ sample $\Psi = -90^\circ$. Curie temperatures is indicated with vertical line as defined in Figure 3.10 and literature. [7].

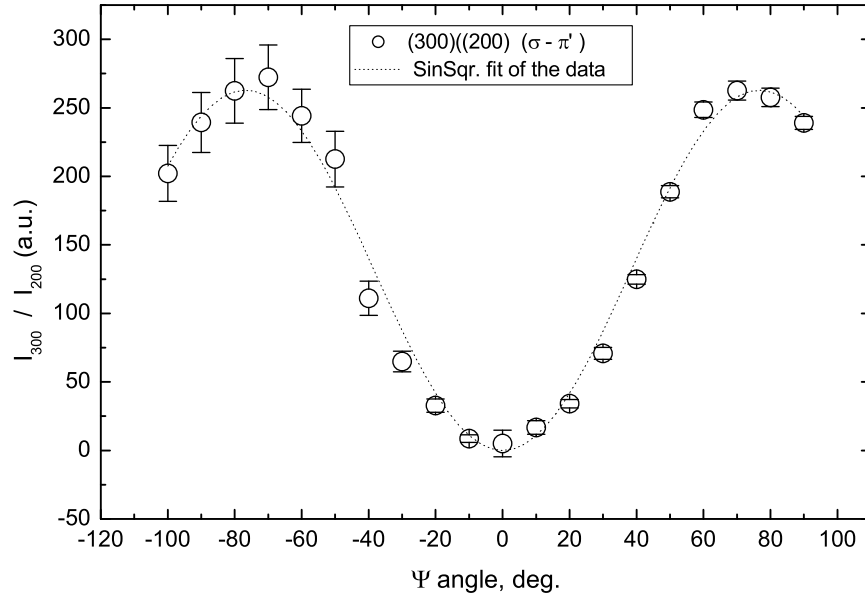


Figure 4.9: Azimuthal dependence of the intensity of (3,0,0) reflection normalized by the intensity of the (2,0,0) Bragg reflection. $x=0.135$, $T=220\text{K}$, $E=6554\text{ eV}$. The angle Ψ is zero when the crystal c axis is normal to the scattering plane and ± 90 deg when in the scattering plane.

sample surface. In contrast, high-energy photons of 88 keV can penetrate through the whole 5mm-thick sample. The area detector which is situated at the distance of 50 cm from the sample can detect reflections in the reciprocal space up to $(\pm 4, 0, 0)$.

Superstructure reflections with modulation vector $(h \pm 0.5, k \pm 0.5, 0)$ with h, k, l being integer or half-integer were found in the entire temperature range 10-300 K. The origin of these reflections will be discussed in the next sections. No superstructure reflections changing their intensities in temperature were found, most probably due to technical problems. Short-time exposures of the area-detector were not enough for detection of weak superstructure reflections due to their low intensities, on the other hand, long-time exposures lead to saturation of the detector elements which causes huge broadening of the spots from main Bragg reflections.

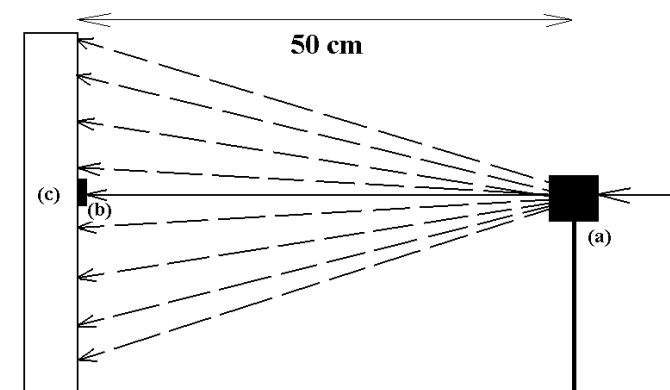


Figure 4.10: Experimental set-up of the high energy experiment. (a) - sample, (b) - direct beam stopper, (c) - large-area detector.

4.3 Non-resonant X-Ray Scattering

Non-resonant X-ray scattering experiments on the manganites were performed at the W1 beamline located at HASYLAB, DESY. As in the RXS experiments, the standard four-cycle vertical geometry was used. A Ge (111) analyzer crystal was used to improve the spatial resolution. The incident beam was tuned to $E = 9500$ eV for the $x=0.115$ sample and to $E = 10000$ eV for the $x=0.105$, $x=0.125$ and $x=0.135$ samples, which roughly corresponds to the maximum of flux for this beamline. The (1 0 0) planes of the samples were aligned within the scattering plane. The sample were mounted on the coldfinger of a closed cycle cryostat which itself was fixed on a standard Huber Eulerian cradle.

At low temperatures superstructure reflections which do not belong to the crystallographic group $Pbnm$ were detected at various positions (See Figure 4.13) in the (ac) -plane with modulation vector $(h, 0, \frac{k}{2})$ for samples $x=0.115$, $x=0.125$, $x=0.135$. A typical longitudinal l -scan is shown in Figure 4.12.

In the (ab) -plane satellite reflection with modulation vector $(h \pm 0.25, k \pm 0.25, 0)$ were found only around the main (4,0,0) and (5,0,1) reflection (see Figure 4.14). No superstructure peaks were detected around (2,0,0) and (3,0,1) although they were reachable in the present scattering geometry. Other main Bragg peaks were unreachable due to technical reasons - at some angle ω of the sample the Eulerian cradle shadowed the incident beam and also the detector angles 2θ could not exceed a certain value of about 90° .

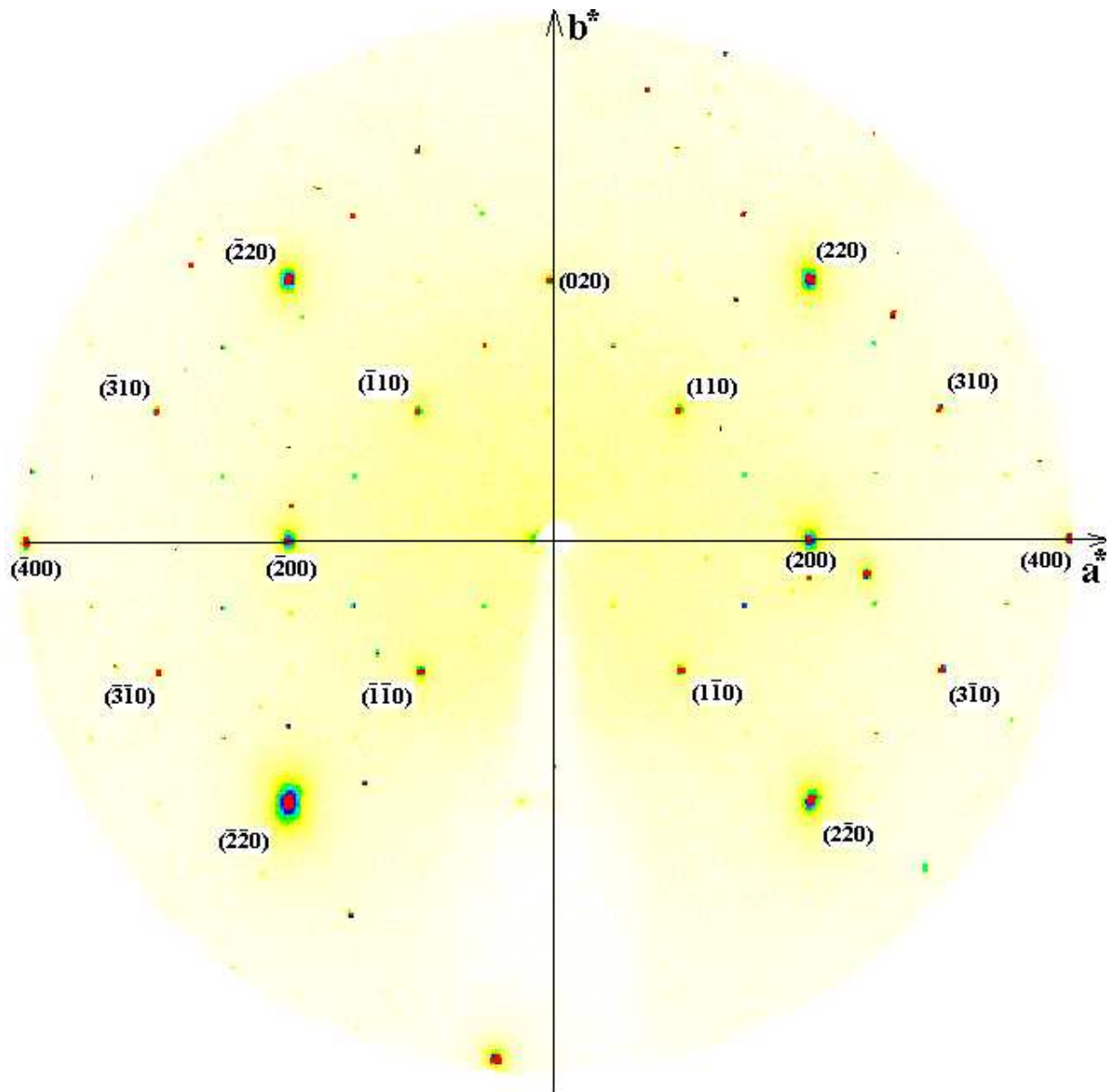


Figure 4.11: High-energy pattern of the $(h, k, 0)$ plane of the $x=0.125$ crystal. $E=88$ keV, $T=300$ K

Approximate boundaries of accessible area are shown in Fig. 4.13 and 4.14 as dashed lines.

The ration of the satellite peak intensity to the adjacent Bragg peak intensity is $1.7 \cdot 10^{-4}$ for the $x=0.115$ sample, $2.9 \cdot 10^{-5}$ for the $x=0.125$ sample and $2.4 \cdot 10^{-6}$ for the $x=0.135$ sample. No superstructure reflections were detected for the sample $x = 0.105$.

In figures 4.15 (a), 4.16 (a) and 4.17 (a) the variations of the integrated intensities with temperature are shown for samples with $x=0.115$, $x=0.125$, $x=0.135$, respectively. No hysteresis was found upon heating or cooling. Peak widths are shown in Figures 4.15 (b), 4.16 (b) and 4.17 (b).

The $x=0.125$ sample has the smallest width of about 0.15° in the low-temperature range. The $x=0.135$ sample has the width of about 0.2° and the $x=0.135$ sample has the largest width of about 0.3° at low temperatures. Below 120 K peak widths of all three samples are not changing with temperature (horizontal line in Figs. 4.15 (b), 4.16 (b) and 4.17 (b)). Above temperature about 120 K all samples begin to exhibit a significant broadening of the satellite peaks (oblique line in Figs. 4.15 (b), 4.16 (b) and 4.17 (b)), which further leads with increasing temperature to their complete disappearing (Fig. 4.15 (b), 4.16 (b) and 4.17 (b)). This transition is of second order type. The transition temperature was defined by the cross-section of the horizontal and the oblique lines and equals to approximately 120-125 K for all three studied samples.

In addition to the satellite peaks with modulation vector $(h \pm 0.25, \pm 0, 25, 0)$, weak superstructure reflections of another type were found in all samples at $(2.5, 0.5, 0)$, $(4.5, 0.5, 0)$ and $(4.5, -0.5, 0)$ positions in the $(hk0)$ zone. These reflections are observed in the entire temperature range (see Figure 4.18). According to Niemöller ([34], they may be attributed to the imperfect destructive interference of adjacent layers in the perovskite structure due to the Sr-doping which introduces distortions in the tilt pattern of the oxygen octahedra ([34]). We suggest they may come just from the twinning of the crystals which is a characteristic feature for all manganites. The lattice constants $a \approx b = c/\sqrt{2}$, therefore $(1,1,0)$ reflection has the same d -spacing as $(2,0,0)$ and $(1/2, 1/2, 0)$ as $(1,0,0)$. Temperature and energy behavior of these reflections look exactly like the one of the main Bragg reflections. The intensities of the "half-integer" reflections are about $3.3 \cdot 10^{-2}$ for the $x=0.115$ sample and $1 \cdot 10^{-5}$ for the $x=0.125$ sample.

It was confirmed that both kinds of superstructure reflections are non-resonant at the

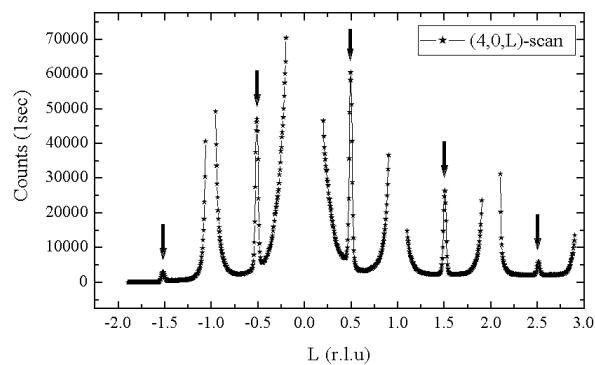


Figure 4.12: L-scan of the $x = 0.115$ crystal, $T=50$ K, $E=9500$ eV

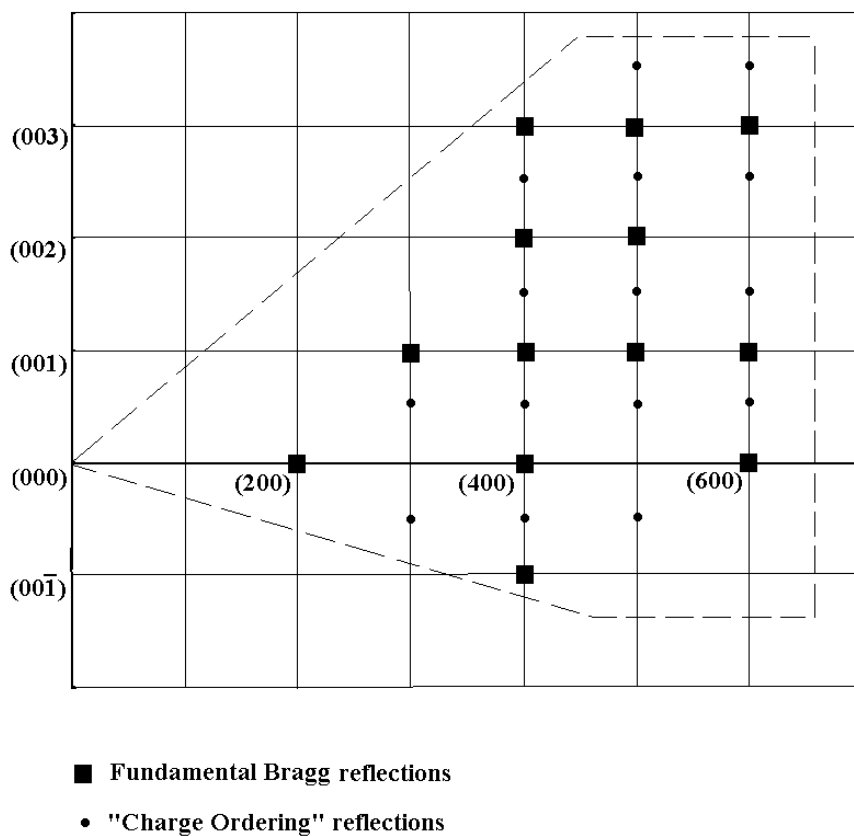


Figure 4.13: The surveyed area in reciprocal space (ac -plane) with different types of reflections observed.

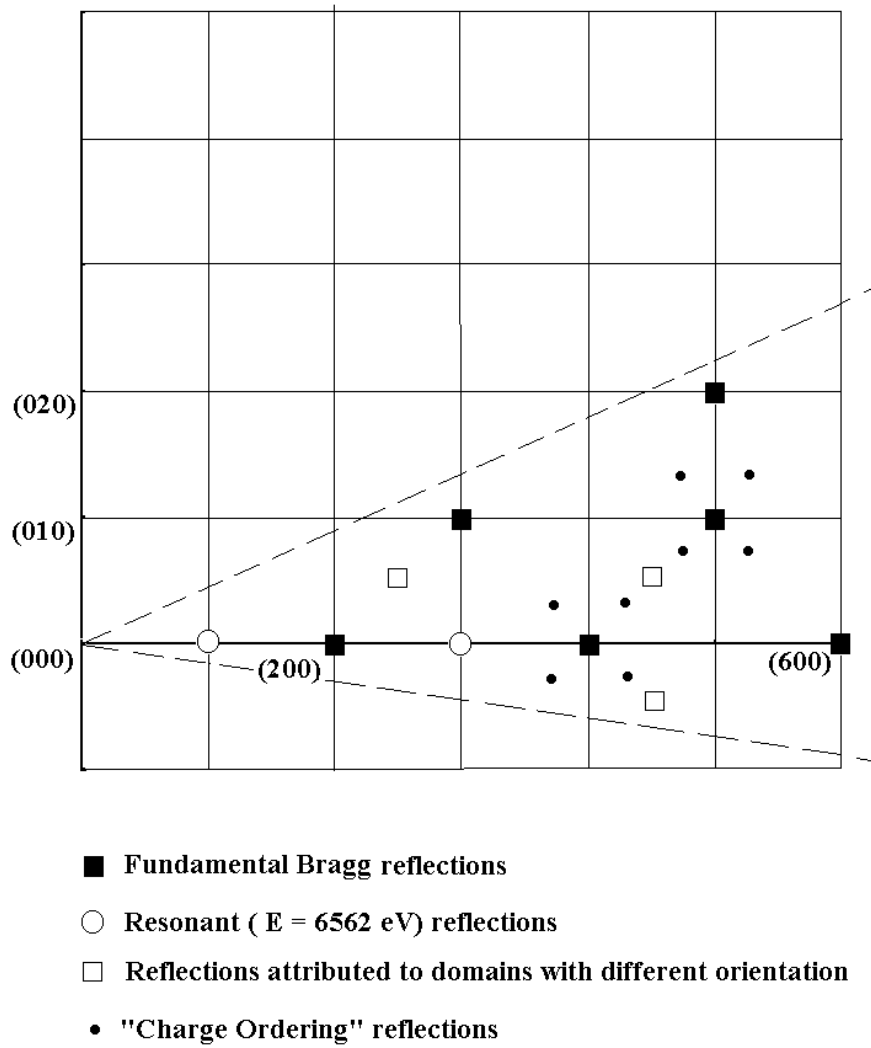


Figure 4.14: The surveyed area in reciprocal space (ab -plane) with different types of reflections observed.

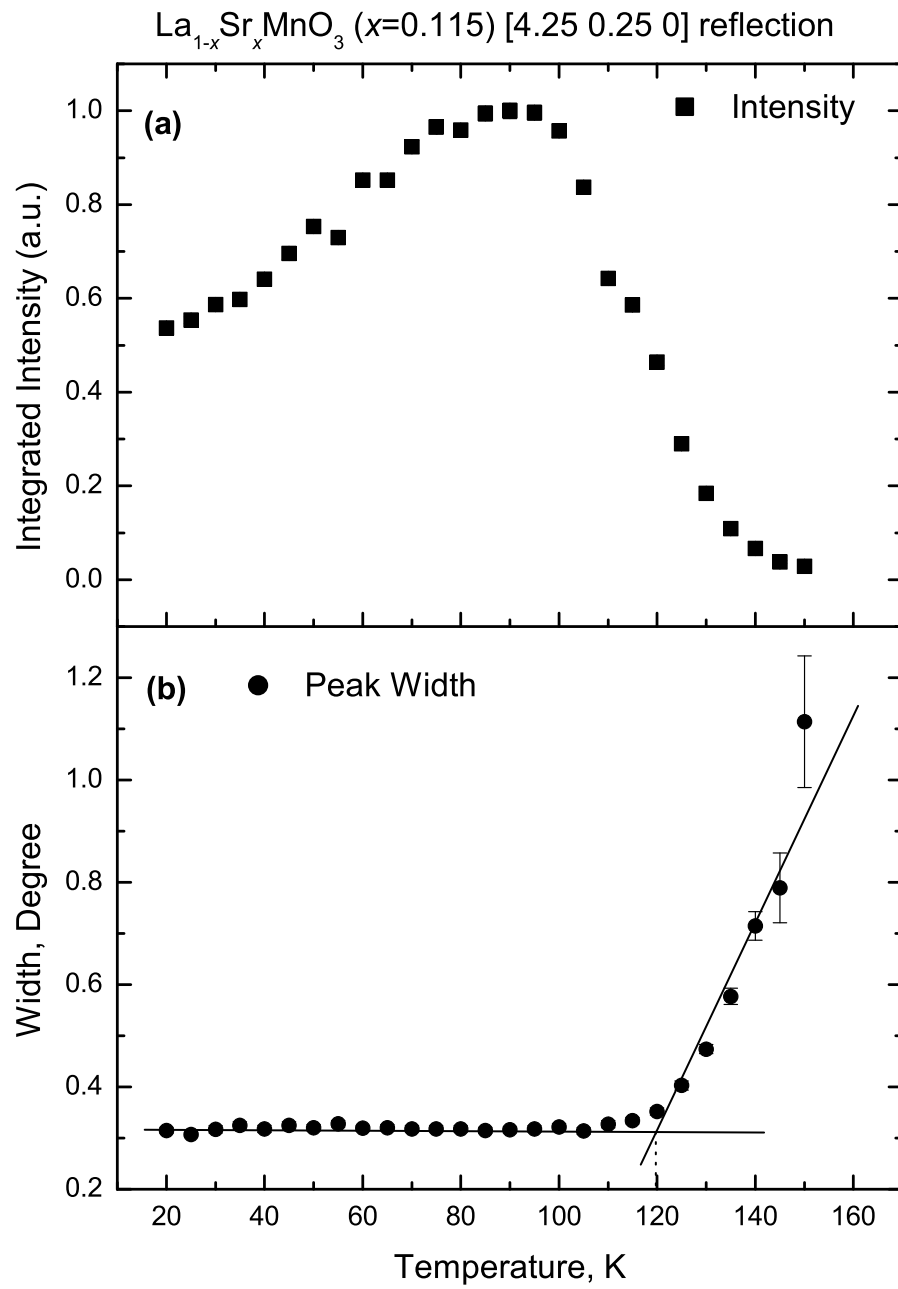


Figure 4.15: Temperature behavior of the integrated intensity (a) and the peak width of the (4.25,0.25,0) reflection of the $x=0.115$ sample (b) taken from transverse scans.

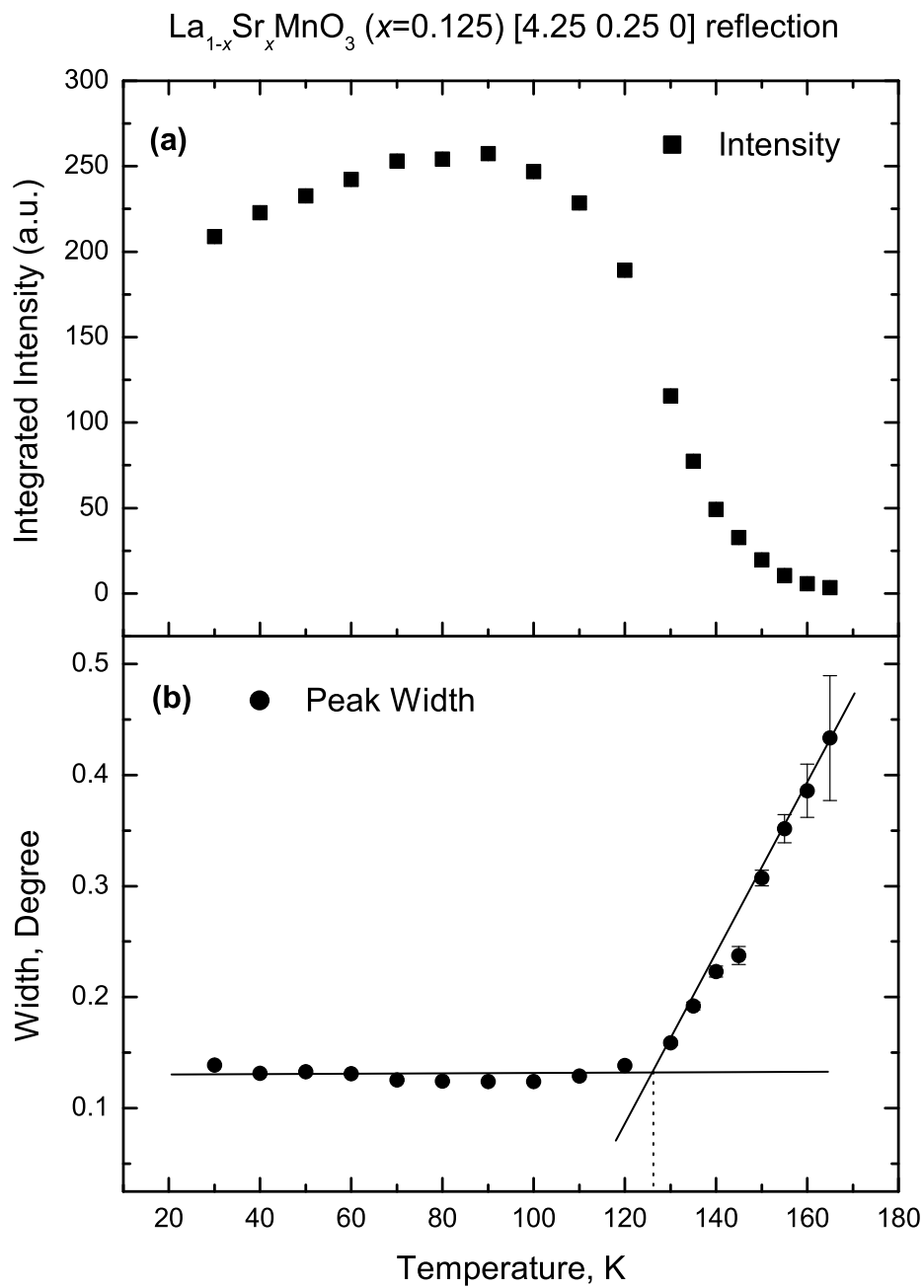


Figure 4.16: Temperature behavior of the integrated intensity (a) and the peak width of (3.75,0.25,0) reflection of the $x=0.125$ sample (b) taken from transverse scans.

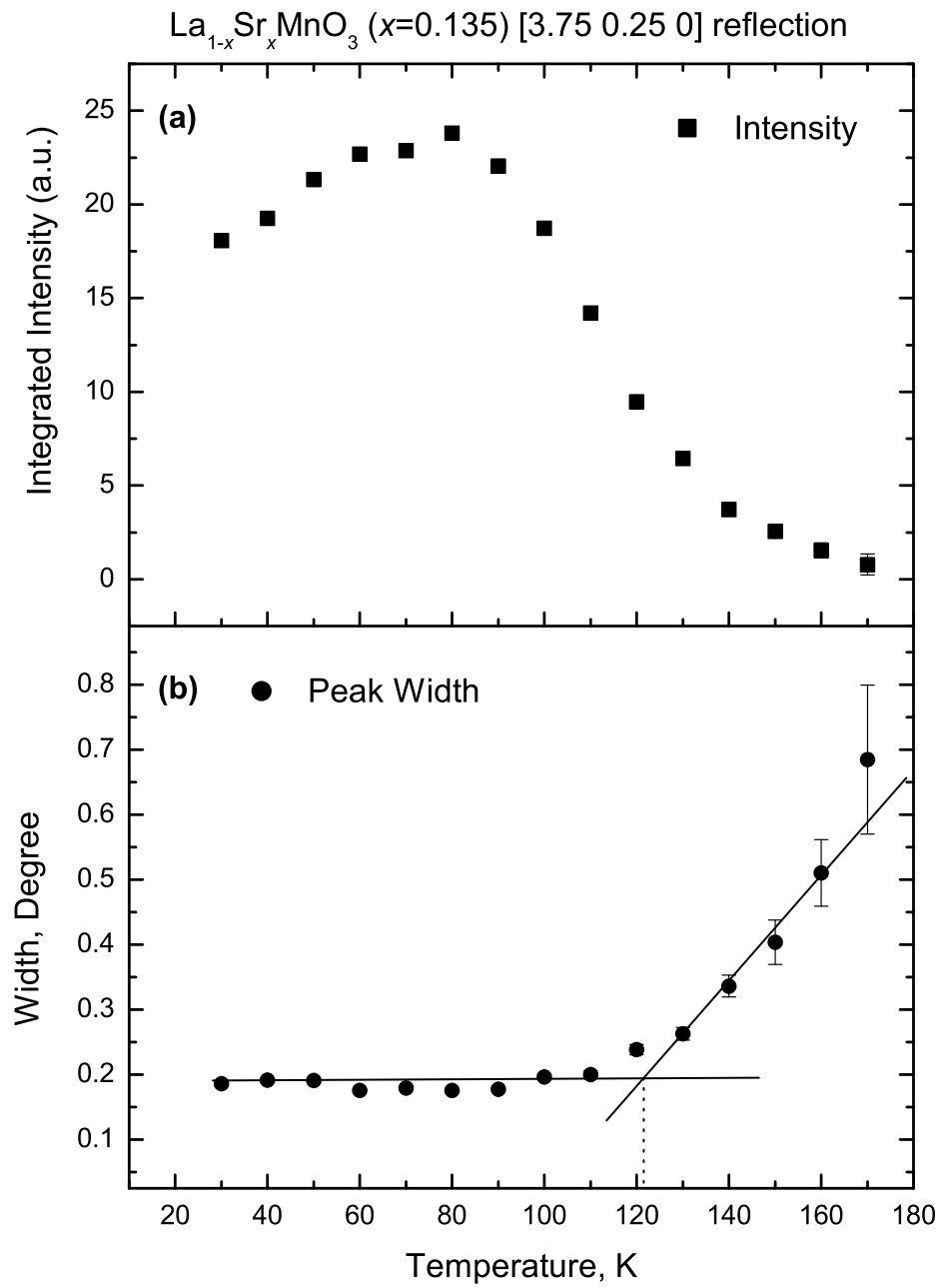


Figure 4.17: Temperature behavior of the integrated intensity (a) and the peak width of (3.75,0.25,0) reflection of the $x=0.135$ sample (b) taken from transverse scans.

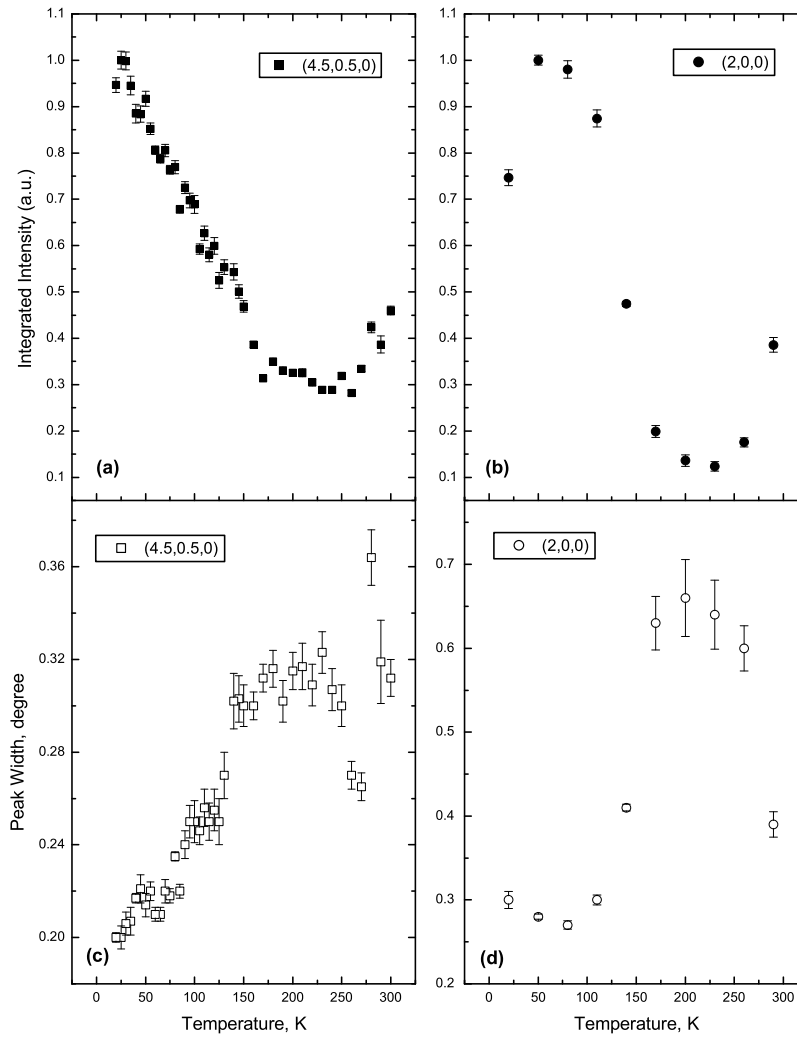


Figure 4.18: Temperature behavior of the intensity and the peak width of (4.5,0.5,0) and (2,0,0) reflections in $\sigma \rightarrow \pi$ geometry for $x=0.115$ sample.

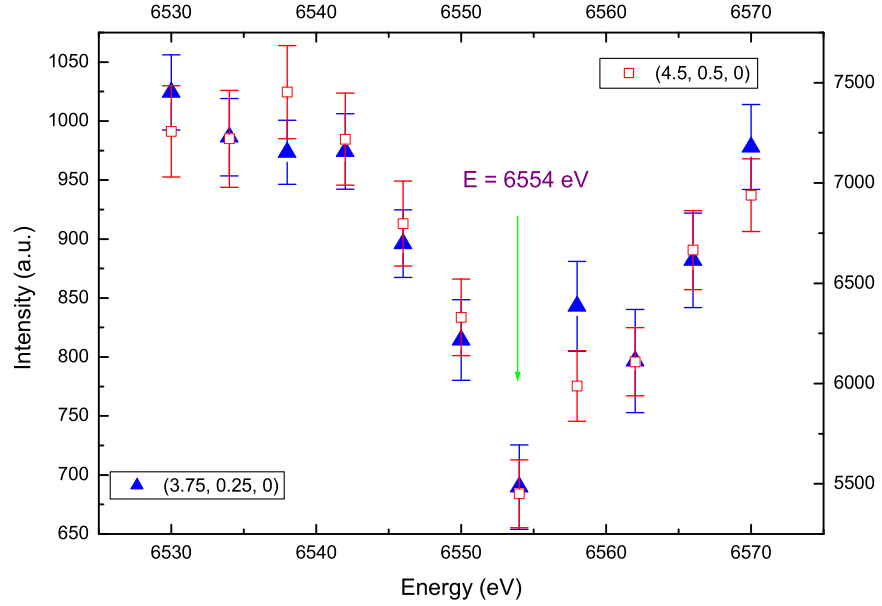


Figure 4.19: Energy dependence of (4.5,0.5,0) and (4.25,0.25,0) peaks in $\sigma \rightarrow \pi$ geometry for $x=0.115$ sample at $T=80$ K

Mn K-edge in contrary to the (1,0,0) and (3,0,0) peaks (See Fig. 4.19). Instead of it they have a local minimum of energy at about $E=6554$ due to increased absorption on manganese. Energy dependences of Bragg reflections have the same kind (See Fig. 4.20).

4.4 Interpretation Of The Experimental Results and Discussion

4.4.1 Resonant X-Ray Scattering

As it was shown by Hupfeld [54], it is necessary to make an absorption correction of the data to compare integral intensities of the resonant signal measured at different energies (Fig. 4.4) The energy dependence of the absorption can be calculated with the following formula [54]:

$$\mu(E) = \mu_1 f(E) + \frac{[I^F(E)(\mu_1 f(E) + \mu_{FS}) - I_1^F f(E)(\mu_1 + \mu_{FS})] \cdot [\mu_2 - \mu_1 f_2]}{I_2^F(\mu_2 + \mu_{FS}) - I_1^F(\mu_1 + \mu_{FS})f_2 - I^F(E)(\mu_2 - \mu_1 f_2)}, \quad (4.1)$$

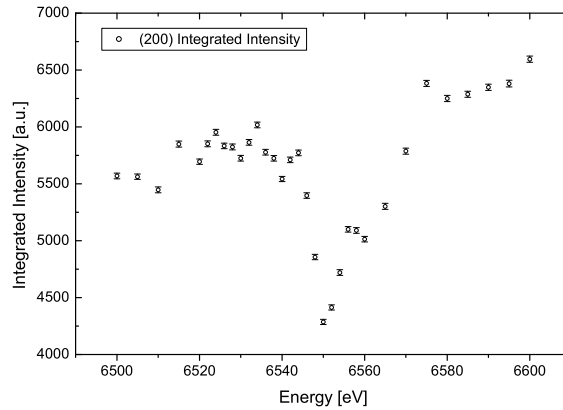


Figure 4.20: Energy dependence of main (200) reflection of the $x=0.115$ in $\sigma \rightarrow \pi$ geometry at $T=80\text{K}$

where $s = \frac{\sin \alpha(\text{incident angle})}{\sin \beta(\text{reflected angle})}$ is the geometry factor (in our case 1 since the incident and reflected angles are equal), μ_1 - Absorption coefficient for an energy below the edge, μ_2 - for an energy above the edge and μ_F is the absorption coefficient of the strongest fluorescence line. They can be calculated using the "Absorption" program package written by Brennan and Cowan [55].

The absorption lengths calculated by this program are shown in Table 4.1 in microns (absorption of oxygen is negligible). Resulting absorption coefficients are calculated afterwards taking into account weight percentage of the materials: $\mu_F = 1695 \text{ cm}^{-1}$, $\mu_1 = 1989 \text{ cm}^{-1}$, $\mu_2 = 2611 \text{ cm}^{-1}$.

Element	$E_F=5887 \text{ eV}$	$E_1=6509 \text{ eV}$	$E_2=6604$
La	3.37	2.77	2.87
Sr	15.2	19.9	20.7
Mn	17.9	23.6	2.97

Table 4.1: Absorption lengths of La, Sr and Mn at the energy of the most intense fluorescence line (5887 eV), below the Mn-edge (6509) and above (6604) the Mn-edge

Figure 4.21 shows measured fluorescence (a) and intensity of the (1,0,0) reflection of the $x=0.125$ sample at room temperature (b), absorption coefficients calculated from

formula 4.1 (c) and corrected intensity of the (1,0,0) reflection (d).

The corrected data clearly shows two peaks at $E=6554$ eV and $E=6566$ eV. The second peak has not been observed before by other groups working on the same materials, most probably due to the poor energy resolution and insufficient intensity of the resonant reflection. However this feature has been predicted by Benfatto's full potential calculations [37] (Fig. 2.9 and connected to the complex band structure of manganites).

The resonant intensity can even be observed at room temperature, which is a non JT distorted region. The intensity of (1,0,0) (or (3,0,0)) resonant peak reaches maximum at $T \approx 220$ K ($x=0.115$), $T \approx 210$ K ($x=0.125$) and $T \approx 180$ K ($x=0.135$), and then decreases upon cooling. Below $T \approx 120$ its intensity almost stays constant for all sample. The difference is that the ration of resonant intensity in the low-temperature range to the maximum intensity in the middle-temperature range is much less for the $x=0.125$ sample than for those of the $x=0.115$ and $x=0.135$ samples. It indicates that in the low-temperature range JT distortion for commensurate $x=0.125$ are lower than distortions of incommensurate $x=0.115$ and $x=0.135$ samples.

4.4.2 Charge Ordering

In three $La_{1-x}Sr_xMnO_3$ samples with doping $x=0.115$, $x=0.125$ and $x=0.135$ superstructure reflections were found which reveal quartering of the quasi-cubic unit cell. These reflections were widely attributed to the CO phenomena in the manganites [34], [16]. All samples with $x=0.115$, $x=0.125$ and $x=0.135$ exhibit second order type transitions to the CO state at about $T=120$ K. Since the CO reflections appear at exactly the same positions for all samples, it means that only one fraction of ions with exact rational $x = 0.125$ undergoes the CO transitions while the remaining ions are randomly distributed over the sample.

4.4.3 Interplay Between Orbital Ordering and Lattice Distortions

Peak splittings along longitudinal direction of the Bragg (2,0,0) reflections were identified between 160-270K ($x=0.115$), 150-260K ($x=0.125$) and 120-230K ($x=0.135$), where the

(1,0,0) and (3,0,0) peaks are split along transverse direction. Cooperative JT distortions are believed to be responsible for the observed changing of the lattice parameters when one filled $3d_{x^2}$ -orbital is surrounded by four $3d_{y^2}$ -orbitals. The oxygen square, which surrounds one Mn atom in the a, b -zone, is distorted into a rhombus. There are two slightly different lattice parameters a and b , one is about 5.63 Å and the other one is about 5.52 Å at room temperature. The measured lattice distortion $(a - b)/(a + b)$ and the intensity of the resonant (1,0,0) reflection are shown versus temperature in Fig. 4.22. As it can be seen, the lattice distortions and the resonant signal are very much correlated.

4.4.4 Interplay between Charge and Orbital Ordering

The Yamada model says that no $3d_{(x,y,z)^2}$ -orbital ordering with quartering of the unit cell can affect the position of La atoms and mostly La-atoms are responsible for the CO signal. This explains the absence of resonant enhancement of the CO reflections in Figure 4.19.

One possible realization of $d_{(x,y,z)^2}$ -orbital ordering is shown in Figure 2.5. However, the RXS method is definitely not a direct probe of orbital ordering phenomena. Resonant signal on the forbidden (1, 0, 0) and (3, 0, 0) reflections exists in the whole temperature range below room temperature and correlated to the cooperative JT-distortions. No sharp transition to "orbital ordered phase" was observed which is a contradiction to the experiment of Endoh et al ([30]). Temperature dependence of the resonant signal slightly varies for samples with different Sr content.

At lower temperature the CO state was observed. For a series of samples with different Sr content, we have observed a phase separation with the exact $x \approx 1/8$ CO state and non-ordered areas with some excess, or lack, of charge carriers. Transition temperatures taken from magnetization measurements, RXS and non-RXS experiments are summarized in Fig. 4.23. In contrary to Tc and T_{JT} temperatures, CO transition temperatures seem to be not sensitive to the doping level x .

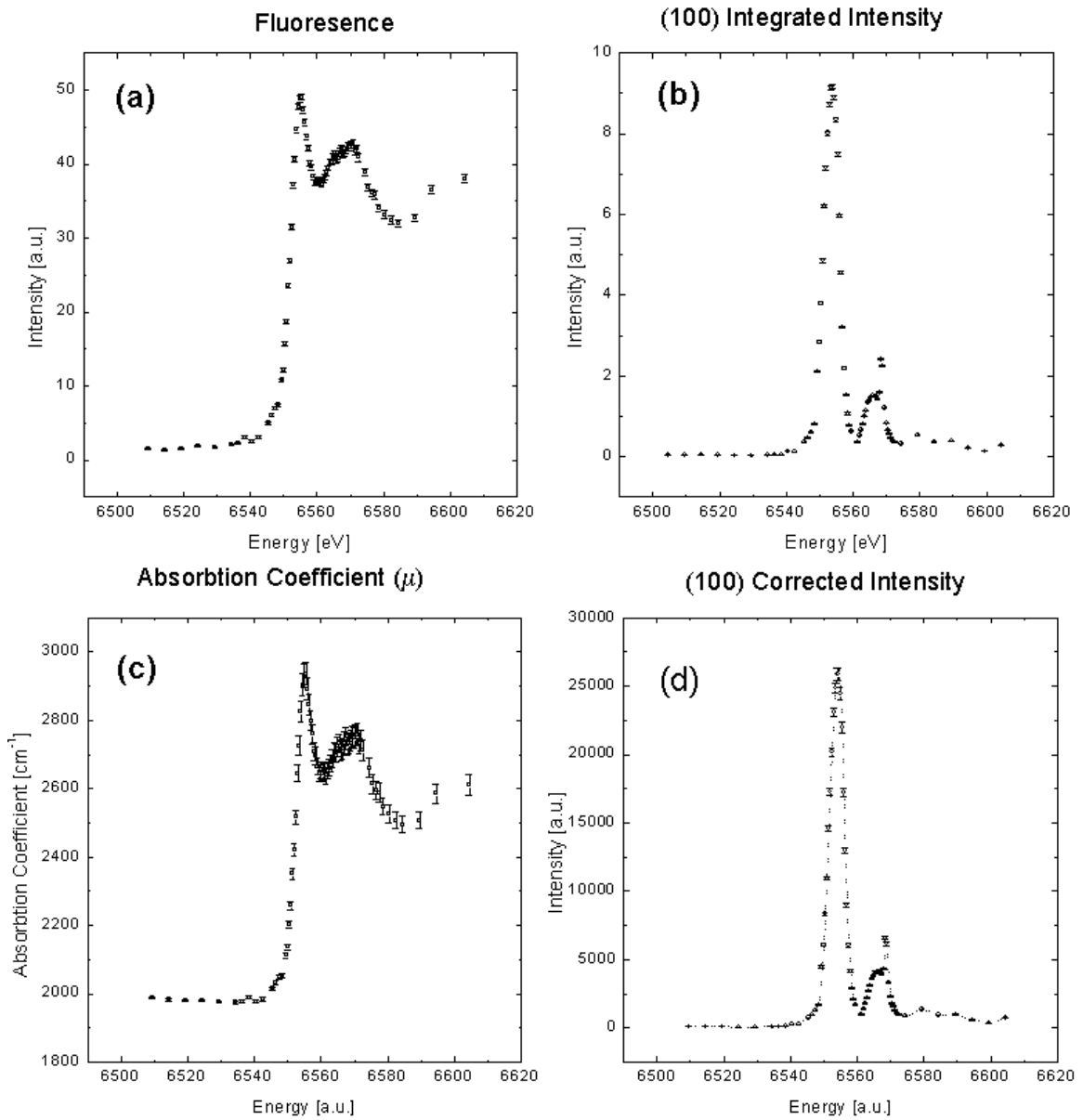


Figure 4.21: Absorption correction on the Mn K-edge of $x=0.125$ sample at room temperature. (a) - measured fluorescence, (b) - integrated intensity of the (1,0,0) reflection, (c) - calculated absorption coefficient, (d) - corrected intensity.

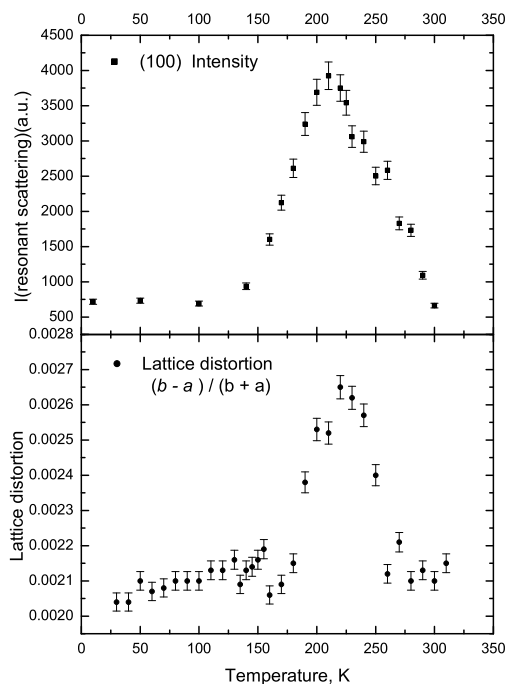


Figure 4.22: Intensity of the resonant peak and lattice distortion for the $x=0.125$ sample

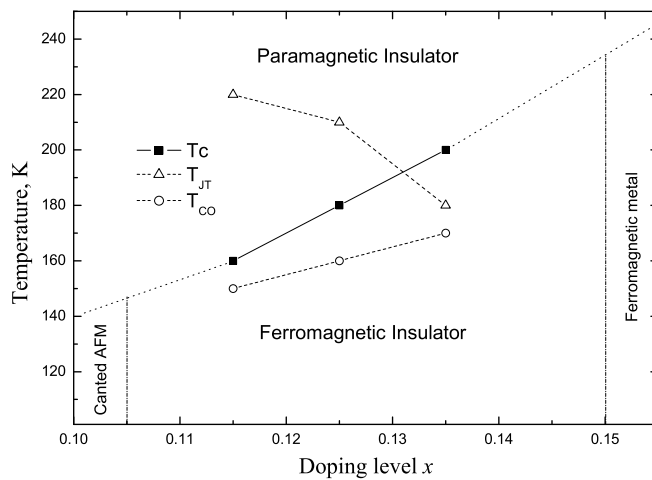


Figure 4.23: Phase diagram with temperatures taken from magnetization measurements both RXS and non-RXS experiments. Closed quadrates stand for curie temperature (T_c), open triangles for maxima of JT distortions (T_{JT}) and open circles for CO transition (T_{CO}).

Chapter 5

Experiments with Neutron Scattering

5.1 Introduction

Phenomena of neutron scattering is strongly correlated to its wave nature. The method is widely used for studying of atomic and magnetic structure of crystals due to four following reasons:

First, the wave length of thermo neutrons ($\lambda \approx 1.33 - 1.55 \text{ \AA}$) is about correlated to the lattice parameters of the crystals.

Second, neutrons do not have an electric charge. This provides a larger penetration depth (in comparison to the lattice parameters) into the bulk of the crystals.

Third, neutrons have a magnetic moment which makes them very useful in diffraction studies of the magnetic structure of the crystals. Neutrons scatter not only on the electrons in the crystals but also on the nuclei of atoms.

Fourth, The cross-section of the nuclear and magnetic scattering of neutrons is about the same order of magnitude (10^{-24} cm^2). This allows to conduct magnetic and atomic measurements with the same accuracy. In comparison to the X-rays (synchrotron radiation) scattered monochromatic neutron beam has a larger wave length dispersion and a smaller intensity but X-rays can not compete with neutrons in the field of magnetic scattering.

In common case, angle and energetic distributions of the neutrons contain information about the nuclear and magnetic structure of the crystals. We used neutron scattering only for investigation of spin ordering processes since the synchrotron radiation (X-Rays) provides experiments with higher quality on orbital, charge and lattice correlations in the manganites.

Neutron scattering may be elastic and inelastic.

5.1.1 Elastic Nuclear and Magnetic Scattering

Elastic scattering may be used for determination of magnetic structure of the crystals. If a crystal has an ordered magnetic structure than there are additional Bragg reflections from the planes with the same orientation of the magnetic moments. In case of a paramagnetic material consisting of atoms of one kind, magnetic and nuclear Bragg reflections have the same positions in the reciprocal space. But in case of a complex magnetic structure, new additional magnetic reflections may appear.

Elastic neutron scattering also may be used for determination of magnetic moments of atoms via diffuse magnetic scattering. This method is especially important in case of ordered solid state solutions like our $La_{1-x}Sr_xMnO_3$.

5.1.2 Inelastic Neutron Scattering

In case of inelastic neutron scattering the energy of scattered neutrons may be smaller than the energy of incoming neutrons due to energy loss for creation of a phonon or a magnon, or greater due to energy absorption from the crystal. Inelastic scattering may be interesting because it allows to study the dispersion of lattice excitations which take place in the process of scattering. In the energy distribution of the inelastic coherent scattering one may observe new additional peaks which are correlated to the energy gain (or loss) of one absorbed (or emitted) lattice excitation quantum (phonon or magnon).

Inelastic neutron scattering also may be used for determination of temperature dependence of spin waves using temperature dependence of diffuse scattering width.

5.1.3 Magnetic Critical Neutron Scattering

The intensity of magnetic scattering on ferro- and antiferromagnetics may sharply increase close to magnetic Bragg reflections in the vicinity of Curie (or Neele) temperatures. Using magnetic critical scattering on a crystal one can determine radii of spin moments correlations which are directly correlated to its magnetic characteristics. This may be used for determination of temperature dependences of magnetic susceptibility.

5.1.4 Paramagnetic Scattering

Critical neutron scattering take place on the "remains" of magnetic ordering above Curie (or Neele) temperature. On the other hand in paramagnetics there is another effect of pure paramagnetic scattering (even without the remains of magnetic ordering) attributed to exchange interactions between atomic spins which leads to incoherence of scattering. The theory of this scattering was developed by Van Vleck [56] and de Gennes [57].

5.2 Rules For Separation

It was shown (See [58]) that using polarized neutrons technique it is possible to separate different scattering contributions. Hence, the paramagnetic scattering is given by

$$\frac{d^2\sigma}{d\Omega d\omega_{paramagnetic}} = 2\left(\frac{d^2\sigma^{SF}}{d\Omega d\omega_x} + \frac{d^2\sigma^{SF}}{d\Omega d\omega_y} - 2\frac{d^2\sigma^{SF}}{d\Omega d\omega_z}\right) = -2\left(\frac{d^2\sigma^{NSF}}{d\Omega d\omega_x} + \frac{d^2\sigma^{NSF}}{d\Omega d\omega_y} - 2\frac{d^2\sigma^{NSF}}{d\Omega d\omega_z}\right) \quad (5.1)$$

$$\frac{d^2\sigma}{d\Omega d\omega_{coherent}} = \frac{d^2\sigma^{NSF}}{d\Omega d\omega_z} - \frac{1}{2}\frac{d^2\sigma^{NSF}}{d\Omega d\omega_{paramagnetic}} - \frac{1}{3}\frac{d^2\sigma^{NSF}}{d\Omega d\omega_{spin-incoherent}} \quad (5.2)$$

$$\frac{d^2\sigma}{d\Omega d\omega_{spin-incoherent}} = \frac{3}{2}\left(3\frac{d^2\sigma^{SF}}{d\Omega d\omega_z} - \frac{d^2\sigma^{SF}}{d\Omega d\omega_x} - \frac{d^2\sigma^{SF}}{d\Omega d\omega_y}\right) \quad (5.3)$$

Where SF (Spin-Flip) and NSF (Non-Spin-Flip) are defined like in Fig. 5.1

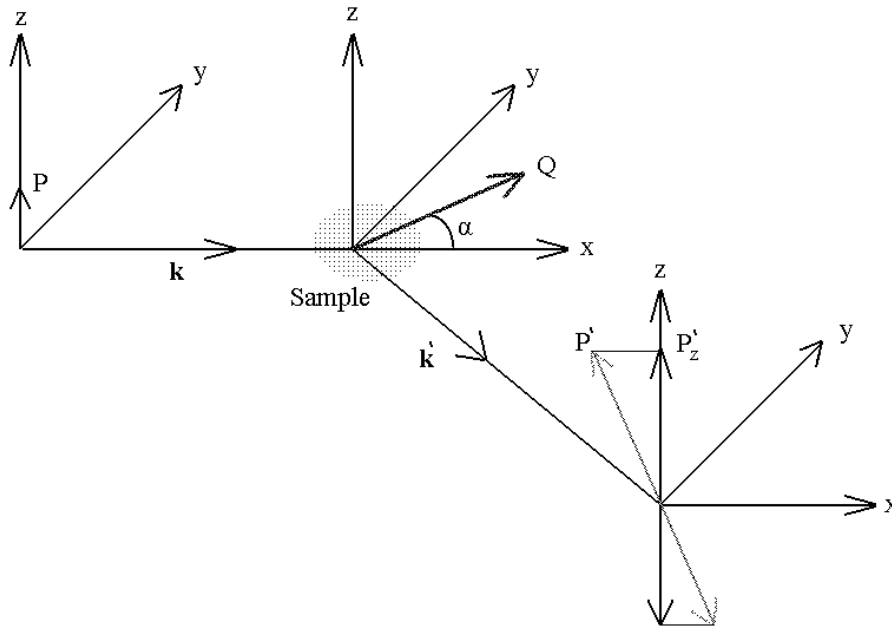


Figure 5.1: Schematic illustration of the polarized neutron experiment.

5.3 Diffuse Neutron Scattering Experiments

Diffuse neutron scattering (DNS) experiments were conducted at the DNS instrument which is specialized for such purposes and located at the research reactor DIDO (FRJ-2) in Jülich.

The DNS has a comparably compact design [58] (Fig. 5.2). Different detector banks are used for standard time-of-flight (TOF) mode and polarization analysis (typically combined with TOF). They are placed to the right and left, respectively, to the incoming beam. The polarizers and analyzers (d) are made of a stack of sputted magnetic supermirrors, alternating layers of FeCoV/Ti:N with Gd:Ti absorbing antireflexion layer underneath. The monochromatic beam is vertically and horizontally focused, the polarizers have a geometrical design to use beam focusing on the sample (c) with a substantial gain in intensity. A Mezei-type (π)-spin-flipper is used in combination with a Brookhaven correction coil (b), both made of uncoated aluminum wires. The degree of polarization determined from intensities on non-spin-flip scattering to spin-flip scattering for a coherent scatter is rather high, on average $1 - I_-/I_+ = 0.95$.

The samples were placed on the top of a cold finger of a closed-cycle cryostat. The

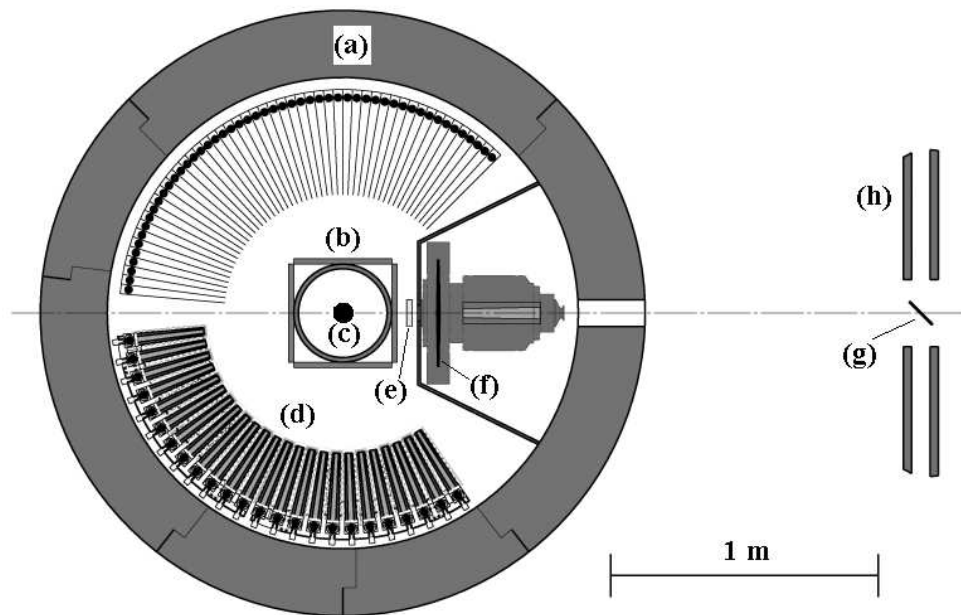


Figure 5.2: The DNS instrument at Jülich equipped for 3-dim polarization analysis. The detector bank to the right of the incoming beam is for unpolarized experiments, the one to the left for polarization analysis. A focusing layout has been used for the initial and final polarizers. (a) - shielding, (b) - coils, (c) - sample, (d) - polarization analyzer, (e) - flipper, (f) - disc chopper, (g) - monochromator Graphite (002), (h) - neutron guide.

cold finger was shielded with Cadmium foils to reduce the background scattering. Temperatures between 15K and 300K could be reached.

We studied the same 3 single crystals with $x=0.105$, $x=0.115$ and $x=0.125$ which we used in the RXS and non-RXS experiments. As that moment samples with $x=0.105$ and $x=0.115$ had worse quality in comparison to the time of the RXS experiments. The crystals seemed to be hygroscopic and absorbed water from the air which lead to their decomposition. However, qualitative experiments on the diffuse scattering were still possible on these crystals. On the other hand, signal from domains with different orientation in the bulk of the crystal, as well as from the decomposed powder, made experiments on detection of the CO phenomena nearly impossible.

With the banana-type multidetector complete layers of reciprocal space were recorded with a wavelength of 3.3 \AA at different temperatures. Figure 5.3, represents the (ac) plane of the $x=0.125$ sample at $T=250\text{K}$. Additional data taken at different temperatures for samples with $x=0.105$, 0.115 and 0.125 are available in Appendix B. The data reveals a significant amount of diffuse scattering around Bragg reflections both above and below T_c .

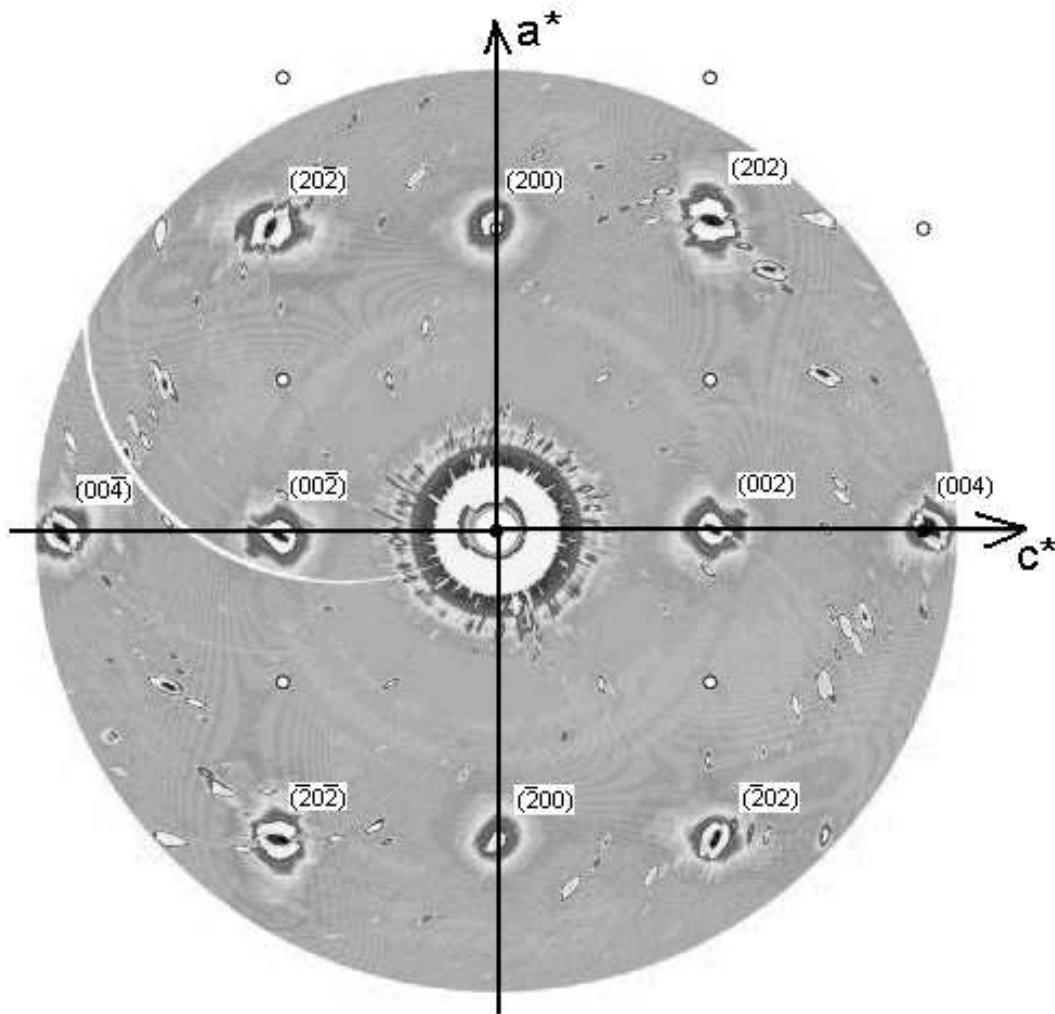


Figure 5.3: A 2D contour plot of the (ac) reciprocal plane of the $x=0.125$ single crystal at $T=250$.

For qualitative determination of the temperature dependence of the diffuse scattering it is possible to measure the scattering intensity at one fixed point in the reciprocal plane

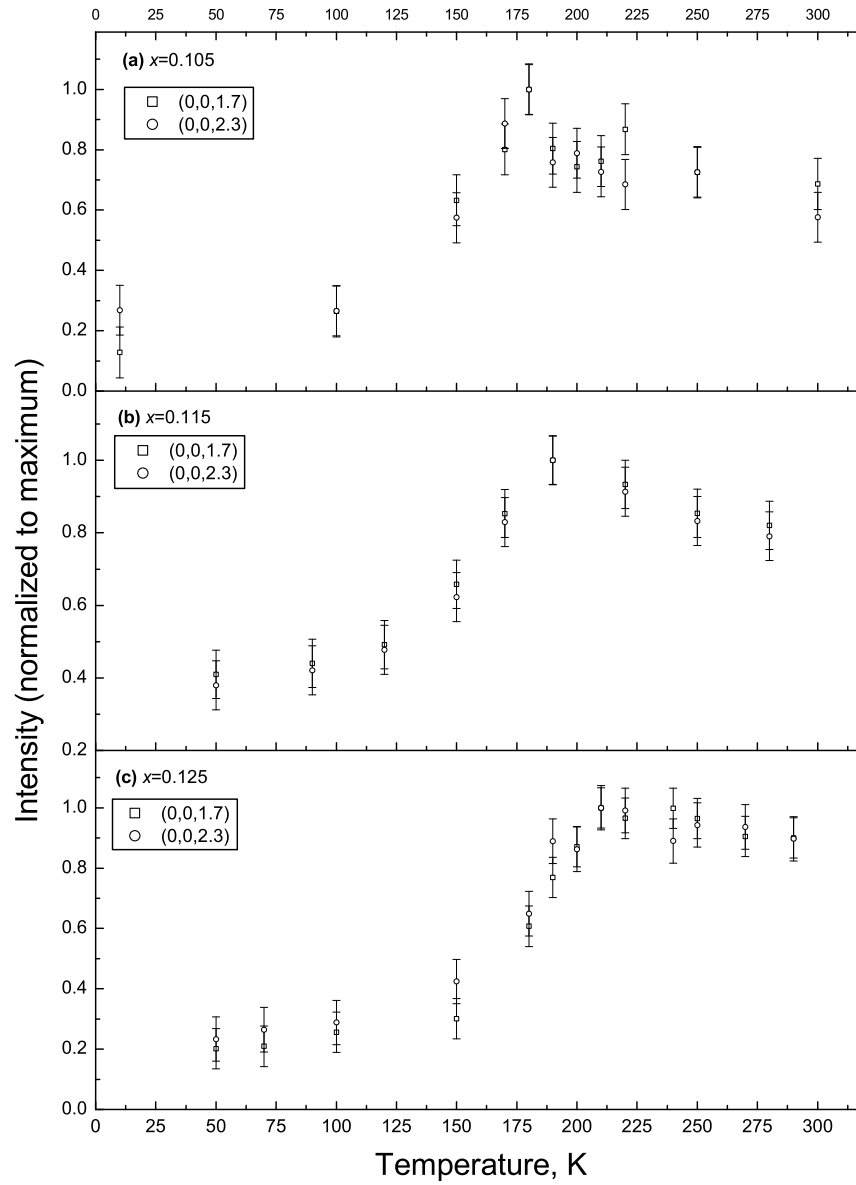


Figure 5.4: Temperature dependence of the diffuse scattering intensity for crystals with (a) $x=0.105$, (b) $x=0.115$ and (c) $x=0.125$

off the Bragg peak. For example at $(0,0,1.7)$ and $(0,0,2.3)$. Temperature dependences of the diffuse scattering from single crystals with $x=0.105$, 0.115 and 0.125 are shown in Fig. 5.4 (a),(b) and (c) respectively. The diffuse scattering intensity for all samples reaches maximum at T_c and then decreases upon cooling. The transition temperatures are consistent with those measured in magnetization measurement. It means that by this method transition temperatures can be measured without applying external magnetic field in contrary to the SQUID method.

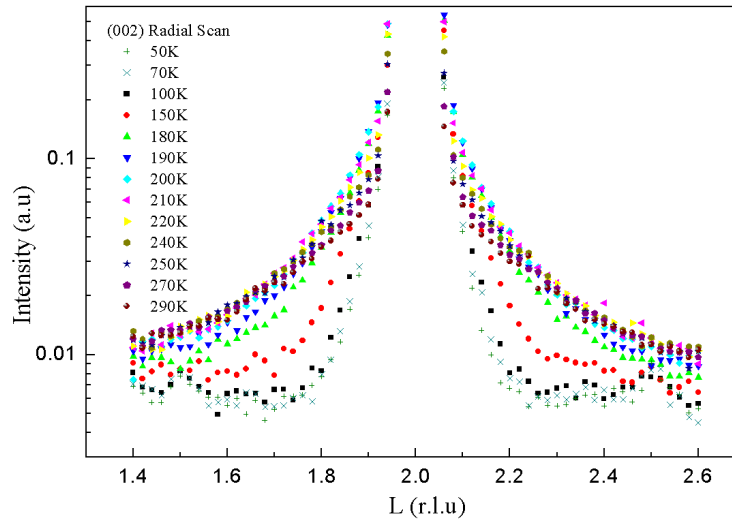


Figure 5.5: Radial scans across (002) Bragg reflection of the $x=0.125$ crystal measured with just one single detector at various temperatures.

To analyze the temperature dependence of the diffuse scattering we performed transverse and longitudinal scans along (002) Bragg reflections with fine step of 0.02 r.l.u. (reciprocal lattice units). Figure 5.5 represents compilation of the results of these scans for the $x=0.125$ single crystal. At temperatures above 200 K the data can be well fitted with a sum of the Gauss function (contribution from the nuclear Bragg with the width of about 0.4 r.l.u.) and the Lorentz functions (contribution from the diffuse scattering). Below 200 K, when the width of the Lorentz-shaped diffuse scattering intensity is comparable to the width of the Bragg peak, the data may be treated as a sum of the Gauss and the Voigt functions. The Voigt function is a convolution of the Lorentz and the same

Gauss function ¹. A fit at T=200 K is shown in Fig. 5.6.

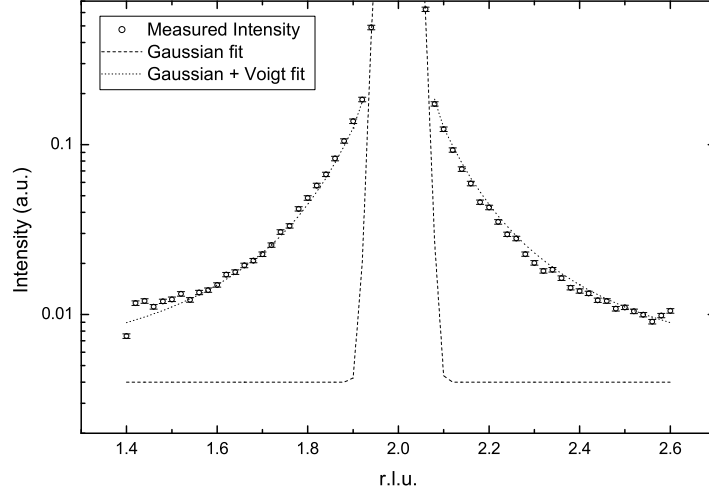


Figure 5.6: Radial scan across (002) Bragg reflection of the $x=0.125$ crystal at T=200K. Dotted line - fit with sum of Gauss and Voigt functions.

The measured temperature dependence of the diffuse scattering intensity as well as the width of the Lorentz (Voigt) function are shown in Fig. 5.9. The intensity has a maximum around 175 K and then decreases at low temperatures, on the other hand, the width of the Lorentz-shaped fit has a minimum at the same temperature and then increases upon cooling. In Fig. 5.7 logarithm of the width is plotted as a function of $\log \frac{T-175}{T}$ showing a linear dependence and directly giving the value of the critical exponent of about 0.70.

It is possible to fit the diffuse scattering intensity with a mean-field formula. In the quasi-elastic approximation, $I_{diff} \sim \chi(Q) \cdot T$, with

$$\chi = g^2 \mu_B^2 S(S+1) / [3k_B T - 2S(S+1)J(Q)] \quad (5.4)$$

where g is the spectroscopic splitting factor, μ_B - Bohr's magneton, S - total spin, equals to 1.925 ([60]), k_B - Boltzmann's coefficient, $J(Q)$ - Fourier transform of the exchange

¹The Voigt function formula:

$$f(x) = \frac{\int_{-\infty}^{\infty} \frac{H \exp(-y^2) dy}{w_l^2 + [(\frac{x-x_0}{w_g}) - y]^2}}{\int_{-\infty}^{\infty} \frac{\exp(-y^2) dy}{w_l^2 + y^2}}$$

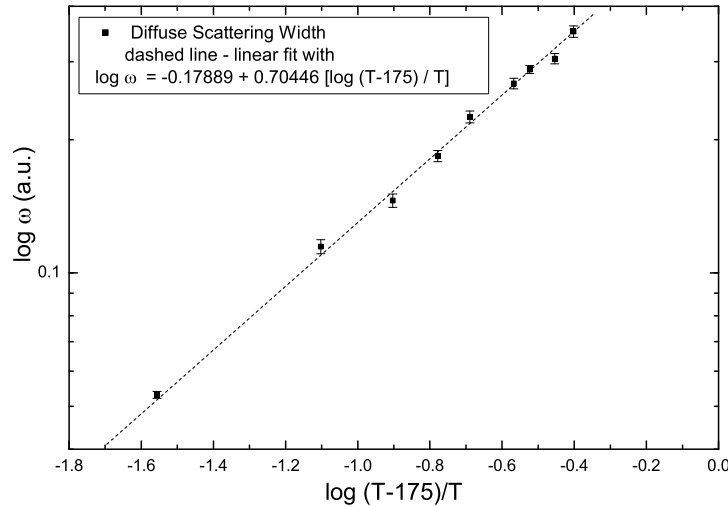


Figure 5.7: Logarithm of the diffuse scattering width plotted as a function of $\log \frac{T-175}{T}$.

integral J to the nearest neighbors [59]. The results are plotted in Fig. 5.8. One can fit the data using only two parameters, a common scale factor A and $J(Q)$. The $J(Q)$ value obtained from this field is equal to approximately 40 K.

5.4 Polarized Neutrons Experiments

By applying polarized neutron technique we were able to separate different scattering contributions. Fig.5.10 shows the polarization degrees of neutron beam polarized in different direction (P_x , P_y and P_z) as a function of temperature. At temperatures above T_c , polarization degree for the P_y and P_z components is about 95 % and for the P_x component is 90 %. Below T_c the polarization degree begin to decrease due to depolarization of neutrons due to transition to the ferromagnetic state (See Fig.5.10). Below 160 K neutrons with all polarization components are completely depolarized.

Using formulas 5.1, 5.1 and 5.1 it is possible to separate paramagnetic and spin-incoherent scattering at temperatures above T_c . Fig. 5.11 shows radial scan across the (0,1,3) pure nuclear Bragg reflection at 220 K. Gaussian-shaped nuclear coherent scattering and Lorentzian-shaped paramagnetic and spin-incoherent scattering are clearly separated. Note, that the right and the left shoulders of the Lorentz curve are not sym-

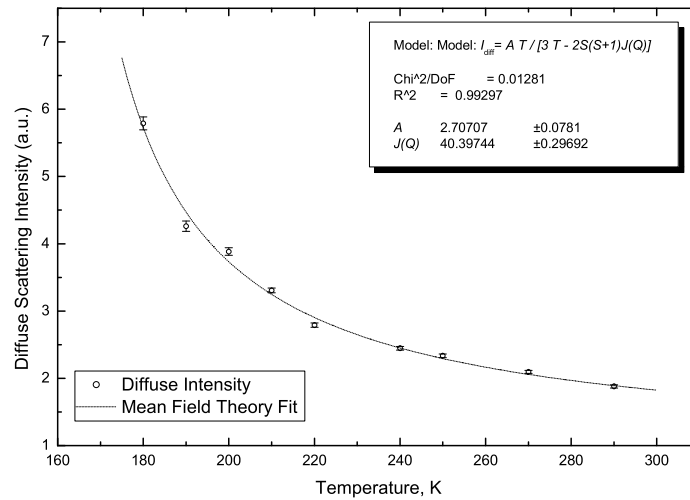


Figure 5.8: The diffuse scattering intensity as a function of temperature and a mean field theory fit (dotted line).

metric due to the fact that at the corresponding q -values there is a weak signal from the aluminum shielding of the cryostat. As it can be seen the diffuse scattering is dominated by paramagnetic scattering.

5.5 Results

Significant amount of diffuse scattering has been observed at different temperatures around main Bragg peaks for the samples with $x=0.105$, 0.115 and 0.125 . The temperature dependence of the diffuse scattering may be well fitted by the mean field theory with a value of exchange integral of about 40 K. Using polarization set-up different components of the diffuse scattering can be separated above T_c . The results show that the most of the diffuse scattering originates from the paramagnetic scattering. Below the T_c the neutrons are depolarized due to the transition to ferromagnetic state.

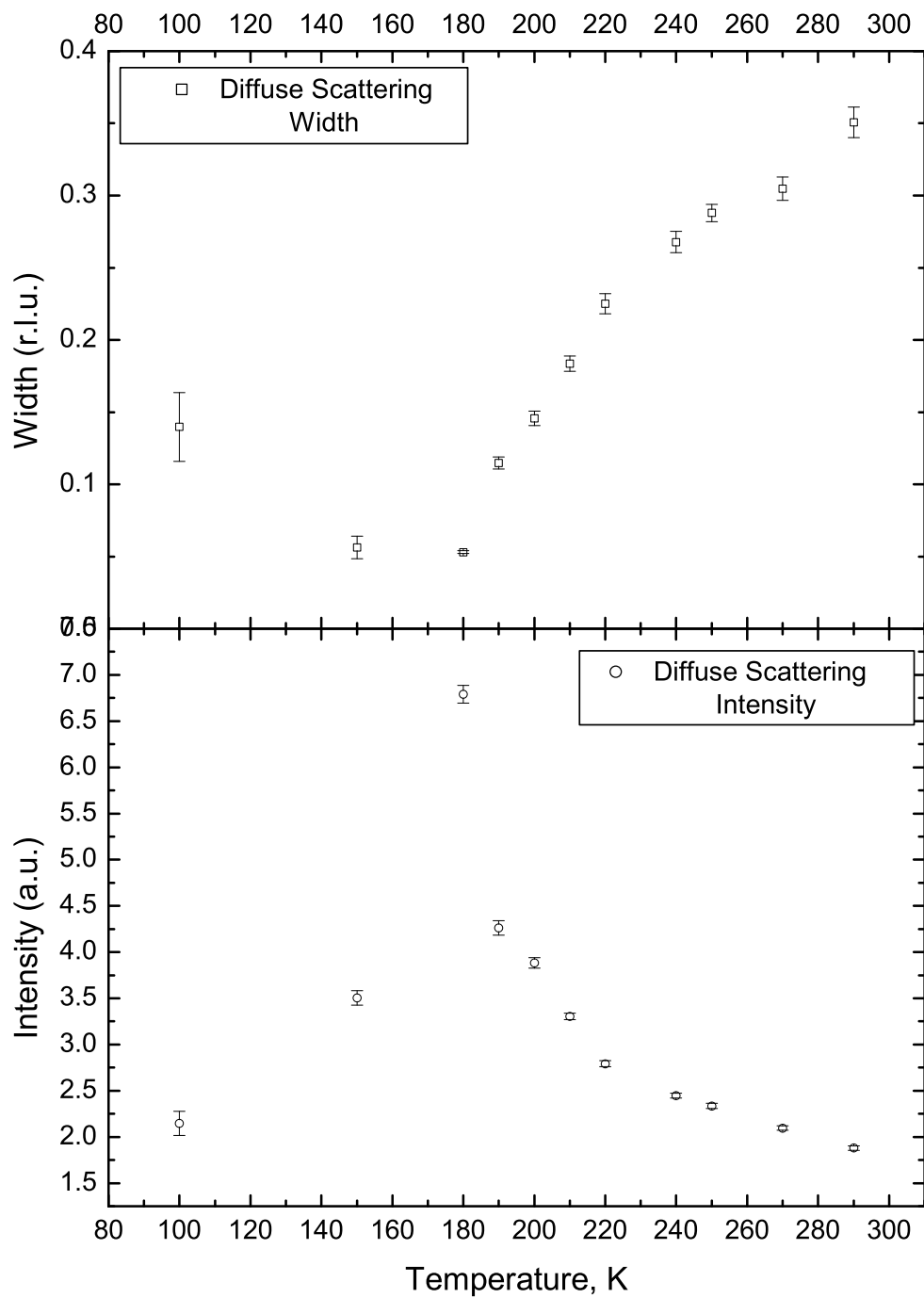


Figure 5.9: Temperature behavior of the intensity and the width of diffuse scattering

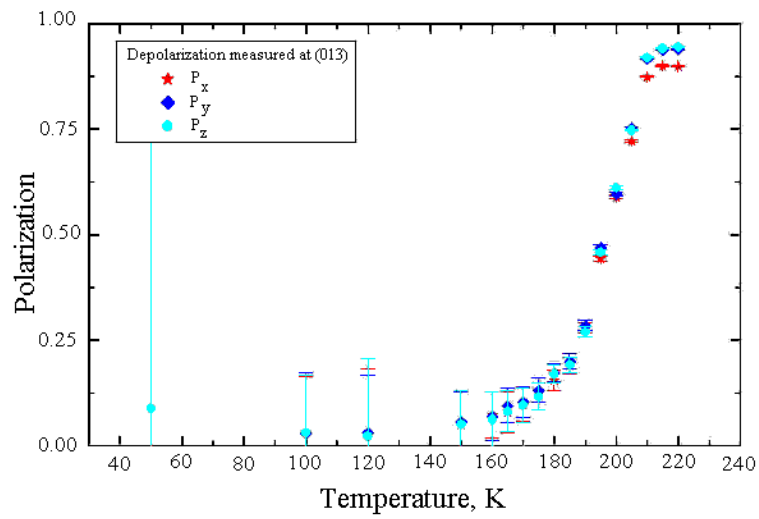


Figure 5.10: Polarization degree measured at pure nuclear (0,1,3) Bragg reflection as a function of temperature for the $x=0.125$ single crystal.

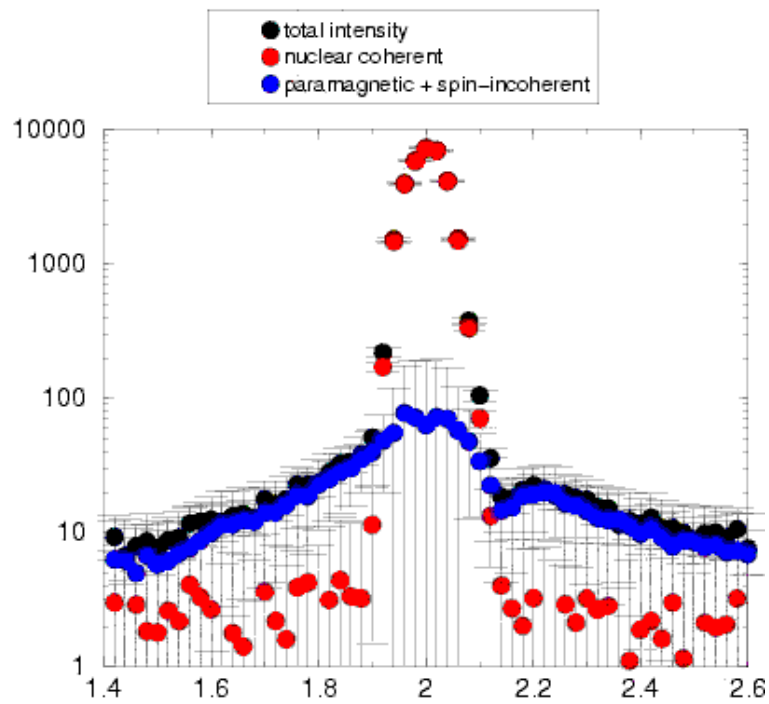


Figure 5.11: Separation of paramagnetic and nuclear coherent scattering at (0,1,3) nuclear reflection at $T=220$ K for the $x=0.125$ single crystal.

Chapter 6

Summary of Results

The main results obtained in the present work are as follows:

- A new technique for preparation of single-phase manganite powders has been developed and approved for a series of powder samples with different stoichiometry.
- A series of $La_{1-x}Sr_xMnO_3$ good quality single crystals with Sr content $x=0.105$, 0.115 , 0.125 and 0.135 has been obtained using the floating-zone single crystal growing method. Tuning x doping level around fractional $1/8$ value allowed to study systematically properties of the manganites including interplay between charge, spin and orbital ordering.
- The powder samples and the grown single crystals have been thoroughly studied and characterized at the Institute of Solid State Research (IFF) by macroscopic measurements (XPD, ICAP, EIS), magnetization measurements (SQUID) and resistivity measurements.
- To clarify contradictory results of the experimental works reported so far by other groups ([30], [16], [34], [38], [39] and other), a complimentary approach including experiments with both resonant and non-resonant X-Ray scattering as well as neutron scattering has been implemented.

Results from the experiments firmly show that the resonant X-Ray scattering method can not be treated as direct probe of orbital ordering phenomena. Resonant intensities on the forbidden $(1, 0, 0)$ and $(3, 0, 0)$ reflections exist in the whole temperature

range below room temperature in the series of samples with different Sr content and are correlated mainly to the cooperative JT-distortions. No sharp transition to "orbital ordered phase" was observed.

At energies close to Mn K-Edge a multi-peak energy response of the forbidden $(1, 0, 0)$ and $(3, 0, 0)$ reflections has been observed. At least two separate maxima are found at 6554 eV and 6566 eV. This effect is attributed to dipolar $1s \rightarrow 4p$ transition with a complex $4p$ band.

By applying advantages of the very good energy resolution of the 6ID-B station at the APS, the *Umweganregung* effect has been also observed for these materials.

- Non-resonant X-Ray experimental data reveals a charge ordered phase with quartering of the quasi-cubic unit cell for the same series of samples. Previously existed charge ordering models are confirmed. Nevertheless, the transition temperature to the ordered state found to be of second order type and equals to about 120 K for all samples which is in disagreement with experiments conducted by other groups working on the same systems.

It is also suggested that there is a phase separation for samples with non-rational compositions $x=0.115$ and $x=0.135$ into domains with exact rational $x=0.125$ value and domains with a lack (or extense) of charge carriers.

- Results of the neutrons scattering experiments show a large amount of diffuse scattering around main Bragg peaks. Using polarization analysis it is shown that the diffuse scattering can be effectively separated to nuclear coherent and paramagnetic scattering, the latter is dominating above the Curie temperature.

The diffuse scattering can be well fitted with the main field theory, giving the value of exchange integral of about 40 K, which is higher than the values reported in the literature.

Appendix A

RXS Mesh-Scans

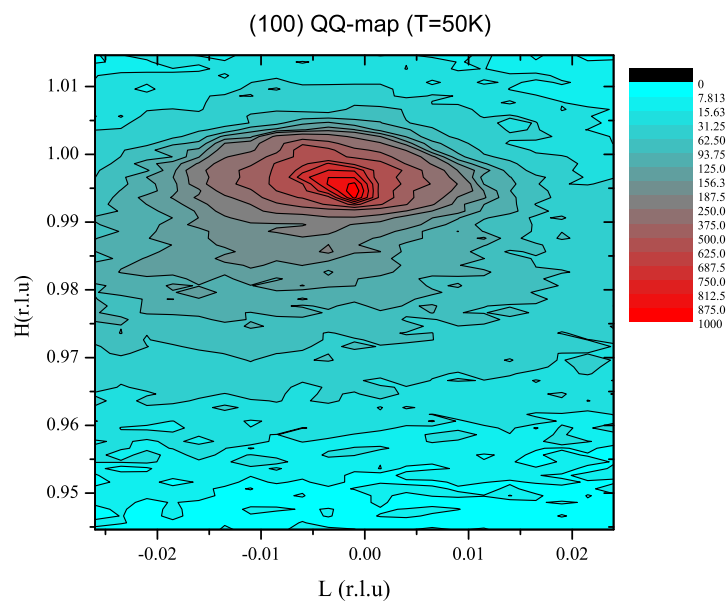


Figure A.1: Reciprocal area around (1,0,0) resonant reflection for the $x=0.125$ sample at $T=50$ K

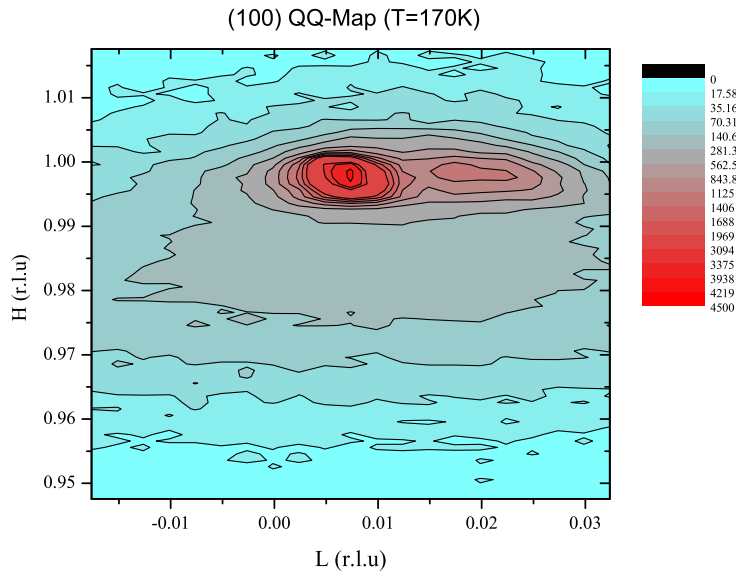


Figure A.2: Reciprocal area around (1,0,0) resonant peak for the $x=0.125$ sample at $T=170$ K

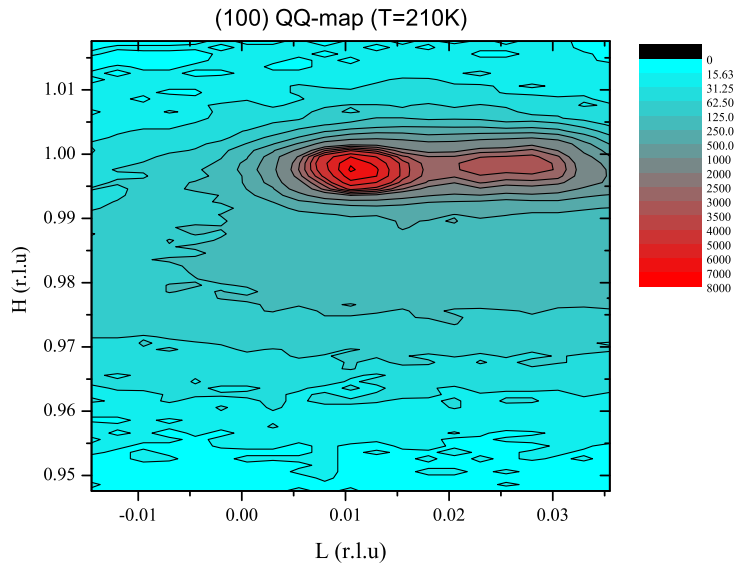


Figure A.3: Reciprocal area around (1,0,0) resonant peak for the $x=0.125$ sample at $T=210$ K. Splitting due to JT-distortion can easily be seen.

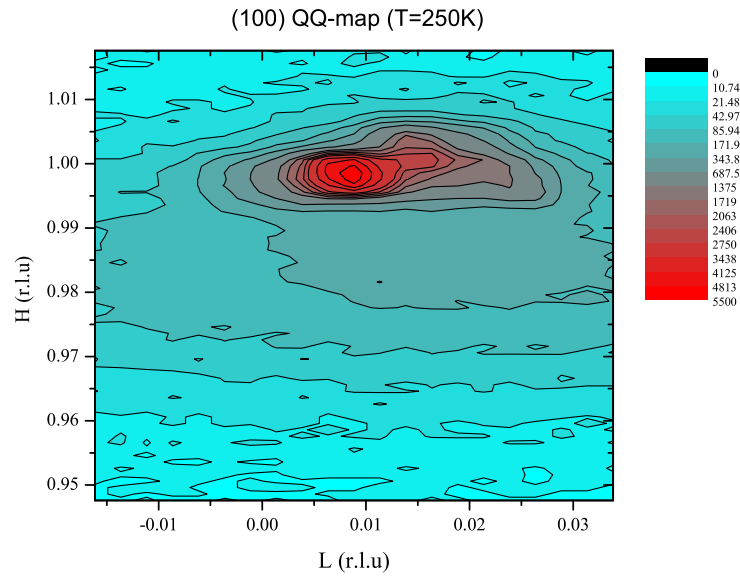


Figure A.4: Reciprocal area around (1,0,0) resonant peak for the $x=0.125$ sample at $T=250$ K

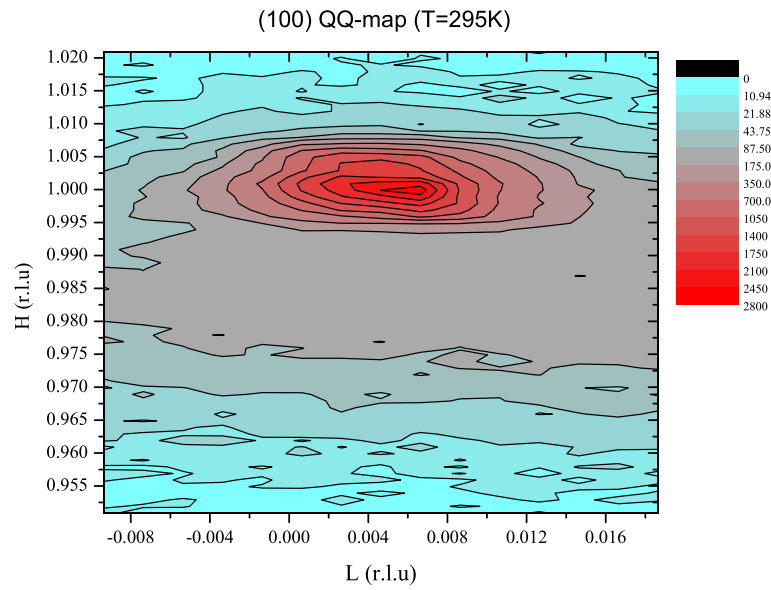


Figure A.5: Reciprocal area around (1,0,0) resonant peak for the $x=0.125$ sample at $T=295$ K

Appendix B

Neutron Scattering Data

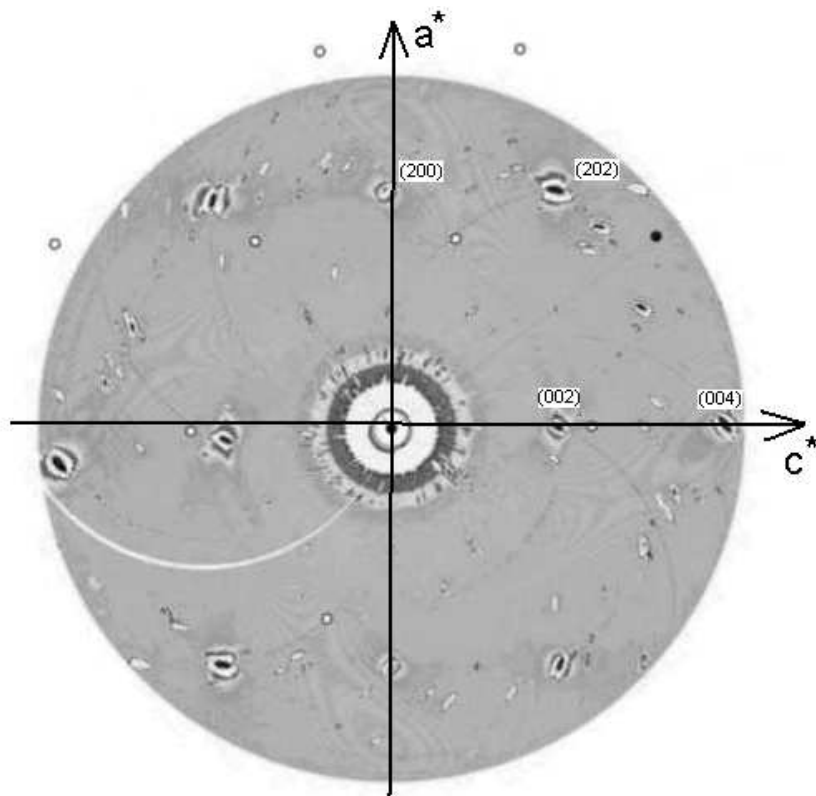


Figure B.1: A 2D contour plot of the (ac) reciprocal plane of the $x=0.125$ single crystal at $T=100\text{K}$.

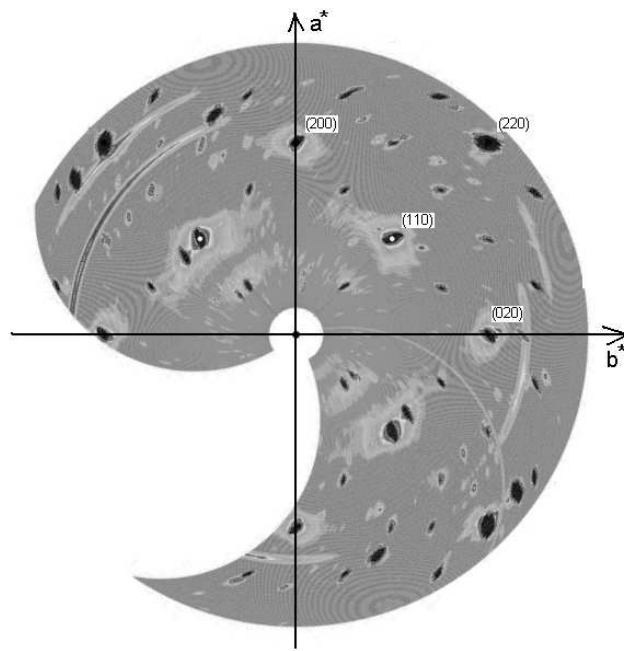


Figure B.2: A 2D contour plot of the (ab) reciprocal plane of the $x=0.105$ single crystal at $T=100\text{K}$.

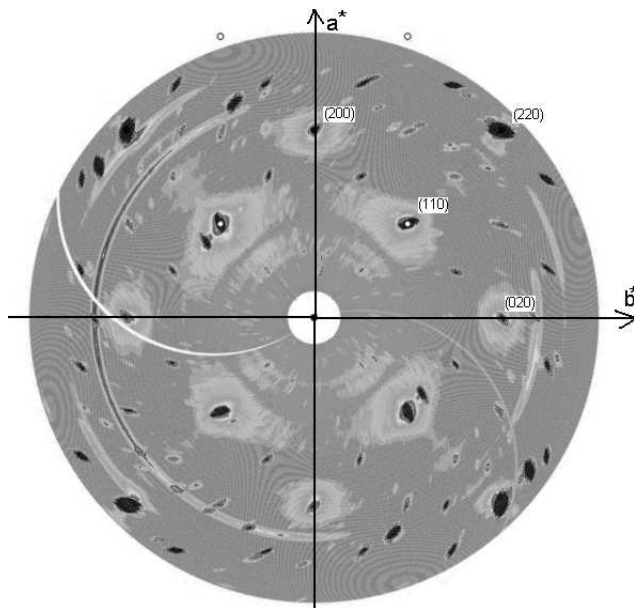


Figure B.3: A 2D contour plot of the (ab) reciprocal plane of the $x=0.105$ single crystal at $T=250\text{K}$.

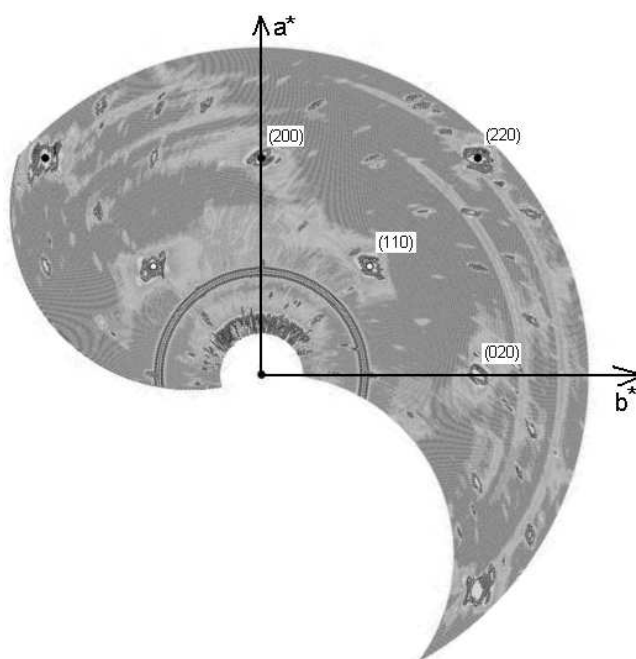


Figure B.4: A 2D contour plot of the () reciprocal plane of the $x=0.115$ single crystal at $T=50\text{K}$.

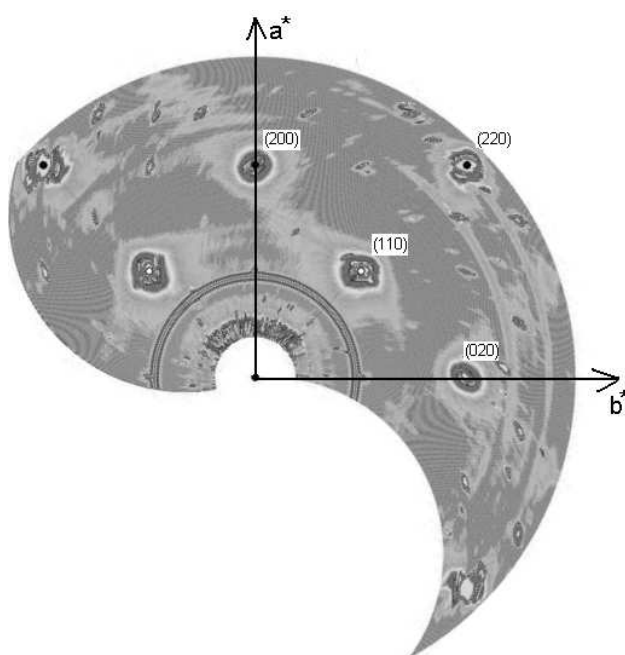


Figure B.5: A 2D contour plot of the () reciprocal plane of the $x=0.115$ single crystal at $T=250\text{K}$.

List of Figures

1.1	The idealized perovskite unit-cell of manganese and Jahn-Teller distortions.	5
1.2	Splitting of the $3d$ -orbitals under the influence of Crystal Field and Jahn-Teller distortions.	6
1.3	Super exchange of two $4d$ -ions over an O^{2-} -ion.	7
1.4	Double Exchange Mechanism.	9
1.5	Complete phase diagram of $La_{1-x}Sr_xMnO_3$. From [8]. Abbreviations used in this figure: O, O', O'' - Different Orthorhombic phases, R - Rhombohedral, C - Cubic, H - Hexagonal, I - Insulator, M - Metal, PM - Paramagnetic, FM - Ferromagnetic, AFM - Antiferromag- netic, CA - Canted	11
1.6	Temperature dependence of resistivity for $La_{1-x}Sr_xMnO_3$ under various magnetic fields. (a) $x=0.15$, (b) $x=0.175$, (c) $x=0.2$. Open circles represent the magnitude of negative Mag- netoresistance $-\frac{[\rho(H) - \rho(0)]}{\rho(0)}$ with a magnetic field of 15 T. Open triangles represent structural transitions. From [7].	12
1.7	Temperature dependence of the resistivity in zero field for $La_{1-x}Sr_xMnO_3$. Arrows in- dicate the critical temperature for the ferromagnetic transition. Open triangles represent structural transitions. From [7]	13
1.8	Magnetic phases in $La_{1-x}Ca_xMnO_3$ [15]. The shaded lines represent the insulator-metal transitions. The regions are indicated with the same abbreviations like in Fig.1.5, only A stands here for antiferromagnetic.	14
1.9	Spin, Charge and Orbital Ordering model of the CE type observed for most of $x \approx 1/2$ manganites. The e_g -orbitals ordering on Mn^{3+} sites are also shown. The Mn^{4+} sites are indicated by closed circles. From [18].	15
2.1	Phase diagram for $La_{1-x}Sr_xMnO_3$, $0 \leq x \leq 0.20$. [28] The regions are indicated with the same abbreviations like Fig.1.5	18

- 2.2 Schematic representation of the observed diffraction pattern. The solid lines represent the pseudocubic $(h, k, 0)_c$ reciprocal space. The dashed line give the orthorhombic $(h, k, 0)_o$ lattice. The small solid circles give the the positions of the superstructure satellites. The inset shows the corresponding positions of the Bragg reflections in the first Brillouin zone of pseudocubic reciprocal space. Notice Δ and Δ' points are equivalent when referred to the exact orthorhombic symmetry. The equivalent superlattice reflections originating from the different domains are distinguished by the following symbols: open diamond M points of domain I; stripped diamond X points of domain II; dotted diamond X points of domain III. [16] 19
- 2.3 Temperature dependencies of the intensities of various types of reflection: (a) $x = 0.15$, (b) $x = 0.10$. [16] 20
- 2.4 According to the Yamada CO model there are periodical two layers with charge carriers (full circles, Mn^{4+}) and two JT-distorted layers without charge carriers. This ordering exists for optimal $x=0.125$ doping level. 20
- 2.5 One possible ordering of $d_{(x,y,z)^2}$ -orbitals according to the Yamada model for exact $x=0.125$ doping. Holes are not shown since they are not ordered as opposed to the orbitals. The circle symbols are d -orbitals perpendicular to the figure plane. 21
- 2.6 (a) Proposed hole configuration corresponding to the most stable state. The unit cell of the hole lattice is $(\sqrt{2} \times \sqrt{2} \times 2)_{\text{cubic}}$. (b) Schematic representation of the elongated orbitals and the deformation of the oxygen octahedron at various types of small polarons. A, B (solid lines): orbital and deformation around the Mn^{3+} site, A', B' (dashed lines): orbital and deformation around the $Mn^{3.25+}$ site. [33] 22
- 2.7 (a) The surveyed area in the reciprocal space. The solid lines belong to the cubic reciprocal lattice, whereas the dashed lines show the h, k plane of an orthorhombic setting. The corners represent the fundamental reflections. Charge peaks and superstructure reflections due to Sr-doping have been observed at the indicated positions. (b) Comparison of the charge peak intensities in the $x=0.125$ and the $x=0.15$ sample. The intensities are normalized relative to the adjacent Bragg-reflections. The inset shows resistivity measurement from the same samples on a logarithmic scale. [34] 23
- 2.8 Upper panel: Schematic view of the orbital and spin ordering in the $a - b$ plane of the perovskite manganite, $LaMnO_3$. Lower panel: Schematic energy level diagram of Mn $4p_{x,y,z}$ in the orbitally ordered state. From [35] 24
- 2.9 (a) Anomalous resonant diffraction intensity (adimensional units) at the $(3,0,0)$ reflections by full potential calculations. (a) Full line: Pure JTD; (b) long-dashed line: JTD plus OO on all Mn atoms; (c) dotted line: same as (b) with no OO on central Mn_1 atom; (d) dot-dashed line: pure OO without JTD ($\times 10$). (b) Mn K-edge unpolarized absorbtion cross section (Mbarn, left scale) in $LaMnO_3$ and anomalous resonant diffraction signal due solely to JTD, calculated in muffin-tin approximation (adimensional units, right scale). [37]. 25

2.10	Temperature dependence of the normalized intensity of the orbital ordering reflection (3,0,0) at E=6555 eV. Open symbols correspond to results obtained at an azimuthal angle $\psi = 127^\circ$ and cooling with a displex cryostat; closed symbols were obtained for $\psi = 90^\circ$ and heating with an oven. [35]	26
2.11	(a) Energy dependence of intensity of the orbital ordering reflection (0,3,0) at $T = 12$ K. The dashed curve represents fluorescence showing the resonant energy (6552 eV) corresponding to the <i>MnK</i> -edge. (b) The azimuthal angle dependence of (0,3,0). The solid line is the twofold squared sine curve of angular dependence. (c) Temperature dependence of (0,3,0) peak intensity [30].	27
2.12	Comparison of temperature dependencies for $\sigma\sigma$ – and $\pi\pi$ -component of (003) reflection shown in a) and the lattice parameters (Pbnm-setting) in b). The energy dependence for $\sigma\sigma$ – and $\pi\pi$ -component at 200K is plotted in c) and d), respectively.	28
3.1	Distribution of the particle size after milling as determined by the ultrasonic probe analysis.	32
3.2	Typical XPD pattern for $La_{0.875}Sr_{0.125}MnO_3$ sample.	33
3.3	Compilation of measured Curie temperatures in nominal $La_{1-x}Sr_xMnO_3$ compounds from [15].	35
3.4	CSI machine with four ellipsoidal mirrors (a). Common view (b).	36
3.5	Schematic illustration of the four mirror image furnace. Upper view.	36
3.6	Schematic illustration of 3 stages of growing process. Front view.	37
3.7	Grown crystal on top of seed rod.	38
3.8	Laue picture taken from $La_{0.875}Sr_{0.125}MnO_3$ crystal. The polished surface is (1 0 0) plane of the crystal, the distance between the X-Ray source and the sample is 3 cm.	39
3.9	Areas on the crystal surface investigated by electron ion spectroscopy. $La_{0.875}Sr_{0.125}MnO_3$ sample	40
3.10	Magnetization of the four $La_{1-x}Sr_xMnO_3$ single crystals.	42
3.11	Reciprocal magnetization of the four $La_{1-x}Sr_xMnO_3$ single crystals. Transition temperatures are indicated with Tc symbols, transition temperatures as are taken from Fig. 2.1 are indicated with Tc(lit.).	43
3.12	Resistance of four $La_{1-x}Sr_xMnO_3$ single crystals with different x contents in zero field. Transition temperatures are shown as from magnetization measurements Fig. 3.11.	44
4.1	The schematic view of the experimental arrangement (refs. [50], [51]) which consists of a sample crystal (S), analyzer crystal (A) and photon detector (D). φ is the azimuthal angle and φ_A is the analyzer angle. \vec{k}' (k'^y) is the photon momentum and $\vec{\pi}'$ (π'') and $\vec{\sigma}'$ (σ'') are the polarization of the incident (scattered) photon.	46
4.2	Rocking curve on the (200) reflection of the $x = 0.125$ sample at room temperature. Gaussian fit is also shown.	46

4.3	Fluorescence at the Mn K -edge. $T=300$ K, $x=0.125$ sample. Tabulated energy for Mn K -Edge (single ion) is 6539 eV (inflection point).	47
4.4	Resonant enhancement of the forbidden (1,0,0) at the Mn K -edge. ($x=0.125$ sample) at different temperatures normalized at the maximum. (1) Main peak, (2) Second peak and (3) Multiple scattering peak.	48
4.5	Rocking curve scan of the resonant (100) reflection in $\sigma - \pi$ and $\sigma - \sigma$ polarization geometries. Note the logarithmic scale of the intensities.	49
4.6	Temperature behavior of magnetization (a), resistivity (b), intensity of (1,0,0) reflection (c). $x=0.115$ sample, $\Psi = -90^\circ$. Curie temperature is indicated with vertical line as defined in Figure 3.10 and literature [7].	50
4.7	Temperature behavior of magnetization (a), resistivity (b), intensity of (1,0,0) reflection (c). $x=0.125$ sample $\Psi = -90^\circ$. Curie temperature is indicated with vertical line as defined in Figure 3.10 and literature. [7].	51
4.8	Temperature behavior of magnetization (a), resistivity (b), intensity of (1,0,0) reflection (c). $x=0.135$ sample $\Psi = -90^\circ$. Curie temperatures is indicated with vertical line as defined in Figure 3.10 and literature. [7].	52
4.9	Azimuthal dependence of the intensity of (3,0,0) reflection normalized by the intensity of the (2,0,0) Bragg reflection. $x=0.135$, $T=220$ K, $E=6554$ eV. The angle Ψ is zero when the crystal c axis is normal to the scattering plane and ± 90 deg when in the scattering plane.	53
4.10	Experimental set-up of the high energy experiment. (a) - sample, (b) - direct beam stopper, (c) - large-area detector.	54
4.11	High-energy pattern of the $(h, k, 0)$ plane of the $x=0.125$ crystal. $E=88$ keV, $T=300$ K	55
4.12	L-scan of the $x = 0.115$ crystal, $T=50$ K, $E=9500$ eV	57
4.13	The surveyed area in reciprocal space (ac -plane) with different types of reflections observed.	57
4.14	The surveyed area in reciprocal space (ab -plane) with different types of reflections observed.	58
4.15	Temperature behavior of the integrated intensity (a) and the peak width of the (4.25,0.25,0) reflection of the $x=0.115$ sample (b) taken from transverse scans.	59
4.16	Temperature behavior of the integrated intensity (a) and the peak width of (3.75,0.25,0) reflection of the $x=0.125$ sample (b) taken from transverse scans.	60
4.17	Temperature behavior of the integrated intensity (a) and the peak width of (3.75,0.25,0) reflection of the $x=0.135$ sample (b) taken from transverse scans.	61
4.18	Temperature behavior of the intensity and the peak width of (4.5,0.5,0) and (2,0,0) reflections in $\sigma \rightarrow \pi$ geometry for $x=0.115$ sample.	62
4.19	Energy dependence of (4.5,0.5,0) and (4.25,0.25,0) peaks in $\sigma \rightarrow \pi$ geometry for $x=0.115$ sample at $T=80$ K	63
4.20	Energy dependence of main (200) reflection of the $x=0.115$ in $\sigma \rightarrow \pi$ geometry at $T=80$ K	64

4.21	Absorption correction on the Mn K-edge of $x=0.125$ sample at room temperature. (a) - measured fluorescence, (b) - integrated intensity of the (1,0,0) reflection, (c) - calculated absorption coefficient, (d) - corrected intensity.	67
4.22	Intensity of the resonant peak and lattice distortion for the $x=0.125$ sample	68
4.23	Phase diagram with temperatures taken from magnetization measurements both RXS and non-RXS experiments. Closed quadrates stand for curie temperature (T_c), open triangles for maxima of JT distortions (T_{JT}) and open circles for CO transition (T_{CO}).	68
5.1	Schematic illustration of the polarized neutron experiment.	72
5.2	The DNS instrument at Jülich equipped for 3-dim polarization analysis. The detector bank to the right of the incoming beam is for unpolarized experiments, the one to the left for polarization analysis. A focusing layout has been used for the initial and final polarizers. (a) - shielding, (b) - coils, (c) - sample, (d) - polarization analyzer, (e) - flipper, (f) - disc chopper, (g) - monochromator Graphite (002), (h) - neutron guide.	73
5.3	A 2D contour plot of the (ac) reciprocal plane of the $x=0.125$ single crystal at $T=250$	74
5.4	Temperature dependence of the diffuse scattering intensity for crystals with (a) $x=0.105$, (b) $x=0.115$ and (c) $x=0.125$	75
5.5	Radial scans across (002) Bragg reflection of the $x=0.125$ crystal measured with just one single detector at various temperatures.	76
5.6	Radial scan across (002) Bragg reflection of the $x=0.125$ crystal at $T=200$ K. Dotted line - fit with sum of Gauss and Voigt functions.	77
5.7	Logarithm of the diffuse scattering width plotted as a function of $\log \frac{T-175}{T}$	78
5.8	The diffuse scattering intensity as a function of temperature and a mean field theory fit (dotted line).	79
5.9	Temperature behavior of the intensity and the width of diffuse scattering	80
5.10	Polarization degree measured at pure nuclear (0,1,3) Bragg reflection as a function of temperature for the $x=0.125$ single crystal.	81
5.11	Separation of paramagnetic and nuclear coherent scattering at (0,1,3) nuclear reflection at $T=220$ K for the $x=0.125$ single crystal.	81
A.1	Reciprocal area around (1,0,0) resonant reflection for the $x=0.125$ sample at $T=50$ K	85
A.2	Reciprocal area around (1,0,0) resonant peak for the $x=0.125$ sample at $T=170$ K	86
A.3	Reciprocal area around (1,0,0) resonant peak for the $x=0.125$ sample at $T=210$ K. Splitting due to JT-distortion can easily be seen.	86
A.4	Reciprocal area around (1,0,0) resonant peak for the $x=0.125$ sample at $T=250$ K	87
A.5	Reciprocal area around (1,0,0) resonant peak for the $x=0.125$ sample at $T=295$ K	87
B.1	A 2D contour plot of the (ac) reciprocal plane of the $x=0.125$ single crystal at $T=100$ K.	89
B.2	A 2D contour plot of the (ab) reciprocal plane of the $x=0.105$ single crystal at $T=100$ K.	90

B.3	A 2D contour plot of the (ab) reciprocal plane of the $x=0.105$ single crystal at $T=250\text{K}$. . .	90
B.4	A 2D contour plot of the (c) reciprocal plane of the $x=0.115$ single crystal at $T=50\text{K}$	91
B.5	A 2D contour plot of the (c) reciprocal plane of the $x=0.115$ single crystal at $T=250\text{K}$. . .	91

Bibliography

- [1] H.A.Jahn, E. Teller, Proc. R. Soc. London **A,161** (1937) 220
- [2] C. Zener Phys. Rev. **82** (1951) 403
- [3] J.B. Goodenough: Magnetism and the Chemical Bond, Interscience Publ. (1963)
- [4] G. Jackeli, N.B. Perkins and N.M. Plakida, Phys. Rev. B **62** (2000) 372
- [5] S.-Q. Shen and Z.D. Wang, Phys. Rev. B **61** (2000) 9532
- [6] P. Novák and M. Maryško, Phys. Rev. B **60** (1999) 6655
- [7] A. Urushibara, Y. Moritoma, T. Arima, A. Asamitsu, G. Kido, Y. Tokura: Phys. Rev B **51** (1995) 14103
- [8] J. Hemberger, A. Krimmel, T. Kurz, H.-A. Krug von Nidda, V.Yu. Ivanov, A.A. Mukhin, A.M. Balbashov, A. Loidl (*unpublished*), <http://arXiv.org/abs/cond-mat/0204269>
- [9] N. Furukawa Phys. Soc. Jpn. **63** (1994) 3214
- [10] Yu. Izyumov Phys. Met. Metallogr. **89** (2000) 21
- [11] A.J. Millis, B.I. Shraiman, Phys. Rev. Lett. **74** (1995) 5144
- [12] J.B. Goodenough Phys. Rev. **100** (1955) 564
- [13] E.O. Wollan Phys. Rev. **100** (1955) 564
- [14] P.G. Radaelli, D.E. Cox, M. Marezio, S.-W.Cheong, Phys. Rev. **B55** (1997) 3015

- [15] J.M.D. Coey, M. Viret and S. von Molnar, *Adv. Phys.*, **48** (1999) 192
- [16] Y. Yamada, O. Hino, S. Nohdo, and R. Kanao, *Phys. Rev. Lett.* **77** (1996) 904
- [17] S. Mori, C.H. Chen and S.-W. Cheong, *Nature* **393** (1998) 473
- [18] Y. Tokura, Y. Tomioka, *Jour. of Magn. and Magn. Mat.* **200** (1999) 1
- [19] K.I.Kugel, D.I.Khomskii, *Sov. Phys. Uspekhi* **25** (1982) 231
- [20] I. Solovyev and T. Terakura, *Phys. Rev. Lett.* **83** (1999) 2825
- [21] J. van der Brink, G. Khaliullin, D. Khomskii, *Phys. Rev. B* **83** (1999) 5118
- [22] J. Kanamori, *J. Appl. Phys. (Suppl.)* **31** (1960) 14S
- [23] A.J.Millis, *Phys. Rev. B* **53** (1996) 8435
- [24] A.E.Nikiforov, S.E. Popov, S. Yu. Shashkin, *Phys. Met. Metallogr.* **87** (1999) 16
- [25] M.Z.Li, *J. Appl. Phys.* **83** (1998) 6596
- [26] T. Hotta, Y. Takada, H. Koizumi, E. Dagotto, *Phys. Rev. Lett.* **84** (2000) 2477
- [27] S. Yunoki, T. Hotta and E. Dagotto, *Phys. Rev. Lett* **84** (2000) 3714
- [28] G.-L. Liu, J.-S. Zhou and J.B. Goodenough, *Phys. Rev. B*, **64** (2001) 14414
- [29] H. Kawano, R. Kajimoto, Y. Yoshizawa, Y. Tomioka, H. Kuwahara, and Y. Tokura, *Phys. Rev. Lett.* **78** (1997) 4253
- [30] Y. Endoh, K. Hirota, S. Ishihara, S. Okamoto, Y. Murakami, A. Nishizawa, T. Fukunda, H. Kimura, H. Nojiri, K. Kaneko and S. Maekawa, *Phys. Rev. Lett* **82** (1999) 4328
- [31] R. Senis, V. Laukhin, B. Martinez, J. Fontcuberta, X. Obradors, A.A. Arsenov, Y.M. Mukovskii, *Phys. Rev. B* **57** (1998) 14680
- [32] T. Mizokawa and A. Fujimori, *Phys. Rev. B* **54** (1996) 5368

- [33] Y. Yamada, J. Suzuki, K. Oikawa, S. Katano, J.A. Fernandez-Baca, *Phys. Rev. B* **62** (2000) 11600
- [34] T. Niemöller, M. von Zimmermann, S. Uhlenruck, O. Friedt, B. Büchner, T. Frello, N.H. Andersen, P. Berthet, L. Pinsard, A.M. Leon-Guevara, A. Revcolevschi and J.R. Schneider, *Eur. Phys. J. B* **8** (1999) 5
- [35] Y. Murakami, J.P. Hill, D. Gibbs, M. Blume, I. Koyama, M. Tanaka, H. Kawata, T. Arima, Y. Tokura, K. Hiroto and Y. Endoh, *Phys. Rev. Lett.* **81** (1998) 582
- [36] I.S. Elfimov, V.I. Anisimov, G.A. Sawatzky, *Phys. Rev. Lett.* **82** (1999) 4264
- [37] M. Benfatto, Y. Joly, C. Natoli, *Phys. Rev. Lett.* **83** (1999) 636
- [38] J. Geck, B. Büchner, S. Kiele, P. Reutler, U. Gebhardt, P. Wochner, HASYLAB Annual Report 2001.
- [39] M. von Zimmermann, J.P. Hill, D. Gibbs, M. Blume, D. Casa, B. Keimer, Y. Murakami, Y. Tomioka and Y. Tokura, *Phys. Rev. Lett.* **83** (1999) 4872
- [40] A. Hammouche and E. Siebert, *Mater. Res. Bull.*, **24** (1989) 367
- [41] A. Montaser, D.W. Golightly, *Inductively coupled plasmas in analytical atomic spectroscopy*, VCH (1987)
- [42] S.J. Hill, *Inductively coupled plasma spectroscopy and its applications*, Sheffield Academic Press (1998)
- [43] J. Tanaka et al, *J. Crystal Growth* **60** (1982) 191
- [44] T. Hashimoto, T. Ishizawa, N. Mizutani, M. Kato, *J. Crystal Growth* **84** (1987) 207
- [45] A.M. Balbashov, S.G. Karabashev, Yu.M. Mukovskiy, S.A. Zverkov, *J. Crystal Growth* **167** (1996) 365
- [46] C.-H. Lee, *Supercond. Sci. Technol.* **11** (1998) 891
- [47] Ch. Kloc, S.-W. Cheong, P. Matl, *J. Crystal Growth* **191** (1998) 294

- [48] W. Wu, K.H. Wong, X.-G. Li and C.I.Choy, *J. Apl. Phys.* **87** (2000) 3006
- [49] X. Wen-xu, L. Bao-he, Q. Zheng-nan and J. Han-min, *J. Apl. Phys.* **86** (1999) 5164
- [50] Y.Murakami, H. Kawada, H. Kawata, T. Arima, Y. Morimoto and Y. Tokura, *Phys. Rev. Lett.* **80** (1998) 1932
- [51] E. Tsuji, T. Kurasawa, I. Yazawa, H. Katoh, N. Nomozawa, K. Isida and S. Kishimoto, *J. Phys. Soc. Jpn.* **65** (1996) 610
- [52] L. Hozoi, A.H. de Vroes, R. Broer, *Phys. Rev. B* **64** (2001) 165104
- [53] J.Stremper, Th. Brückel, U. Rütt, J.R. Schneider, K.-D. Liss, Th. Tschentscher, *Acta Cryst. A* **52** (1996) 438
- [54] D. Hupfeld, Dissertation, Hamburg University (1998)
- [55] S. Brennan, P.L. Cowan, *Rev. Sci. Instr.* **63** (1992) 850
- [56] J.H. Van Vleck, *Phys. Rev.* **55** (1939) 924
- [57] P. de Gennes, K. *Phys. Chem. Sol.* **3** (1958) 223
- [58] Th. Brückel, W. Schweika, Polarized Neutron Scattering, Lectures, Forschungszentrum Jülich GmbH (2002)
- [59] D. Hohlwein, Th. Zeiske, *Phys. B.* **276-278** (2000) 584
- [60] J.-U. Hoffmann, D. Hohlwein, R. Schneider, A.H. Moudden, *Phys. B.* **276-278** (2000) 608

B.1 List of Abbreviations

AFM - Antiferromagnetic

APS - Advanced Photon Source

CA - Canted

CF - Crystal Field

CMR - Colossal Magnetoresistance

CO - Charge Ordering

DE - Double Exchange

DESY - Deutsches Synchrotron

DNS - Diffuse Neutron Scattering (also instrument at FRJ-2)

EIS - Electron Ion Spectroscopy

FM - Ferromagnetic

FRJ-2 - Forschungsreaktor Jülich

FZM - Floating-Zone Method

ICAP - Inductively Coupled Argon Plasma

IFF - Institut für Festkörperforschung

JT - Jahn-Teller

NSF - Non-Spin-Flip

OO - Orbital Ordering

PM - Paramagnetic

r.l.u. - Reciprocal Lattice Units

RXS - Resonant X-Ray Scattering

SE - Super Exchange

SF - Spin-Flip

T_c - Curie temperature

TOF - Time-of-flight

x - doping level, $0 \leq x \leq 1$

XPD - X-Ray Powder Diffraction

B.2 Acknowledgement

I would like to thank following people, without their help and support this work would not be possible.

- Prod. Thomas Brückel - My scientific supervisor.
- Dr. Yixi Su - Co-experimentator in all experiments since 2001.
- Dr. Werner Schweika - For the experiments at the DNS beamline in Jülich.
- Dr. Dirk Hupfeld - For participation in the experiments at the Mu-Cat, APS and for the computer program for absorption correction.
- Jörg Voigt and Dr. Didier Wermeille - For participation in the experiments at the Mu-Cat, APS.
- Dr. Oliver Seeck - For local support in experiments at the W1, HASYLAB.
- Abdel Mohamed Fattah, Dr. Volker Kaiser (RWTH, Aachen) - For crystal growing at the Institute for Crystallography, RWTH.
- Dr. Paul Meuffels, H.J. Bierfeld, Pascal Foucart - For help with sample preparation.
- Simon Stein - For magnetization measurements with SQUID.
- Mrs. Hannelore Lippert - For Chemical Analysis of powders with ICAP.
- Mrs. Rose Fischer - For Laue analysis and single crystal orientation.
- Waldemar Babik - For a convenient computer program for data analysis.
- Dr. Ulrich Köbler - For fruitful discussions of the magnetization measurements.

Thank you very much for your contribution!

B.3 Curriculum Vitae

Personal Data	
Name	Konstantin Istomin
Date of Birth	11.01.1975
Place of Birth	Novosibirsk, USSR
Citizenship	Russian
Address	Meyburginsel 31/38, D52428 Jülich, Germany
Telephone Number	+49 174 8324588
Education	
1982-1992	School No.190, Novosibirsk
1992-1998	Novosibirsk State Technical University (Physical Engineering Department)
1999-2002	RWTH Aachen (Department of Mathematics, Informatics and Nature Sciences)
Work	
September 1995 - June 1999	Budker Institute of Nuclear Physics, Novosibirsk, Russia (Research Fellow)
July 1999 - March 2003	Research Centre Jülich, Germany (Ph.D. Student, Guest Scientist)
Grades	Thesis Titles
June 1996 (Bachelor of Physics)	Ionization chamber as an absolute detector of ultrasoft synchrotron radiation.
June 1998 (Master of Physics)	Calibration of detectors for nuclear physics using synchrotron radiation.
March 2003 (Doctor of Science)	Interplay between charge, spin and orbital ordering in $\text{La}_{1-x}\text{Sr}_x\text{MnO}_3$ manganites.